

# BULGARIAN CHEMICAL COMMUNICATIONS

2024 Volume 56 / Number 4

*Journal of the Chemical Institutes  
of the Bulgarian Academy of Sciences  
and of the Union of Chemists in Bulgaria*



## Thin film humidity sensing elements based on TiO<sub>2</sub> and graphene

Z. P. Nenova<sup>1\*</sup>, S. V. Kozhukharov<sup>2</sup>, T. G. Nenov<sup>1</sup>, N. D. Nedev<sup>1</sup>

<sup>1</sup> Technical University of Gabrovo, 4, Hadzhi Dimitar Str., 5300, Gabrovo, Bulgaria

<sup>2</sup> University of Chemical Technology and Metallurgy, 8, St. Kliment Ohridski Blvd., 1756, Sofia, Bulgaria

Received: September 02, 2023; Revised: July 05, 2024

Thin film humidity sensing elements based on TiO<sub>2</sub> and graphene prepared *via* a sol-gel method were developed. Titanium (IV) n-butoxide (TBOT) and graphene nanoplatelet aggregates (GNPs) were used as basic materials. The samples were sintered at 400°C, 600°C and 800°C. The map data analyses of the surface layer materials were carried out by energy dispersive X-ray (EDX) spectroscopy and the structural characterization – by X-ray diffractometry (XRD). The electrical properties of the sintered sensing elements were investigated in the range of 17% to 85% relative humidity at 20 Hz and 25°C. The experimental results were analyzed for groups of samples with different initial graphene content depending on the sintering temperature (400°C, 600°C and 800°C). The obtained characteristics show that at all investigated sintering temperatures the proposed samples based on TiO<sub>2</sub> and graphene surface layers have a wider range of variation of their resistance *R* to humidity, as well as a lower resistance compared to the corresponding reference samples without graphene. The maximum relative sensitivity  $S_{Rrel\ max}$  is highest for the samples sintered at 400°C and 600°C with a higher amount of graphene in the preparation and reaches up to about 735 and 501, respectively, and the resistance variation range - up to about 3 orders of magnitude.

**Keywords:** humidity sensing elements, sol-gel method, titanium dioxide, graphene

### INTRODUCTION

Humidity measurement and control are widely used in industry and agriculture, storage of various products, meteorology, medicine and health care, environmental protection, etc. [1, 2]. Sensors are an important part of humidity measuring devices, with a constant aim at improving their parameters and characteristics.

Resistive sensors are widely used among humidity sensors, most often based on oxide materials such as Al<sub>2</sub>O<sub>3</sub> [3, 4], TiO<sub>2</sub> [5-8], SnO<sub>2</sub> [9-12], ZnO [13-15], SiO<sub>2</sub> [16-18], etc. TiO<sub>2</sub> is one of the oxides used for development of the sensitive elements of humidity sensors due to its good hydrophilicity. To improve the characteristics of the sensor elements, various alloying additives are used [19].

Since its discovery in 2004 [20], graphene has been explored for various applications due to its unique electrical, thermal, and mechanical properties. Research has also been conducted on its application in sensors [21, 22]. The study in [23] examines the humidity sensitivity of graphene/TiO<sub>2</sub> composites prepared by sol-gel technology and sintered at 400°C. A humidity sensor based on graphene oxide films supported by TiO<sub>2</sub> nanorods has been investigated in [24].

In the present work, thin film humidity sensing elements based on TiO<sub>2</sub> and graphene prepared by a sol-gel method are proposed. Their preparation follows an uncomplicated procedure and affordable materials, namely titanium (IV) n-butoxide (TBOT) as a precursor of TiO<sub>2</sub> and graphene aggregates of nanoplatelets (GNPs) as an additive. The influence of the amount of graphene additive and of the sintering temperature (400°C, 600°C and 800°C) on the electrical resistance and humidity sensitivity of the sensor elements is investigated in order to obtain groups of sensitive elements with improved humidity sensing properties.

### EXPERIMENTAL

#### *Sample preparation*

The preparation of the studied sensing elements is divided into three subsequent stages: (i) sol systems preparation; (ii) film deposition and gelation and (iii) final sample sintering.

#### *(i) Sol systems preparation*

The following materials were used for the sol-gel systems preparation: titanium (IV) n-butoxide (TBOT), produced by Alfa Aesar, graphene nanoplatelet aggregates (GNPs) produced by Alfa Aesar, 1-butanol 99% and nitric acid 65%.

\* To whom all correspondence should be sent:  
E-mail: [z\\_nenova@yahoo.com](mailto:z_nenova@yahoo.com)

Initially, mixtures of 30 ml of butanol, 30 ml of TBOT and 3 ml of nitric acid were prepared in two separate beakers by intensive shaking. To one of the mixtures 6.0599 g of graphene (GNPs) was added. In this way, two solutions were prepared, without and with graphene addition, which are denoted as reference solution and base solution with graphene, respectively. Both vessels were placed in an ultrasonic bath for 1 hour.

After that, different amounts of the obtained solutions were poured into 3 test tubes and the following compositions were obtained: TiR - 20 ml reference solution; TiG1 - 10 ml reference solution and 10 ml base solution with graphene; TiG2 - 20 ml base solution with graphene. The resulting compositions were left for 2 hours at 75°C.

#### (ii) Film deposition and gelation

Prior to the deposition process, the respective solutions were heated for 30 min at 75°C. The deposition was carried out on alumina substrates with symmetrical interdigital silver-palladium electrodes with an electrode width and distance between them of 0.5 mm [8], pre-cleaned by immersion in ether overnight. The layers were deposited by sixfold dipping in test tubes. This procedure was performed by subsequent exposure of the specimens to the solutions for 15 min, and 15 min drying at 75°C. The last drying was performed for 30 min. Finally, the samples were left to ambient conditions at least overnight, in order to achieve the final gelation of the films.

#### (iii) Final sample sintering

After gel deposition, the samples were sintered at 400°C, 600°C and 800°C for 30 min.

Additionally, after deposition on the ceramic substrates, the gels were placed in Petri dishes and, to convert them into powders, they were sintered for subsequent XRD analysis at the same temperatures as the samples.

In the designations of samples and powder materials, the sintering temperature is added as “\_xxx” to the entered abbreviation of the corresponding group of samples with a given composition: TiR\_xxx, TiG1\_xxx and TiG2\_xxx.

#### Surface morphology and structural characterization

Morphological observations of the surface layers of the developed samples were taken by scanning electron microscopy (SEM) combined with elemental analysis, by TESCAN, SEM/FIB LYRA I

XMU working at 20 kV at magnification  $\times 5000$ . The map data analyses were carried out by energy dispersive spectroscopy (EDX) using an energy dispersive spectrometer (Quantax 200 of Bruker detector).

Structural and compositional characterization was performed by X-ray diffraction analysis (XRD) on powder materials from the respective gels for the separate groups of samples, TiR, TiG1 and TiG2, sintered at 400°C, 600°C and 800°C. The studies were carried out on a Philips PW 1050 instrument equipped with a CuK $\alpha$ -X-ray emitter and a monochromator of diffracted radiation within the angle range ( $2\theta$ ) from 7° to 95° with a step of 0.05° $2\theta$ .

#### Electrical measurements

The measurements of the electrical resistance  $R$  of the developed samples were taken on a precision impedance analyzer 6505P of Wayne Kerr Electronics Ltd., at a frequency of the excitation signal of 20 Hz and 500 mV at 25°C. The samples were put inside a humidity/temperature conditioning chamber VAPORTRON H-100BL manufactured by Buck Research Instruments L.L.C., which provides conditioning of accurately controlled humidity in the range of 15–93% with maximal deviation of up to  $\pm 1.5\%$  of relative humidity at a given temperature.

## RESULTS AND DISCUSSION

#### SEM and EDX analyses

The obtained SEM and EDX images during the observations of the surface layers of the investigated samples TiR, TiG1 and TiG2 sintered at temperatures 400°C, 600°C and 800°C are presented in Fig. 1.

The SEM-images show that surface layers consisting of the individual aggregates of the sintered material separated by channel-like spaces are observed in all samples. These channel-shaped spaces grow at a sintering temperature of 800°C for the samples with the presence of graphene in the starting material. They contribute to the occurrence of capillary condensation, and as the size increases, the relative humidity levels at which these processes begin, increase.

The EDX images confirm the presence of Ti and O in the surface layers of all sample types, with C also present for samples TiG1 and TiG2.

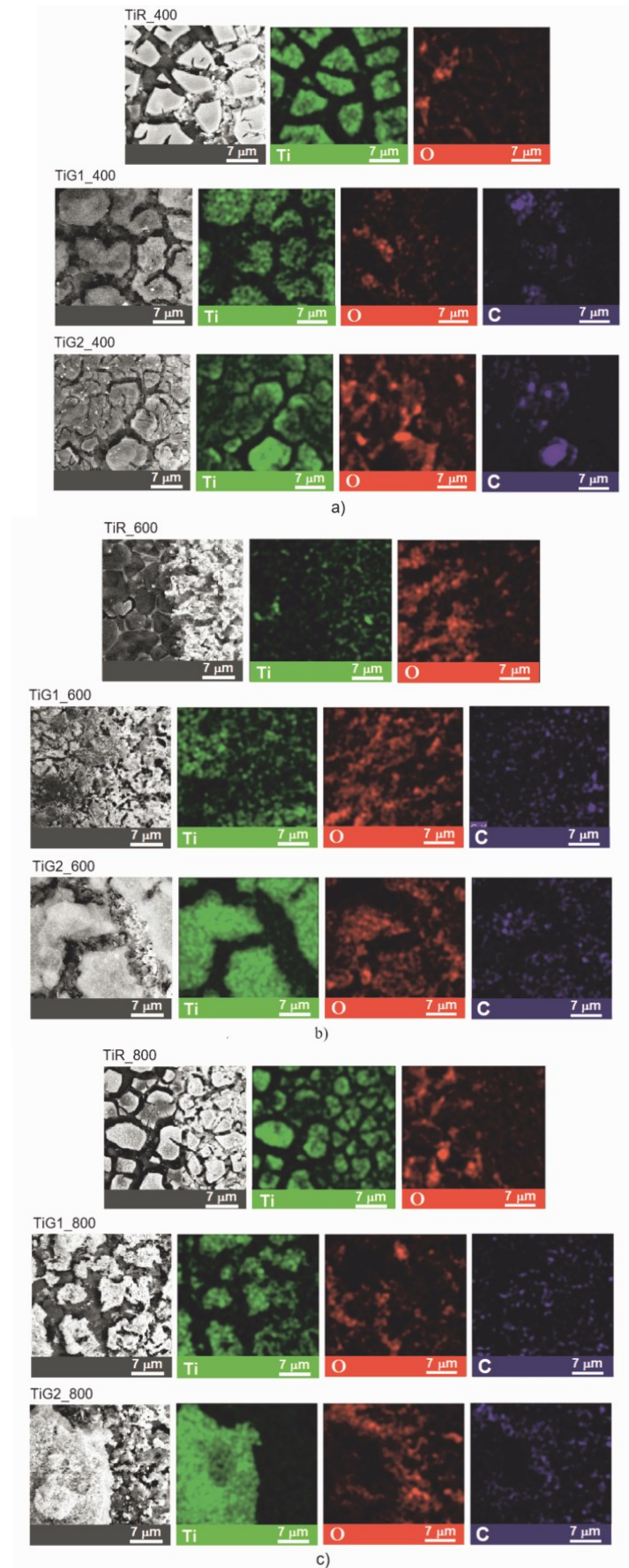


**Fig. 1.** SEM and EDX images of the surface layers of samples TiR, TiG1 and TiG2 sintered at temperatures of: a) 400°C, b) 600°C and c) 800°C

## XRD analysis

The XRD patterns of the materials of the investigated samples TiR, TiG1 and TiG2 for each of the sintering temperatures are presented in Fig. 2.

At a sintering temperature of 400°C for all TiR, TiG1 and TiG2 samples, regardless of the absence or presence of graphene in the preparation, the material structure of the surface layers corresponds to TiO<sub>2</sub> – anatase (PDF code: 01-071-1169). At 600°C, a transformation to rutile begins for all samples and the structure includes TiO<sub>2</sub> - anatase and rutile (PDF code: 01-078-1510). At 800°C, for TiR samples without the presence of graphene in the preparation, the structure of the samples contains rutile, and for TiG1 and TiG2 it includes TiO<sub>2</sub> – rutile and smaller amounts of anatase. For samples TiG1 and TiG2, sintered at 400°C, 600°C and 800°C, XRD studies also show the presence of graphite (PDF code: 00-026-1079). As noted in [25], at temperatures between 550°C and about 1000°C, anatase is irreversibly converted into the equilibrium rutile phase and the temperature of this transformation depends on the impurities or dopants present. In the case under consideration, in the material of the reference samples, the transformation to rutile was completed at 800°C, while in the presence of graphene additive in the preparation of the samples, the materials sintered at 800°C, along with rutile, still contained anatase.

Since there is a difference in the profiles of the diffraction lines, the crystallite sizes of anatase and rutile were calculated according to the Scherrer equation [26] from the measured half-width of the lines. For samples TiR, TiG1, TiG2 sintered at 400°C, the sizes of anatase crystallites are 6 nm, 6 nm, 5 nm, respectively; at 600°C - of anatase crystallites: 22 nm, 21 nm, 21 nm; at 800°C – for the samples with graphene, of anatase crystallites: 27 nm, 27 nm, of rutile crystallites for the three types of samples: 35 nm, 33 nm, 32 nm. There is no significant difference between the crystallite sizes of anatase and rutile for the respective groups at the same sintering temperatures.

Crystallite sizes increase with increasing sintering temperature. This increase may also result in an increase in the intercrystallite spaces, which would affect the sensitivity at different relative humidity levels.

## Electrical characteristics

The characteristic  $R = f(RH)$  of the resistance  $R$  versus the relative humidity RH for the individual groups of samples TiR, TiG1 and TiG2 at sintering

temperatures of 400°C, 600°C and 800°C, investigated at 20 Hz and 25°C in the range of (17-85)% RH, are presented in Fig. 3. They allow to follow the influence of the initial amounts of graphene in the preparation of the samples on the corresponding characteristics.

The maximum relative variation ( $R_{max}/R_{min}$ ) of the parameter  $R$  of the humidity sensing elements in the range from  $RH_{min}$  to  $RH_{max}$  can be assumed to be the maximum relative sensitivity:

$$S_{Rrel\ max} = R_{max}/R_{min} \quad (1)$$

over the entire RH range with respect to resistance.

The range of resistance variation in orders of magnitude can be calculated as:

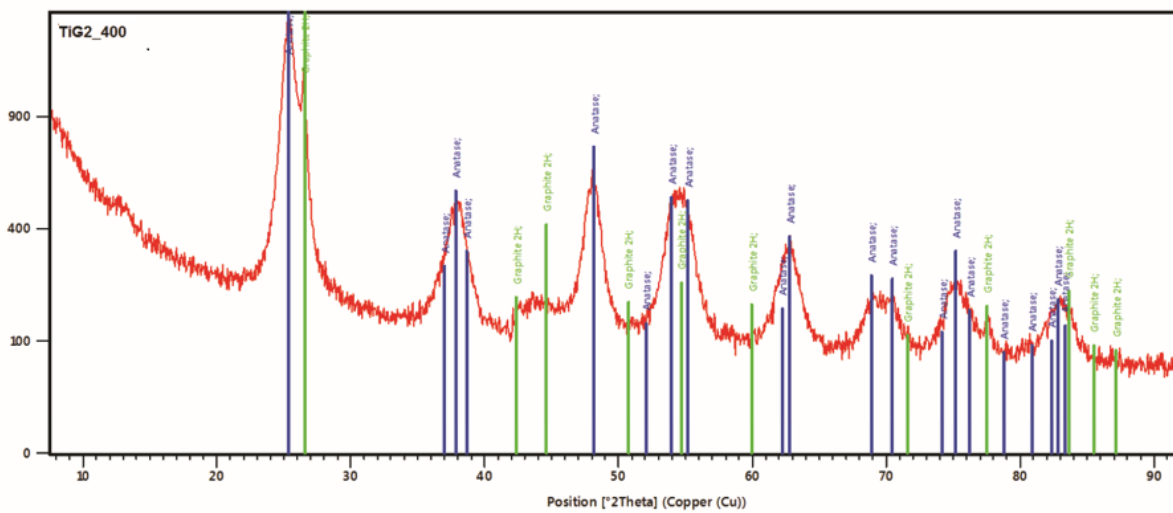
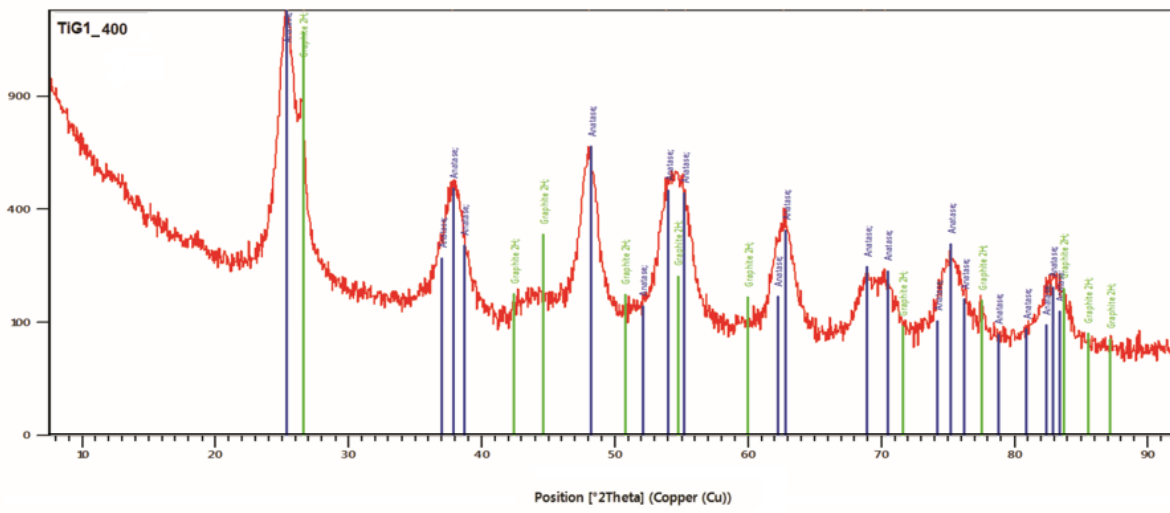
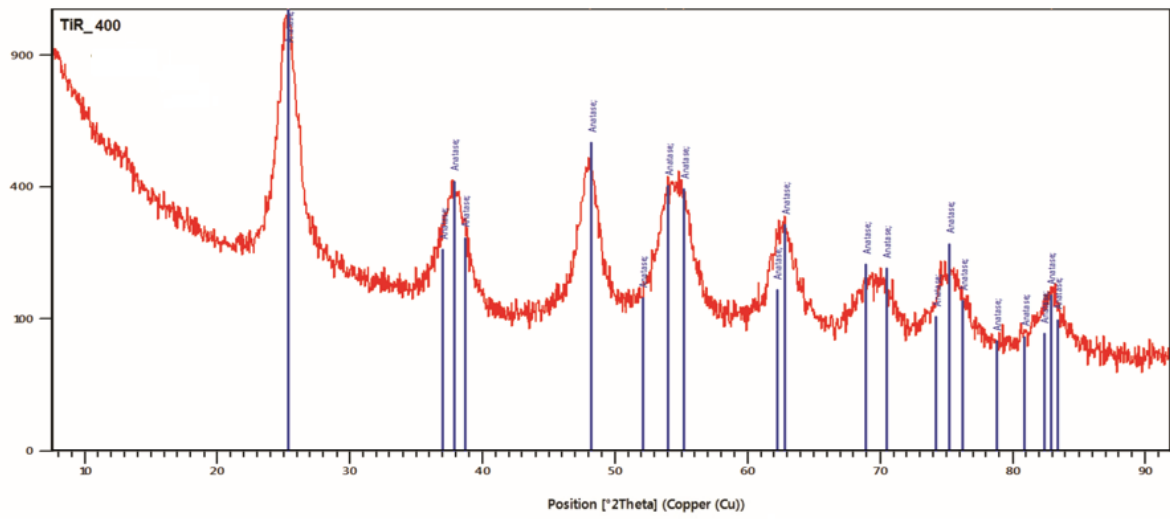
$$L_R = \lg(R_{max}/R_{min}) = \lg(R_{max}) - \lg(R_{min}) \quad (2)$$

For the studied samples, in the range of (17-85)% RH the maximum relative sensitivity  $S_{Rrel\ max}$  and the resistance variation range  $L_R$  in orders of magnitude are presented in Table 1.

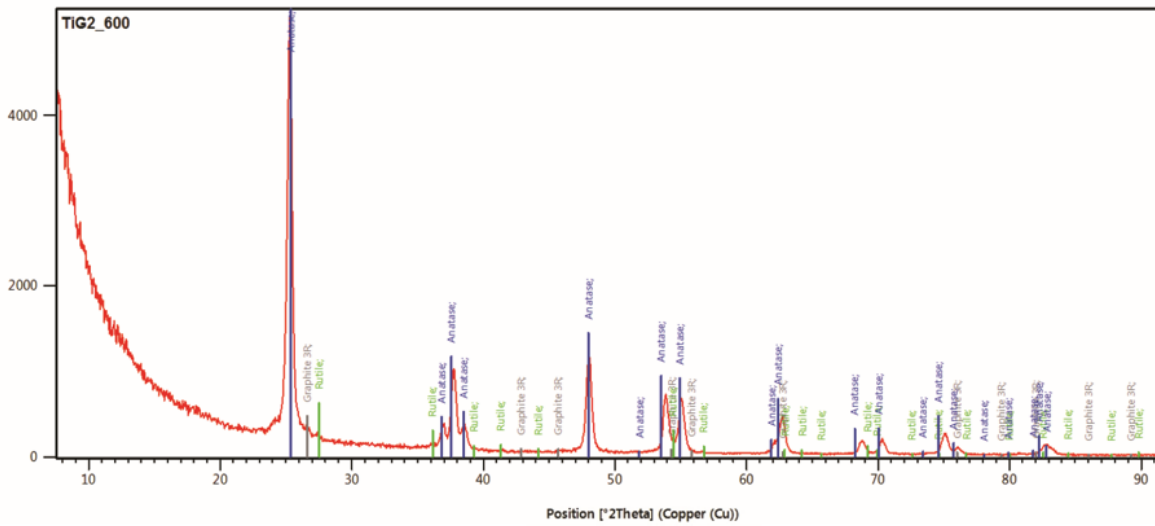
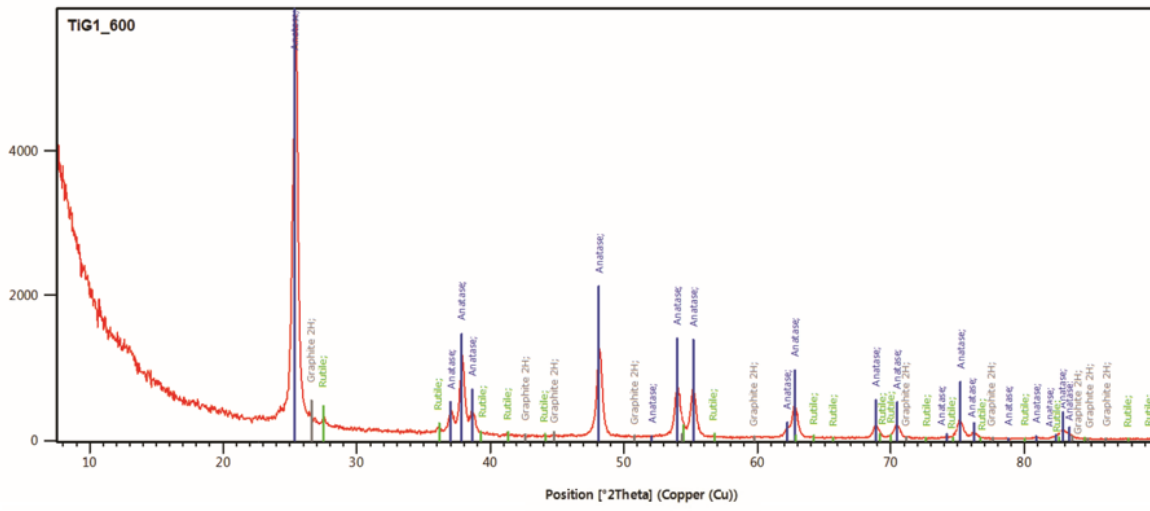
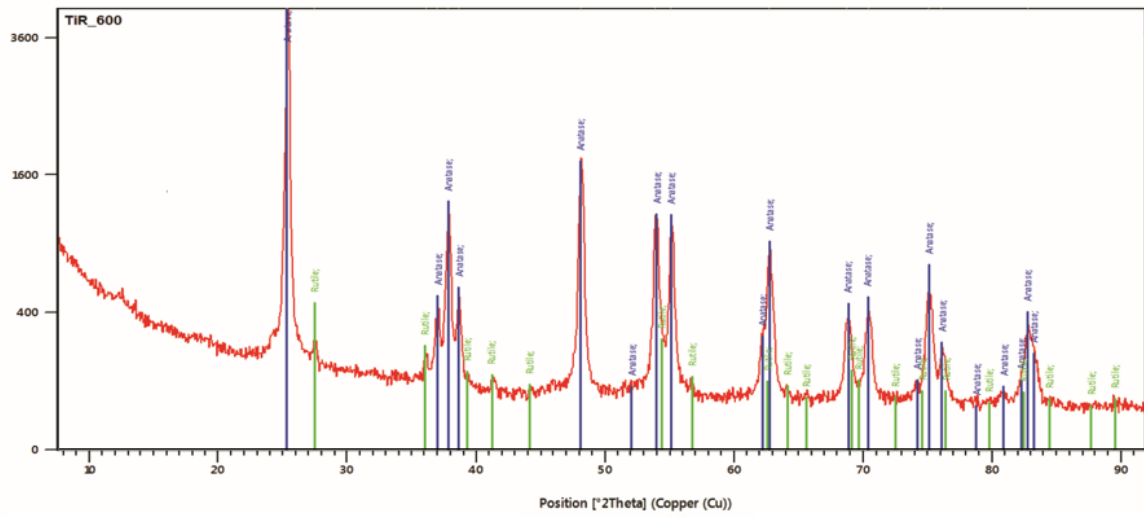
**Table 1.** Maximum relative sensitivity  $S_{Rrel\ max}$  and resistance variation range  $L_R$

Sample	$S_{Rrel\ max}$	Resistance variation range $L_R$ , orders of magnitude
TiR_400	22.4	1.35
TiG1_400	406.20	2.61
TiG2_400	735.84	2.87
TiR_600	5.65	0.75
TiG1_600	155.65	2.19
TiG2_600	501.73	2.70
TiR_800	2.56	0.41
TiG1_800	73.43	1.86
TiG2_800	105.27	2.02

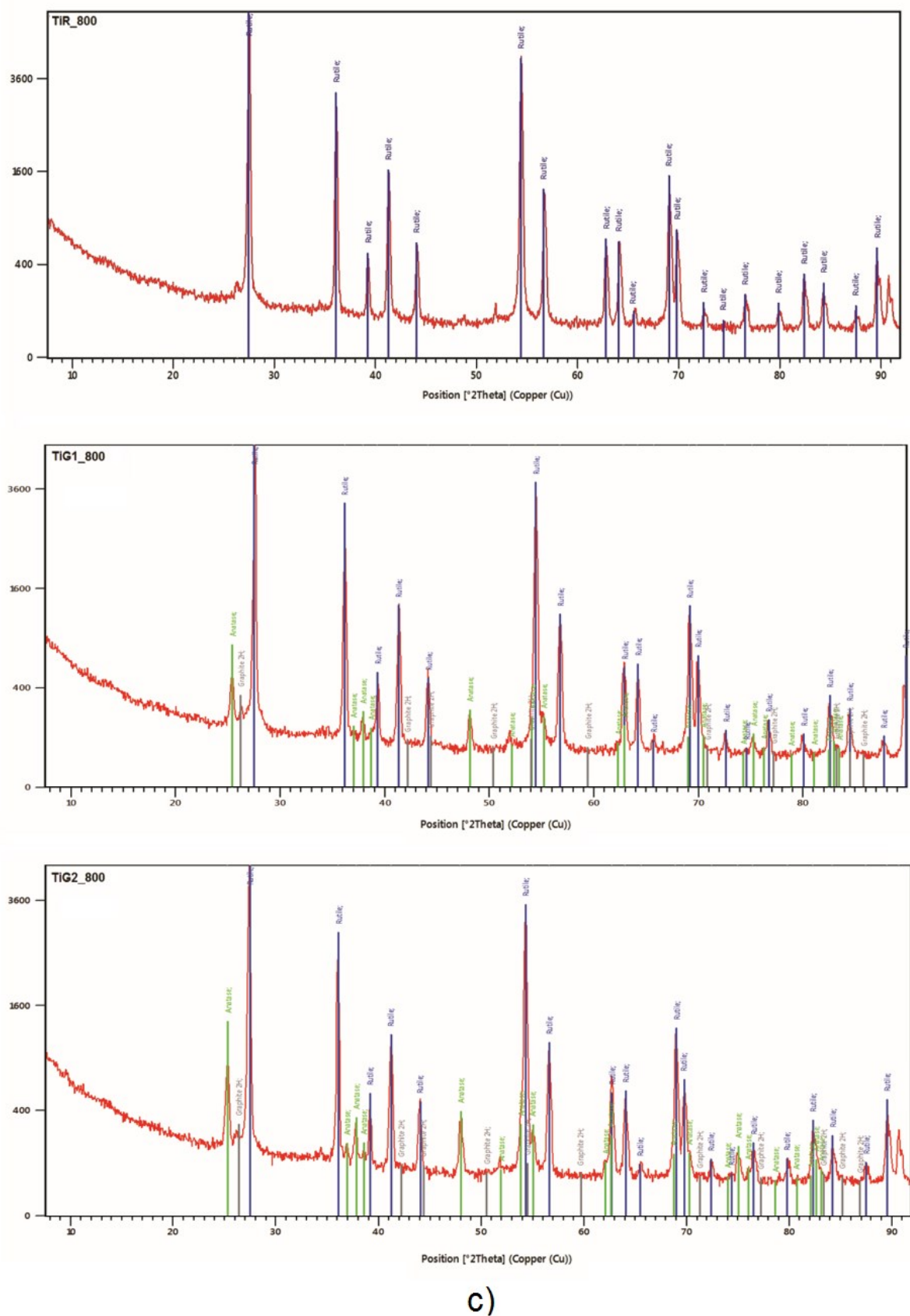
For samples TiG1 and TiG2 prepared with the addition of graphene, at all sintering temperatures their maximum relative sensitivity  $S_{Rrel\ max}$  increased compared to that of the reference samples TiR, this increase being about 33 times at 400° C, 88 times at 600° C and 41 times at 800° C. For the reference samples, the relative change in  $R$  was about 1.4 orders of magnitude at 400°C, about 0.8 orders of magnitude at 600°C, and about 0.4 orders of magnitude at 800°C. This variation for TiG1 samples was about 2.6 orders of magnitude at 400°C, about 2 orders of magnitude at 600°C and 800°C, while for TiG2 samples it reached about 3 orders of magnitude at 400°C and 600°C and about 2 orders of magnitude at 800°C sintering temperatures.



a)



b)



c)

**Fig. 2.** XRD images of the materials of samples TiR, TiG1 and TiG2 sintered at temperatures of: a) 400°C, b) 600°C and c) 800°C

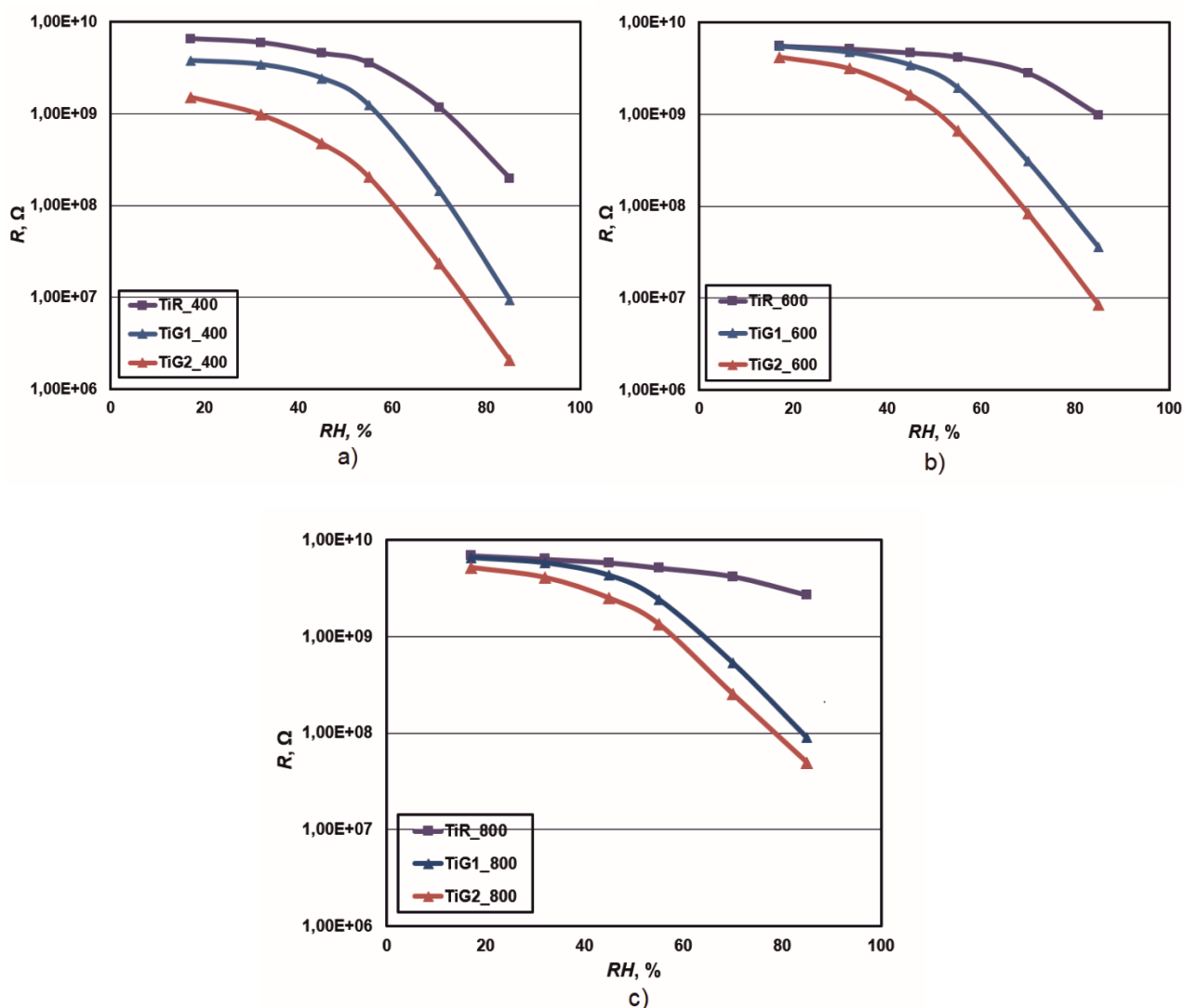


**Fig. 3.** Characteristic  $R = f(RH)$  for samples TiR, TiG1 and TiG2 at sintering temperatures of: a) 400°C; b) 600°C and c) 800°C, investigated at 20 Hz and 25°C.

Moreover, the increase in the graphene content during the preparation of the sensitive layers leads to a certain decrease in their resistance due to the appearance of graphite in the aggregates in the surface layers after sintering the samples. This is favorable for the connection of the sensing elements in measurement circuits.

For all investigated sintering temperatures of 400°C, 600°C and 800°C, the samples in the presence of graphene additive have improved properties compared to the reference samples. At a given sintering temperature, a greater variation of the resistance and a higher sensitivity of the samples started to appear at lower relative humidity levels with increasing initial amounts of graphene, where the steepness of the characteristics (Fig. 3) on a semi-logarithmic scale becomes more significant.

At higher sintering temperatures and a set initial amount of graphene in the preparation of the

samples, a relatively higher resistance was observed, associated with an increase in the spaces between the aggregates in the surface layers, best expressed at 800°C.

Regarding the  $S_{Rrel\ max}$  of the samples, at 800°C sintering temperature, a certain decrease in this variation was observed for each of the sample groups with the same initial amount of graphene due to an increase in the intercrystalline spaces and in the spaces between the surface aggregates, therefore the processes of capillary condensation of water vapor in accordance with Kelvin's equation [27] and sensitivity begin to manifest themselves at higher relative humidity levels. Furthermore, increasing the sintering temperature leads to a transformation of the TiO<sub>2</sub> structure from anatase to rutile, as noted in the XRD-analysis results. The use of initial amounts of graphene additives leads to the fact that at 800°C there is still the presence of anatase in the structure

of the obtained layers, as noted above [25]. In accordance with [28], the anatase structure of TiO<sub>2</sub> favors its hygroscopic properties.

Due to these factors, a larger relative change of the resistance  $R$  with the change of relative humidity RH is observed at sintering temperatures of 400°C and 600°C, and this is best expressed in TiG2 samples with larger initial amounts of graphene (TiG2\_400 and TiG2\_600), the resistance variation range reaching about 3 orders of magnitude when relative humidity changes from 17% RH to 85% RH.

### CONCLUSIONS

It was established that for the developed samples based on TiO<sub>2</sub> and graphene, prepared by a sol-gel method, the increase in the initial amounts of graphene leads to an increase in the maximum relative resistance variation, respectively – maximum relative sensitivity  $S_{Rrel\ max}$  of the samples and to a decrease of their resistance. For all investigated sintering temperatures, for the groups of sensor elements with the presence of graphene in the starting solution, an increase in the maximum relative resistance variation with respect to humidity was observed compared to the reference samples without the presence of graphene additive.

The highest maximum relative sensitivity  $S_{Rrel\ max}$  to humidity is observed in the samples with larger initial amounts of graphene at 400°C and 600°C sintering temperatures (TiG2\_400 and TiG2\_600) – about 735 and 501, respectively, and the relative resistance variation range  $L_R$  reaches about 3 orders of magnitude (2.9 and 2.7 orders of magnitude, respectively). With smaller amounts of graphene, a relative resistance change of about 2.6 orders of magnitude is observed at a lower sintering temperature – 400°C (TiG1\_400) and about 2.2 orders of magnitude – at 600°C (TiG1\_600). For the remaining samples from the two groups at sintering temperature 800°C (TiG1\_800 and TiG2\_800), the relative resistance change is in the range of about 2 orders of magnitude (1.9 and 2.0 orders of magnitude, respectively).

The developed sensor elements have good humidity properties, are made of inexpensive materials by a simple technology, which makes them suitable for practical applications.

**Acknowledgement:** The present study was made possible thanks to the support by the European Regional Development Fund under the OP "Science and Education for Smart Growth 2014 - 2020," Project CoC "Smart Mechatronic, Eco- and Energy Saving Systems and Technologies" Grant number BG05M2OP001-1.002-0023.

### REFERENCES

1. R. Wernecke, J. Wernecke, Industrial Moisture and Humidity Measurement: A Practical Guide, Wiley-VCH Verlag GmbH & Co, Weinheim, 2014.
2. P. Wiederhold, Water Vapour Measurement: Methods and Instrumentation, Marcel Dekker, New York, 1997.
3. G. Sberveglieri, R. Anchisini, R. Murri, C. Ercoli, N. Pinto, *Sens. Actuators B Chem.*, **32**, 1 (1996).
4. B. Cheng, B. Tian, C. Xie, Y. Xiao, S. Lei, *J. Mater. Chem.*, **21**, 1907 (2011).
5. T. Nenov, Z. Nenova, *Ceram. Int.*, **39**, 4465 (2013).
6. Y. Hase, V. Sharma, V. Doiphode et al., *J. Mater. Sci.: Mater. Electron.*, **33**, 11825 (2022).
7. M. M. Zahidi, M. H. Mamat, M. F. Malek, M. K. Yaakob, M. K. Ahmad, S. A. Bakar, A. Mohamed, A. S. R. A Subki, M. R. Mahmood, *Sens.*, **22**, 5794 (2022).
8. S. Kozhukharov, Z. Nenova, T. Nenov, N. Nedev, M. Machkova, *Sens. Actuators B Chem.*, **210**, 676 (2015).
9. S. Pan, G. Gayathri, T.S. Reshma, G. Mangamma, A. K. Prasad, A. Das, *Sens. Actuators A Phys.*, **346**, 113835 (2022).
10. D. Toloman, A. Popa, M. Stan, C. Socaci, A. R. Biris, G. Katona, F. Tudorache, I. Petrila, F. Iacomini, *Appl. Surf. Sci.*, **402**, 410 (2017).
11. M. Parthibavarman, V. Hariharan, C. Sekar, *Mater. Sci. Eng. C*, **31**, 840 (2011).
12. Q. Kuang, C. Lao, Z. L. Wang, Z. Xie, L. Zheng, *J. Am. Chem. Soc.*, **129**, 6070 (2007).
13. S. Yu, H. Zhang, C. Chen, C. Lin, *Sens. Actuators B Chem.*, **287**, 526 (2019).
14. S. P. Gupta, A. S. Pawbake, B. R. Sathe, D. J. Late, P. S. Walke, *Sens. Actuators B Chem.*, **293**, 83 (2019).
15. E. Modaresinezhad, S. Darbari, *Sens. Actuators B Chem.*, **237**, 358 (2019).
16. H. Zhao, T. Zhang, R. Qi, J. Dai, S. Liu, T. Fei, G. Lu, *Sens. Actuators B Chem.*, **266**, 131 (2018).
17. Z. Nenova, T. Nenov, S. Kozhukharov, N. Nedev, *IEEE Sensors J.*, **18** (17), 6946 (2018).
18. Z. P. Nenova, S. V. Kozhukharov, T. G. Nenov, N. D. Nedev, M. S. Machkova, *Bulg. Chem. Commun.*, **45**, Special Edition A, 11 (2013).
19. A. Farzaneh, A. Mohammadzadeh, M. D. Esrafil, O. Mermer, *Ceram. Int.*, **45**, 8362 (2019).
20. K. S. Novoselov, A. K. Geim, S. V. Morozov, D. Jiang, Y. Zhang, S. V. Dubonos, I. V. Grigorieva, A. A. Firsov, *Science*, **306**, 666 (2004).
21. D. Shahdeo, A. Roberts, N., S. Gandhi, *Compr. Anal. Chem.*, **91**, 175 (2020).
22. A. Naga, A. Mitra, S. C. Mukhopadhyay, *Sens. Actuators B Chem.*, **270**, 177 (2018).
23. W.-D. Lin, C.-T. Liao, T.-C. Chang, S.-H. Chen, R.-J. Wu, *Sens. Actuators B Chem.*, **209**, 555 (2015).
24. X. Zhao, X. Chen, X. Yu, X. Ding, X. Yu, X. Chen, *Diam. Relat. Mater.*, **109**, 108031 (2020).
25. A. H. Dorian, C. C. Sorrell, *J. Mater. Sci.*, **46**, 855 (2011).

26. P. Scherrer, *Göttinger Nachrichten Gesell.*, **2**, 98 (1918).
27. Y. Shimizu, H. Arai, T. Seiyama, *Sens. Actuators*, **7**, 11 (1985).
28. B. Fubini, V. Bolis, M. Bailes, F. S. Stone, *Solid State Ion.*, **32–33**, 258, Part 1 (1989).

# Sulfide driven fuel cell performance enhanced by integrated chemisorption and electricity generation

S. Stefanov<sup>1</sup>, D. Uzun<sup>2</sup>, L. Ljutzkanov<sup>1</sup>, V. Beschkov<sup>1\*</sup>

<sup>1</sup>*Institute of Chemical Engineering, Bulgarian Academy of Sciences, 1113 Sofia, Bulgaria*

<sup>2</sup>*Institute of Electrochemistry and Energy Systems, Bulgarian Academy of Sciences, 1113 Sofia, Bulgaria*

Received: May 23, 2024; Revised: July 14, 2024

This study is related to the direct utilization of the hydrogen sulfide in the Black Sea water as energy source in a sulfide-driven fuel cell. One of the main obstacles for the practical application of this process is the low concentration of hydrogen sulfide, less than 20 g dm<sup>-3</sup>.

We propose a scheme of preliminary saturation with sulfide from the sea water of an electro-conductive sorbent doped by metal oxides, forming sulfides with low solubility. The latter simultaneously serve as sorbent and electrode (anode). The next step is sulfide oxidation at a regime of fuel cell with generation of electromotive force. The resulting oxidation products are removed by elution with a solution of supporting electrolyte. We achieved two goals: first, concentration of sulfide on the sorbent to practically significant amounts and second, electricity production in a fuel cell mode together will sorbent regeneration.

Our experiments were carried out in a membraneless fuel cell with gas-diffusion electrode as cathode containing a catalyst doped with compounds of cobalt and manganese. The anode was doped by zinc oxide embedded into electro-conductive char produced by pyrolysis of waste soot. The sorption capacity of the sorbent was practically independent on the sulfide concentration in the feeding solution.

The experimental results show the stable work of both electrodes with high sorption capacity for sulfide on the anode (0.15%wt.), high current density (up to 20 A/m<sup>2</sup>) and power density (up to 2.5 W/m<sup>2</sup>). Different products of sulfide oxidation were detected, namely, polysulfide, sulfite and sulfate. Polysulfides were detected when the sulfide concentrations in the eluting solution were rather high. The oxidation products at low sulfide concentrations are mainly sulfite and sulfate.

**Keywords:** sulfide fuel cell, chemo-sorption, catalysis, gas diffusion electrode

## INTRODUCTION

The present paper deals with the use of sulfide as a fuel for sulfide-driven fuel cell. Cases were considered when the sulfide concentration is low and its direct feed in the fuel cell is not practically reliable.

It is the case of the Black Sea where the amount of hydrogen sulfide is enormous, but its concentration is rather low, i.e. it reaches up to 20 g m<sup>-3</sup> at the biggest depth (*ca.* 2200 m) [1, 2]. This fact makes the use of hydrogen sulfide not suitable as a fuel for practical purposes. There is an effort for stripping of hydrogen sulfide from marine water by heating and further processing in gaseous phase [3, 4]. This process is accompanied by considerable input of thermal energy.

There are some other efforts, each of them associated to the separation of hydrogen sulfide by membrane processes [5], membrane separation with consequent pressure swing adsorption in gaseous phase (6). Dutta *et al.* have proposed a sulfide driven fuel cell operating in gaseous phase [7]. The drawback in this case is the released sulfur being

harmful for the anodes. Kim & Han [8] have studied a liquid phase sulfide fuel cell attaining high current densities but in very strong alkaline medium, i.e. 3N NaOH, which is harmful for the marine aquatic life.

In the last decade some of the authors of the present paper proposed the use of sulfide-driven fuel cell in aqueous solutions to produce electricity and clean the sea water to some extent [9, 10]

In our case the goal is to increase the sulfide concentration in the aqueous phase to reach practically important current and power densities during sulfide-driven fuel cell operation. One possible way to overcome the drawback of low sulfide concentrations in the feed is to adsorb sulfide anions on ion-exchange resin and then to elute sulfide by a certain eluent (e.g. sodium hydroxide solution) with desired amount and flow rate to increase sulfide concentration to an appropriate level. There are attempts for sulfide retention on anion-exchange resins [11, 12], but the problem is the difficult back-elution of sulfide. Another problem is the use of more alkaline eluent (like sodium hydroxide) which is not appropriate from environmental point of view.

\* To whom all correspondence should be sent:  
E-mail: vbeschkov@yahoo.com

Our idea is to compose a electro-conductive chemo-sorbent which absorbs sulfides as chemical compounds, like metal sulfides [13]. This sorbent also serves as anode in the fuel cell.

First, sulfide react with metal oxide embedded into electro-conductive carbon matrix to form metal sulfide.

The second step is elution in a fuel cell mode by the initial sulfide solution or by a supporting electrolyte. Thus, the formed metal sulfides are directly oxidized on the anode, the oxidation products are removed, and the sorption activity of the chemo-sorbent is restored. Thus, electromotive force is generated.

Using this approach, the amount of the captured sulfide depends on the amount of the active metal oxide in the matrix. So, one can regulate the fuel cell capacity according to the required power density.

On the other hand, we decided to use a gas-diffusion cathode with appropriate catalyst to enhance oxygen reduction, to avoid the adverse effect of the low oxygen solubility in aqueous solutions and the mass transfer limitations.

The gas-diffusion electrode (GDE) is a porous electrode where the solid catalyst is in contact with both liquid electrolyte and gas phase, as described in the literature [14-16].

GDEs have a structure that mainly consists of a super-hydrophobic layer (gas phase layer), a gas diffusion layer (solid phase layer) and a catalytic layer (liquid phase layer). The gas is transported to the catalytic bed through the gas diffusion bed [17]. At the same time, the gas diffusion layer prevents the gas diffusion channel from being covered due to electrolyte migration [18]. GDEs are naturally assumed to possess the properties of air permeability and hydrophobicity. Therefore, oxygen/air transport in the gas phase layer plays an important role in sulfate production [19]. The main function of the gas diffusion layer is to collect electrons, facilitating gas transport and chemical reactions, i.e. oxygen reduction in this case. The catalyst is supported on the surface of the catalytic layer, where oxygen can be reduced due to its hydrophilicity under the action of catalyst (solid phase) and electrolyte (liquid phase) [16].

There are some attempts to use gas-diffusion electrodes (GDE) for sulfite oxidation [20] and sulfide oxidation in liquid phase anode fuel cells [21, 22] showing good performance.

Therefore, a membraneless fuel cell was selected with a specially designed gas-diffusion cathode

containing cobalt and manganese compounds as catalyst.

The aim of this study is to demonstrate the combination of integrated preconcentration of sulfide on the anode serving also as sorbent and consequent electricity production in a liquid phase fuel cell with gas-diffusion cathode.

## MATERIALS AND METHODS

### *Materials*

Experiments with a sorbent used as anode were carried out. The sulfide solutions were prepared by sodium sulfide nona-hydrate ACS reagent  $\geq 98\%$  purity (Sigma-Aldrich production). All other chemicals used for analyses were of p.a. grade.

A sodium chloride solution in distilled water was used as a supporting electrolyte for the anodic compartment. The chosen sodium chloride concentration corresponds to the Black Sea water, i.e.,  $16 \text{ g dm}^{-3}$ . The pH of the initial solution varied between 7.3 and 12.6 depending on the chosen sulfide concentration from 20 to  $1200 \text{ mg dm}^{-3}$ .

The catalyst for the cathode was embedded in the gas-diffusion electrode (GDE). The catalyst consisted of oxides of manganese and cobalt, i.e.  $\text{MnCo}_2\text{O}_{4.5}$ . It was prepared by pyrolysis of ground apricot stones, soaked in acetates of the listed metals. The gas-diffusion electrode (GDE) was prepared in a way close to the method previously developed at the Institute of Electrochemistry and Energy Systems at the Bulgarian Academy of Sciences, described in [14] and later using Vulcan XC-72 R [10]. GDE consists of two layers - a gas-diffusion layer of  $50 \text{ mg cm}^{-2}$  of teflonized Vulcan XC-72 R (35 % Teflon) and an active layer of  $50 \text{ mg cm}^{-2}$  of  $\text{MnCo}_2\text{O}_{4.5}$  mixed with  $15 \text{ mg cm}^{-2}$  of Vulcan XC-72 R. Cobalt in combination with manganese in the resulting electrocatalytic mass plays an important role in the diffusion process. There is no evidence of decomposition of the carbon residue and/or passage of Co into solution. GDE works quite efficiently in both alkaline and neutral electrolytes.

The cathode area was  $12.5 \text{ cm}^2$ . The XRD-diagram of the catalyst is shown in Fig. 1. It consists of 47% MnO (manganosite) and 53% cobalt.

The chemo-sorbent was prepared by pyrolysis of waste soot from tire production, soaked in zinc acetate. Its XRD-diagram is shown in Fig. 2. The sorbent particles were of 0.1  $\mu\text{m}$  average size. The prepared chemo-sorbent is electro-conductive and thus it enlarges the apparent anode area.

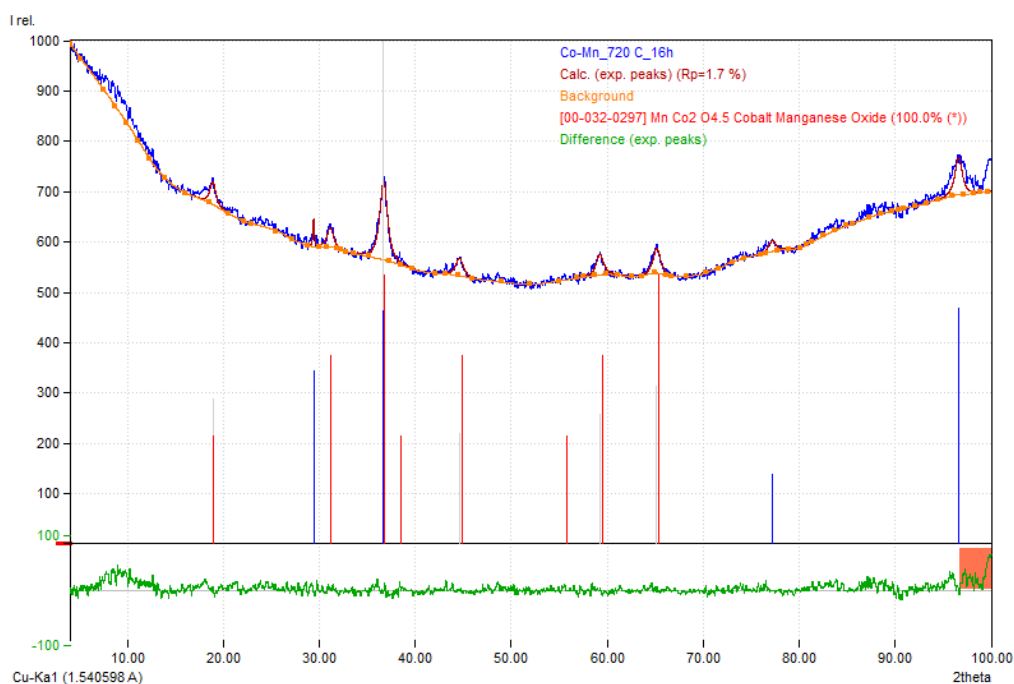


Figure 1. XRD-diagram of the prepared and used catalyst for cathode application.

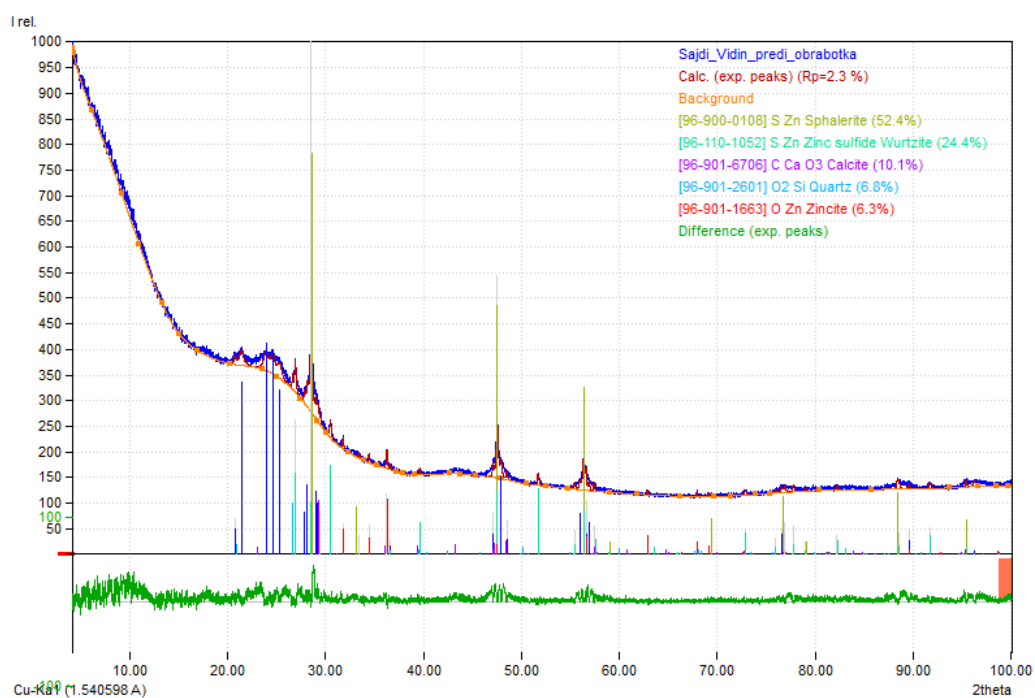
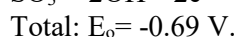
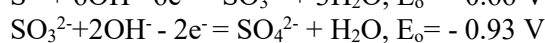
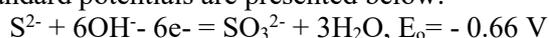


Figure 2. XRD-diagram of the prepared and used as anode chemo-sorbent containing zinc oxide and sulfide.

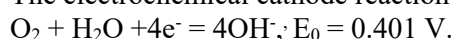
### Experimental design

The fuel cell consisted of a rectangular compartment of 370 cm<sup>3</sup> volume. The external gas diffusion electrode was mounted at one of the walls with access to the air outside. The anode compartment was packed with the sorbent. Graphite rods were used as contact anodes. Continuous processes for the anode compartment were studied with a feed flow rate of 0.300 dm<sup>3</sup> h<sup>-1</sup>.

The expected scheme of the fuel cell for the considered case is shown in Fig. 3. The anode reactions of consecutive sulfide to sulfate oxidation involving hydroxylic anion exchange with their standard potentials are presented below:



The electrochemical cathode reaction is:



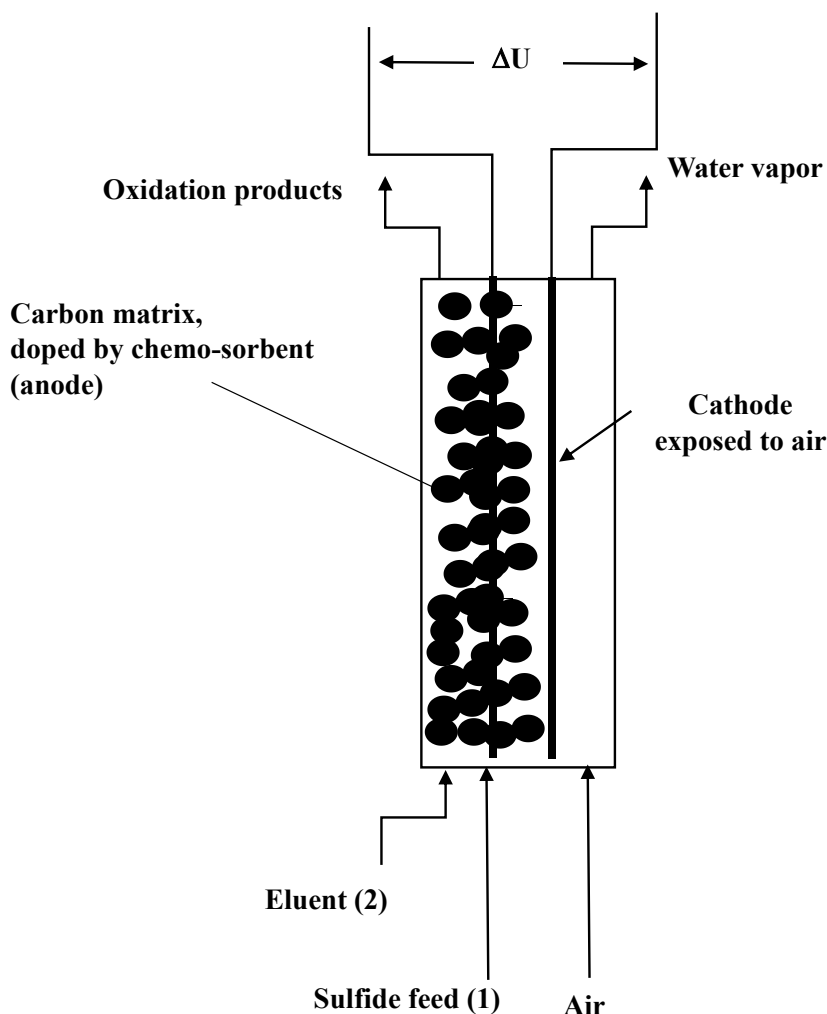


**Figure 3.** Scheme of the operation mode of membraneless sulfide-driven fuel cell.

Before the experiments, as a first step the chemo-sorbent in the anode compartment of the fuel cell was saturated for several hours with sulfide anions by continuous feeding with sulfide solutions of different concentrations, from 20 to 1200 mg dm<sup>-3</sup>. During the saturation the open circuit voltage (OCV) of the cell was monitored. Samples from the inlet and outlet solution were taken and analyzed for sulfide. The sorption capacity (wt.%) was calculated by the difference in inlet and outlet concentrations for the used flow rate. The sorption capacity was calculated as the sorbed amount of sulfide to a unit mass of the used chemo-sorbent. The saturation ended when the OCV value became practically constant. Then the sorbent was eluted in a fuel cell mode by a low-concentration solution of sulfide (ca. 20 g dm<sup>-3</sup>) in 16 g dm<sup>-3</sup> sodium chloride solution as supporting electrolyte. Thus, electromotive force was generated together with regeneration of the chemo-sorbent by *in situ* anode oxidation of the retained sulfide. Some experiments at higher inlet concentrations of sulfide (i.e. from 200 up to 1200 mg dm<sup>-3</sup>) in the eluting solution were made too. The

continuous feeding was accomplished by a peristaltic pump.

During the continuous experiments the inlet sulfide solution was purged by nitrogen prior to supplying it to the fuel cell to avoid or at least to minimize the parasite bulk oxidation of sulfide.

Samples from the inlet and outlet flows were taken regularly and analyzed quantitatively for sulfide, and qualitatively for sulfite, sulfate, thiosulfate and polysulfide. Fourteen experiments were carried out both using the same gas-diffusion cathode and chemo-sorbent. After each saturation, polarization curves were taken at different current densities varying the external resistance of the circuit. Then, experiments on the cell discharge through selected ohmic resistance by continuous feed by sulfide solutions were carried out. The electric current values were calculated by the Ohm's law from the measured cell voltage and the external resistance.

The amounts of oxidized sulfide were calculated from the evaluated electric current according to the Faraday's law and compared to the converted sulfide according to the analyses.

$$\frac{m}{t} = \frac{M_i}{nF}, m = \frac{M}{nF} \int_0^t i. dt \quad (1)$$

where:  $i$ —electric current, A;  $m$ —mass of reacting substance, g;  $t$ —time, s;  $M$ —molar mass of reacting substance, g;  $n$ —number of exchanged electrons;  $F$  Faraday constant = 96,484 C mol<sup>-1</sup>.

The number of exchanged electrons  $n$  depends on the reactions on the anode. In the case of sulfide oxidation these reactions are very sensitive to the sulfide concentration and a large variety of exchanged electrons for different electrochemical reactions are possible. We shall constraint ourselves to some of them which are more probable at lower sulfide concentrations, as in our case. Table 1, excerpt of a comprehensive one [23] is shown below.

**Table 1.** Short excerpt of sulfide oxidation reactions, taken from [23]

No.	Reversible anode reaction	Number of exchanged electrons, $n$	Standard electrode potential, V, 25°C
1	$\text{SO}_4^{2-} + \text{H}_2\text{O} + 2\text{e} = \text{SO}_3^{2-} + 2\text{OH}^-$	2	-0.91
2	$\text{SO}_3^{2-} + 3\text{H}_2\text{O} + 6\text{e} = \text{S}^{2-} + 6\text{OH}^-$	6	-0.66
3	$\text{S}_2^{2-} + 2\text{e} = 2\text{S}^{2-}$	1	-0.524
4	$\text{S}_3^{2-} + 2\text{e} = \text{S}^{2-} + \text{S}_2^{2-}$	1	-0.49
5	$\text{S} + 2\text{e} = \text{S}^{2-}$	2	-0.48
6	$\text{S}_2\text{O}_3^{2-} + 6\text{H}^+ + 8\text{e} = 2\text{S}^{2-} + 3\text{H}_2\text{O}$	4	-0.006

**Table 2.** Comparison of the oxidized amount of sulfide according to the current yields to that determined by analyses of the inlet and outlet flows at different inlet concentrations of sulfide. Elution flow rate 0.3 dm<sup>3</sup> h<sup>-1</sup>.

Run No.	Inlet concentration, mg dm <sup>-3</sup>	Amount of oxidized sulfide, mg 1 exchanged electron	Amount of oxidized sulfide, mg 2 exchanged electrons	Amount of oxidized sulfide, mg 8 exchanged electrons	Amount of oxidized sulfide, analysis, mg	Oxidized forms found in the outlet flow
1	239.7	8.92	4.96	1.12	14.01	Polysulfide, sulfite, sulfate
2	24.9	15.0	7.5	1.88	8.96	Sulfite
3	23.5	16.7	8.35	2.09	5.88	Sulfite
4	1195	41.01	20.5	5.13	501.85	Polysulfide, sulfite, sulfate
5	24.7	16.8	8.4	2.1	13.4	Sulfite, sulfate
6	21.8	5.28	2.64	0.66	7.96	Sulfite, sulfate
7	19.5	6.24	3.12	0.78	6.64	Sulfite, sulfate

## Analyses

Sulfide was analyzed photometrically with N,N-dimethyl-*p*-phenylenediamine in the presence of Fe(III) to form methylene blue [24]. Sulfate and sulfite were qualitatively proven by the addition of barium chloride. Barium sulfite is soluble in acid medium whereas barium sulfate is not. The presence of thiosulfate was checked by the addition of ferric salts leading to purple color. Polysulfides give a colored clear solution (yellow for S<sub>2</sub><sup>2-</sup> and green for S<sub>3</sub><sup>2-</sup>) with deposition of sulfur in acid medium.

During all experiments the acidity of the inlet and outlet flows was monitored by measuring the pH. A glass electrode coupled with a Seven easy pH-meter (Mettler Toledo) was used.

## RESULTS AND DISCUSSION

### Chemo-sorption capacity

The summarized results for the oxidized sulfide calculated by the Faraday's law for different anode reactions compared to the results of the chemical analysis are shown in Table 2. There, the detected products of sulfide oxidation are presented too.

The results for the sorption capacity and the limit open circuit potential of the fuel cell are shown in Fig. 4. It is obvious that both quantities are stable at continuous use for long period of time (i.e. about three months and 14 experiments).

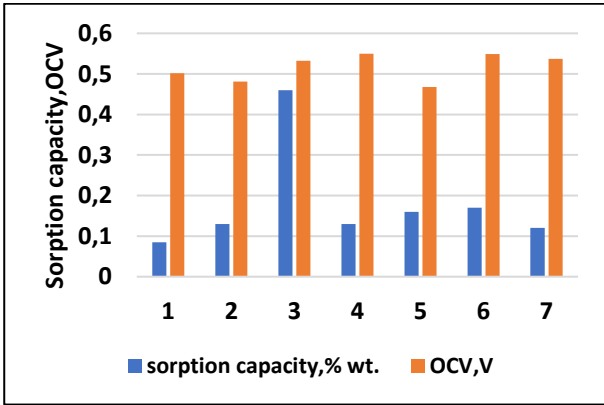


**Figure 4.** Sorption capacities and open circuit voltage during saturation of chemo-sorbent by sulfide at different concentrations.

Except for run 3, all sorption capacities are of the same order of magnitude, i.e.  $0.16 \pm 0.04$  wt.%. The open circuit voltage at saturation negligibly differs depending on the concentration of saturation. Its average value is  $0.54 \pm 0.02$  V.

An attempt was made to find a correlation between the concentration of saturation and the sorption capacity and/or the open circuit voltage, OCV. For the sorption capacity the correlation coefficient was 0.03, whereas for the open circuit voltage it was 0.0001. It means that both are practically independent of the concentration of saturation and chemo-sorption practically occurs.

A kinetic curve for the OCV variation during sorbent saturation is shown in Fig. 5.

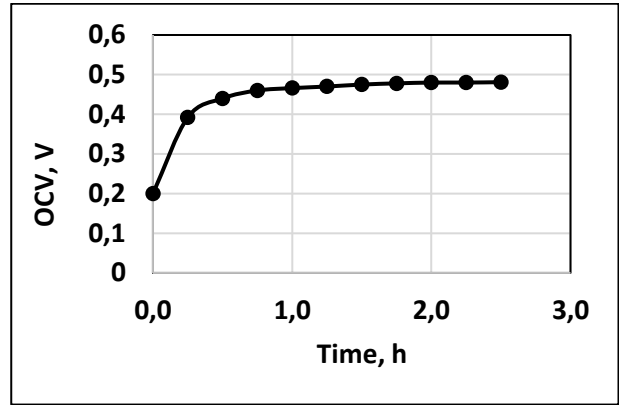


**Figure 5.** Variation of open circuit voltage (OCV) during saturation with sulfide (run 2). Sulfide concentration of saturation  $230 \text{ mg dm}^{-3}$ . Flow rate  $0.3 \text{ dm}^3/\text{h}$ .

#### Fuel cell performance

A polarization curve for continuous feed, obtained after preliminary saturation by sulfide for one experiment, is shown in Fig. 6.

There is a strictly linear dependence between the current density and the cell voltage with a negligible overpotential (about 1 mV) and practically no mass transfer effects at higher current densities.

The results for the cell discharge through external resistance of  $10 \Omega$  for the same experiment (run 2, Table 2) are shown in Figs 7 a, b. It is evident that after a transient process in the beginning all measured quantities remain constant and stable for 4 hours. The same effect was observed for all experiments, no matter of the feeding concentration of sulfide.

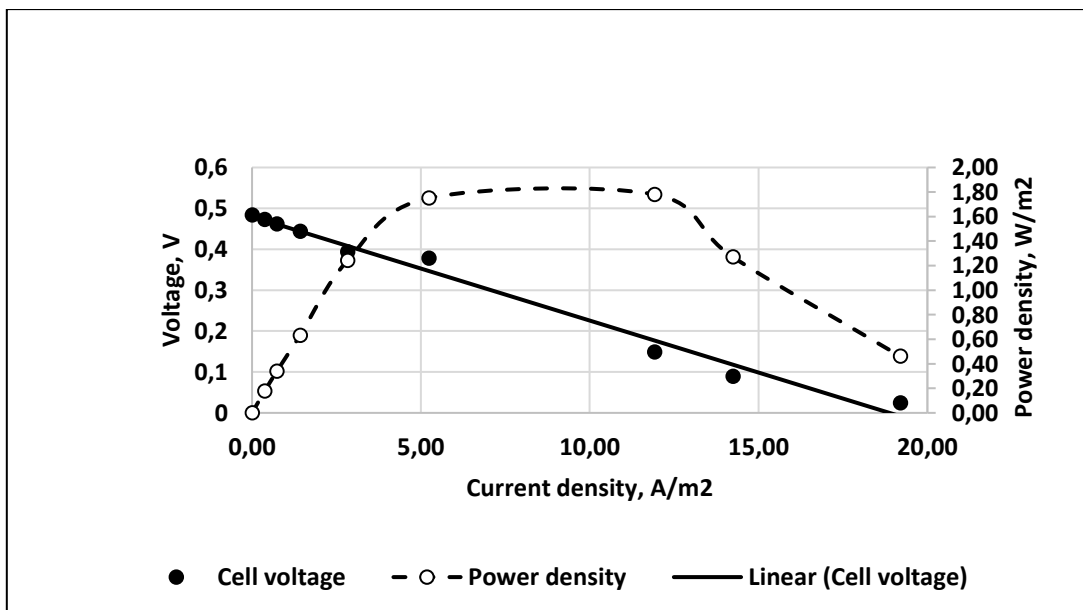


**Figure 6.** Polarization curve for run 2 after saturation. Sulfide concentration  $24.9 \text{ mg dm}^{-3}$ . Continuous process. Flow rate  $0.3 \text{ dm}^3/\text{h}$ .

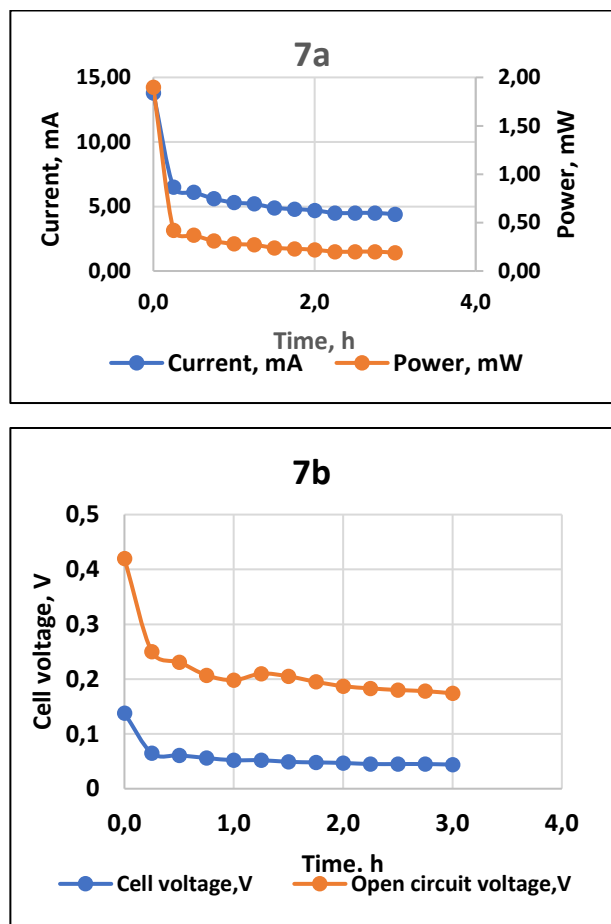


**Figure 7.** Discharge curves for run 2. Sulfide concentration  $24.9 \text{ g dm}^{-3}$ . Continuous process. Flow rate  $0.3 \text{ dm}^3/\text{h}$ . External ohmic resistance  $10 \Omega$ . 7a – curves for electric current and power generated in the fuel cell. 7b – open circuit voltage (OCV) and cell tension during the discharge experiment.

The calculated depleted amounts of sulfide from the current yields according to the Faraday law for each experiment are compared to the amounts determined from the analyses of the inlet and outlet sulfide concentrations, *cf.* Table 2.

There are experiments (runs 1, 4) where the calculated amounts for oxidized sulfide by the Faraday’s law are much less than those determined by analysis. This fact can be explained in the cases of high inlet concentrations of sulfide by parallel parasite reactions in the bulk and by polysulfide formation through competitive anode reactions at excessive amounts of sulfide, e.g. rows 3 and 4 in Table 1. An indication for this conclusion is the polysulfide detected in the outlet flow. Next, too large apparent amounts of depleted sulfide at high inlet concentrations are determined by analyses in the outlet flow, compared to those calculated from the current efficiency, *cf.* rows 1 and 4, Table 2. For those cases the calculated amounts according to the

Faraday’s law correspond to numbers of exchanged electrons less than unity. However, one must keep in mind that many competitive reactions of sulfide oxidation may occur on the anode at high sulfide concentration. On the other hand, neither thiosulfate nor elemental sulfur were detected in the outlet stream.

In the cases of low sulfide feed concentration, the electrochemical oxidation of sulfide to sulfite and sulfate prevails, *cf.* rows 2, 3, 5-7, Table 2. Electrochemical reactions involving exchange of two electrons are sulfide-to-sulfur oxidation and sulfite to sulfate oxidation, *cf.* Table 1, rows 1 and 5. However, no sulfur was detected in the outlet flows. Therefore, it is likely to expect partial oxidation of sulfide to sulfite in the bulk with a subsequent full electrochemical oxidation to sulfate on the anode, reactions 1 and 2 in Table 1. The comparison of the oxidized amounts of sulfite to sulfate on the anode to those determined by analysis shows fuel cell efficiency from 33% (run 6) to 83.7% (run 2) if electrochemical reaction (1) in Table 1 is assumed. The direct electrochemical oxidation of sulfide to sulfate, involving exchange of 8 electrons is not likely. Probably, it takes place in a two-step consecutive scheme, *cf.* reactions 2 and 1 in Table 1.

#### Current and power densities

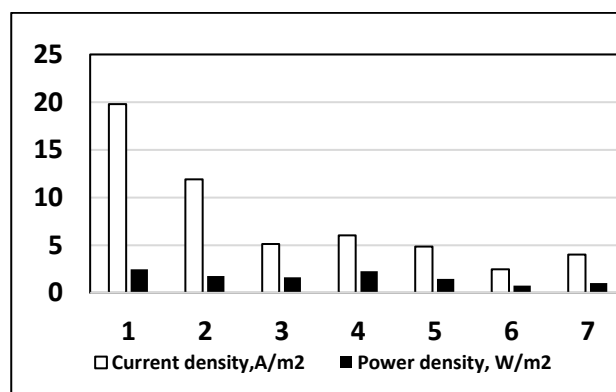


**Figure 8.** The maximum power and the corresponding current density for the runs presented in Table 1.

The maximum power and the corresponding current densities were determined from the polarization curves for each experiment. They are shown in Fig. 8. The highest current density, i.e.  $19 \text{ A/m}^2$  was observed in the first experiment (run 1). The current density diminishes with the consecutive runs reaching almost stable value ( $4.5 \text{ A/m}^2$ ) after the third run, not depending on the inlet sulfide concentration. This decrease can be explained by some wash-out of the active component of the sorbent, i.e. ZnS in the freshly prepared sorbent. This conclusion was confirmed by XRD analyses of the sorbent prior to and after five experiments, *cf.* Table

3. It is seen that wurtzite is considerably removed after five runs and there is a slight decrease in the content of zincite.

**Table 3.** Percentage shares of the components in the anode chemo-sorbent before and after five runs by XRD-analyses.

Component	Before experiments, content %	After five runs, content %
ZnS, sphalerite	52.4	53.1
ZnS, wurtzite	24.4	16.6
CaCO <sub>3</sub>	10.1	10.3
SiO <sub>2</sub>	6.8	15.0
ZnO, zincite	6.3	5.06

The situation for the maximum power densities is similar. It starts with a value of 2.46 W/m<sup>2</sup> for the first run and slowly decreases to about 1 W/m<sup>2</sup> for the last two runs.

The comparison with the available data in the literature shows somewhat lower results than those reported by Wei *et al.* [20]. They measured current and power densities of 60 A/m<sup>2</sup> and 6 W/m<sup>2</sup> in a sulfite/air fuel cell. Wei & Wu [21] presented results for sulfide/air fuel cell with maximum current density of 200 A/m<sup>2</sup> and maximum power density of 9 W/m<sup>2</sup>. In this study elemental sulfur was produced. In another study [22] current density of 65 A/m<sup>2</sup> and power density of 2.6 W/m<sup>2</sup> were reported. The difference can be sought in the fuel cell design and the used catalyst in the GDE. In [22] a silver catalyst directly synthesized on the cathode has been used whereas in [20] a Pt-Pd catalyst has been tested.

## CONCLUSIONS

From the obtained results the following conclusions can be drawn:

1. Consecutive chemo-sorption of sulfide and elution with simultaneous anode oxidation with electromotive force generation are proposed as a method for enrichment of low-concentration sulfide solutions. The method is demonstrated in a sulfide-driven fuel cell. The anode is composed of electro-conductive carbon particles doped by zinc oxide, serving as sorbent and catalyst.

2. Gas diffusion electrode doped by cobalt and manganese compounds is successfully used as cathode in order to eliminate the mass transfer limitations and the low solubility of oxygen in aqueous solutions.

3. The electrodes show good stability after fourteen consecutive runs. The sorption capacity remains stable and practically independent of the concentration of sulfide in the saturation solution.

4. The fuel cell parameters (current and power densities) are stable for the whole set of experiments

and of the same order of magnitude as some data in the literature for fuel cell performance with sulfite and sulfide as a fuel.

5. The anode processes are sensitive to the sulfide concentration in the feeding solution. Sulfite and sulfate are the oxidation products at low sulfide concentrations. At higher concentrations in the feed polysulfide are formed because of competitive anode reactions at excess of sulfide and due to bulk reactions.

**Acknowledgement:** This work was supported by the Fund for Scientific Research, Bulgaria, Project KP-06-H67/3.

## REFERENCES

1. A. Midilli, M. Aya, A. Kale T. N. Veziroglu, *Int. J. Hydrogen Energy*, **32**, 117 (2007).
2. I. I. Volkov, L. N. Neretin. Hydrogen Sulfide in the Black Sea, in: A. G. Kostianoy, A. N. Kosarev, (eds) *The Black Sea Environment. The Handbook of Environmental Chemistry*, vol. 5Q, Springer, Berlin, Heidelberg, 2007. [https://doi.org/10.1007/698\\_5\\_083](https://doi.org/10.1007/698_5_083)
3. N. A. Azarenkov, B. V. Borts, V. I. Tkachenko, *East Eur. J. Phys.*, **1**, 4 (2014).
4. S. A. Naman, I. E. Ture, T. N. Veziroglu, *Int. J. Hydrogen Energy*, **33**, 6577 (2008).
5. S. Gunes-Durak, S. Kapkin, *Int. J. Hydrogen Energy*, **50**, 706 (2024). <https://doi.org/10.1016/j.ijhydene.2023.11.141>
6. R. Simova, R. Velichkova, M. Uzunova, R. Angelova, P. Stankov, K. Atanasov, *Polityka Energetyczna – Energy Policy Journal*, **26**, 183 (2023). doi: 10.33223/epj/163372
7. P. K. Dutta, K. Rabaey, Z. Yuan, J. Keller, *Water Res.*, **42**, 4965 (2008)
8. K. Kim, J.-I. Han, *Int. J. Hydrogen Energy*, **39**, 7142 (2014).
9. V. Beschkov, E. Razkazova-Velkova, M. Martinov, S. Stefanov, *Appl. Sci.*, **8** (10), 1926 (2018). doi:10.3390/app8101926.
10. D. Uzun, E. Razkazova-Velkova, K. Petrov, V. Beschkov, *Bulg. Chem. Commun.*, **47**, 859 (2015). doi:10.1088/1742-6596/2710/1/012034.
11. C. Romero Cotrino, Control of Hydrogen Sulfide from Groundwater Using Packed-Bed Anion Exchange and Other Technologies, Master's Thesis, University of South Florida, Tampa, FL, USA, 2006, p. 8.
12. C. Romero Cotrino, A. D. Levine, P. Amitzoglou, J. S. Perone, *Florida Water Resources J.*, November, 22 (2007).
13. L. Ljutzkanov, V. Beschkov, S. Stefanov, E. Razkazova-Velkova, Method for electrical energy production from aqueous solutions containing hydrogen sulfide and/or sulfide, Application for BG patent, reg. No.BG/P/2022/113529.

14. I. Iliev, J. Mrha, S. Gamburgzev, A. Kaisheva, *J. Power Sources*, **17**, 345 (1986).
15. J. Xi, J. Jing, J. Gu, J. Guo, Y. Li, M. Zhou, *J. Environ. Chem. Eng.* **10**, 107882 (2022). doi.org/10.1016/j.jece.2022.107882
16. M. Zhu, H. Ge, X. Xu, Q. Wang, *Heliyon*, **4**, E00729 (2018). <https://doi.org/10.1016/j.heliyon.2018.e00729>].
17. E. Murawski, N. Kananizadeh, S. Lindsay, A. M. Rao, S. C. Popat, *J. Power Sources*, **481**, 228992 (2021).
18. K. U. Hansen, F. Jiao, *Joule* **5**, 754 (2021) doi: 10.1016/j.joule.2021.02.005
19. J. Uzun, E. Razkazova–Velkova, K. Petrov, V. Beschkov, *J. Appl. Electrochem.*, **46**, 943 (2016) doi: 10.1007/s10800-016-0979-4.
20. J. Wei, Y. Gu, X. Wu, *Sustainable Energy Fuels*, **5**, 3666 (2021). doi: 10.1039/D1SE00659B
21. J. Wei, X. Wu, *ACS Environ. Sci. Technol. Water*, **3**, 3428 (10) (2023). <https://doi.org/10.1021/acsestwater.3c00436>. 2023
22. J. Wei, Y. Liu, X. Wu, *Separ. Purif. Technol.*, **329**, 125234 (2024).
23. A.M. Suhotin, Guidebook on Electrochemistry, Himia, Leningrad, Russia, 1981 (in Russian).
24. E. Rees, T. D. Gyllenpetz, A. B. Docherty, *Analyst*, **96**, 201 (1971).

## Resin Tulsion-8052 MP – a novel and ecofriendly catalyst for Knoevenagel reaction in aqueous medium

S. A. Sadaphal, S. B. Sapkal\*, S. S. Gadekar, J. J. Gawai

*Department of Chemistry, School of Basic and Applied Sciences, Mahatma Gandhi Mission University Chhatrapati Sambhajinagar, (MS), 431003, India*

Received: June 17, 2024; Revised: August 08, 2024

The novel catalyst resin Tulsion-8052 MP is an acid catalyst that promotes the Knoevenagel reaction of aldehydes with active methylene compounds in an ecofriendly way. The reaction was performed in an aqueous medium with a catalytic amount of resin. This method is advantageous, as the catalyst is easy to operate, recyclable, ecofriendly, and economical.

**Keywords:** Resin Tulsion-8052 MP catalyst, Aldehydes, Active methylene compounds, Knoevenagel reaction, Water, Recyclable catalyst.

### INTRODUCTION

In the past decades, the wave of catalytical transformation in the Knoevenagel reaction has peaked due to its unique carbon-carbon bond formation ability. This method is widely used and impacted on several fields such as pharmaceuticals, fine chemicals, functional polymers, and biologically active materials [1-5]. Knoevenagel reaction products or specially benzyldene malononitrile (BMN) derivatives are widely used pioneers in several areas of organic chemistry due to their biological activities [6-15].

Recently, due to the advantageous nature of BMN, there is an extensive need to focus on its synthesis using a greener approach. The best way to perform organic transformation is using water as a solvent due to its universal solvent property [16]. The aqueous medium is selective, environmentally friendly, cheap and non-hazardous [17-19]. For Knoevenagel condensation, recently scientists reported an aqueous medium reaction with different catalysts such as, zeolitic imidazolate framework-8 (ZIF-8) [20], acylhydrazone-linked COF catalyst (TH-MT-COF-OH) [21], chiral 4-MeO-pyridine (MOPY) [22], magnesium [23], boron carbon nitride (BCN) [24], amine-rich nickel(II)-xerogel [25], Pd nanoparticles supported on 2-(aminomethyl) phenol-modified boehmite [26], as well as catalyst-free reaction [27]. All the above methods show some drawbacks like use of expensive catalysts, tedious method of catalyst preparation, workups, and high-temperature reactions. To overcome these problems, our team introduced a simple, ecofriendly, cheap,

stable, and recyclable method for the Knoevenagel reaction using the resin Tulsion-8052 MP catalyst.

There are some review articles [28] that give brief details on catalysts for Knoevenagel condensation such as heterogeneous catalysts, nitrogen-based catalysts, and metal-free sustainable nitrogen-based catalysts.

Resins are versatile materials used in various industries like pharmaceuticals [29], petrochemicals [30], and polymers [31]. Resin catalysts almost never encompass the use of toxic solvents, which avoids environmental risks, endorses the efficiency of the reaction and decreases waste production [32-34]. The catalyst's acidic sulfonic functional group promotes the activation of the carbonyl group in the aldehydes to be involved in carbon-carbon bond formation. This mechanism ensures high selectivity and enables the carbon-carbon bond formation in excellent yields. Moreover, the resin Tulsion-8052 MP can be easily recycled, making it a cost-effective and bearable choice for large-scale synthesis.

In consideration of all the advantageous activities of the resin in organic transformation, we herein performed a Knoevenagel reaction of aldehydes with active methylene compounds using the resin Tulsion-8052 MP.

### EXPERIMENTAL

#### *General information*

All reagents, active methylene compounds, and aldehydes were obtained from commercial suppliers and were not purified. Tulsion-8052 MP

\* To whom all correspondence should be sent:  
E-mail: [ssapkal@mgmu.ac.in](mailto:ssapkal@mgmu.ac.in)

resin was obtained from Thermax Limited. Melting points were recorded in open capillaries and were uncorrected. Thin-layer chromatography was performed on preparatory glass coated by silica gel 60F254 measuring 20×20 cm from Merck. IR spectra were recorded on an FT/IR-410 type (A) spectrophotometer in KBr. <sup>1</sup>H and <sup>13</sup>C NMR spectrum was measured in CDCl<sub>3</sub>/DMSO-d<sub>6</sub> solution on a Bruker spectrophotometer. Electron spray ionization mass spectra (ES-MS) were recorded on a Water-Micro mass Quattro-II spectrometer.

#### General procedure

Knoevenagel condensation reaction was carried out in a four-neck glass round-bottom flask of 100 mL volume on a magnetic stirrer. The stirrer speed was controlled by a speed regulator. The round-bottom flask was placed in a water bath at room temperature. In a typical run, 1.0 mmol of aromatic aldehyde (limiting reactant) and 1.0 mmol of active methylene group compound were charged in the round-bottom flask with water (5V) as solvent. The Tulsion-8052 MP catalyst loading was 10 mol%. The reaction mixture was stirred at room temperature. After completion of the reaction, the reaction mass was filtered and purified by using ethanol. Obtained wet purified product was dried and analysed.

#### Recovery of resin

After completion of Knoevenagel condensation reaction, the catalyst was undissolved and remained on the filter paper during ethanol purification of product. After ethanol washing (2×5 mL) of the recovered catalyst, the latter was collected, air dried to remove solvent traces of ethanol and used in further cycles.

#### Spectral data of the synthesized compounds

**2-Benzylidenemalononitrile (3a):** white solid, m. p. 80-82°C (ref. 39); FT-IR (KBr, cm<sup>-1</sup>): 3035, 2223, 1568; <sup>1</sup>H-NMR (400 MHz, CDCl<sub>3</sub>), δppm 7.88 (d, *J*=7.05 Hz, 2H), 7.76 (s, 1H), 7.61 (t, *J*=7.6 Hz, 2H); <sup>13</sup>C NMR (101 MHz, CDCl<sub>3</sub>) δppm 159.9, 134.5, 131.0, 130.5, 129.5, 113.8, 112.5, 82.8; MS: *m/z* = 154.05 (M<sup>+</sup>).

**2-(2-Nitrobenzylidene) malononitrile (3b):** yellow solid, m. p. 138-140°C (ref. 40); FT-IR (KBr, cm<sup>-1</sup>): 3062, 2951, 2226, 1728, 1623, 1579, 1524; <sup>1</sup>H NMR (400 MHz, CDCl<sub>3</sub>), δppm 8.45 (s, 1H), 8.32 (d, 1H, *J*=8 Hz), 7.90-7.88 (m, 1H), 7.86 – 7.82 (m, 2H); <sup>13</sup>C NMR (101 MHz, CDCl<sub>3</sub>) δppm 158.2, 146.9, 134.5, 133.3, 130.8, 126.4, 125.6, 112.2, 110.1, 88.2; MS: *m/z* = 200 (M<sup>+</sup>).

**2-(4-Nitrobenzylidene) malononitrile (3c):** light yellow solid, m. p. 160-162°C (ref. 39); FT-IR (KBr, cm<sup>-1</sup>): 3030, 2262, 1622, 1536, 989; <sup>1</sup>H-NMR (400MHz, CDCl<sub>3</sub>): δppm 8.40 (d, *J*= 8.7 Hz, 2H), 8.77 (d, *J*= 8.8 Hz, 2H), 7.90 (s, 1H); <sup>13</sup>C NMR (101 MHz, CDCl<sub>3</sub>) δppm 159.8, 137.7, 134.5, 133.8, 117.5, 112.2, 111.7, 88.0; MS: *m/z* = 200 (M<sup>+</sup>).

**2-(4-Methylbenzylidene) malononitrile (3d):** white solid, m. p. 132-134°C (ref. 39); FT-IR (KBr, cm<sup>-1</sup>): 3030, 2982, 2852, 2220, 1605, 1571, 1557, 1513; <sup>1</sup>H NMR (400 MHz, CDCl<sub>3</sub>), δppm 7.88 (d, 2H, *J*=8 Hz), 7.77 (s, 1H), 7.36 (d, 2H, *J*=8 Hz), 2.43 (s, 3H); <sup>13</sup>C NMR (101 MHz, CDCl<sub>3</sub>) δppm 159.4, 146.3, 130.5, 130.8, 128.1, 114.2, 112.3, 81.4, 22.2; MS: *m/z* = 169 (M<sup>+</sup>).

**2-(4-Methoxybenzylidene) malononitrile (3e):** white solid, m. p. 112-114°C (ref. 39); FT-IR (KBr, cm<sup>-1</sup>): 3032, 2986, 2848, 2218, 1615, 1566, 1549, 1510; <sup>1</sup>H NMR (400 MHz, CDCl<sub>3</sub>), δppm 7.94 (d, 2H, *J*=8.8 Hz), 7.68 (s, 1H), 7.11 (d, 2H, *J*=8.8 Hz), 3.96 (s, 3H); <sup>13</sup>C NMR (101 MHz, CDCl<sub>3</sub>), δppm 165.0, 158.8, 133.0, 124.2, 114.9, 114.3, 113.1, 78.0, 56.1; MS: *m/z* = 185 (M<sup>+</sup>).

**2-(2-Chlorobenzylidene) malononitrile (3f):** light beige solid, m. p. 96-98°C (ref. 39); FT-IR (KBr, cm<sup>-1</sup>): 3047, 2224, 1638, 1585, 1164, 757; <sup>1</sup>H NMR (400 MHz, CDCl<sub>3</sub>), δppm 8.25 (s, 1H), 8.19 (d, *J* = 7.9 Hz, 1H), 7.58 – 7.52 (m, 2H), 7.48 – 7.40 (m, 1H); <sup>13</sup>C NMR (101 MHz, CDCl<sub>3</sub>) δppm: 158.4, 133.1, 131.8, 129.9, 129.6, 113.4, 112.3, 83.5; MS: *m/z* = 190 (M<sup>+</sup>).

**2-(4-Chlorobenzylidene) malononitrile (3g):** White solid, m. p. 161-163°C (ref. 39); FT-IR (KBr, cm<sup>-1</sup>): 3033, 2923, 2227, 1636, 1585, 1407; <sup>1</sup>H NMR (400 MHz, CDCl<sub>3</sub>), δppm 7.89 (d, 2H, *J* = 8.4 Hz), 7.76 (s, 1H), 7.54 (d, 2H, *J* = 8.7 Hz); <sup>13</sup>C NMR (101 MHz, CDCl<sub>3</sub>) δppm: 158.7, 141.6, 132.2, 130.5, 129.6, 113.8, 112.7, 83.7; MS: *m/z* = 190 (M<sup>+</sup>).

**2-(4-Fluorobenzylidene) malononitrile (3h):** Brown solid, m. p. 125-127°C (ref. 41); FT-IR (KBr, cm<sup>-1</sup>): 3038, 2920, 2229, 1596, 1575; <sup>1</sup>H NMR (400 MHz, CDCl<sub>3</sub>), δppm 7.8 (s, 1H), 6.76–6.71 (m, 2H), 7.2–7.4 (m, 2H); <sup>13</sup>C NMR (101 MHz, CDCl<sub>3</sub>) δppm: 165.0, 158.7, 134.0, 128.1, 117.1, 113.6, 112.6, 81.8; MS: *m/z* = 172 (M<sup>+</sup>).

**2-(4-Hydroxybenzylidene) malononitrile (3i):** pale yellow solid, m. p. 187-189°C (ref. 39); FT-IR (KBr, cm<sup>-1</sup>): 3353, 3080, 2922, 2226, 1611, 1581; <sup>1</sup>H NMR (400 MHz, DMSO-d<sub>6</sub>) δppm 11.05 (s, 1H), 8.30 (s, 1H), 7.89 (d, *J*= 8.5 Hz, 2H), 6.97 (d, *J*= 8.5 Hz, 2H); <sup>13</sup>C NMR (101 MHz, DMSO-d<sub>6</sub>) δppm 164.5, 161.0, 134.4, 123.2, 117.1, 115.6, 114.7, 75.4; MS: *m/z* = 171 (M<sup>+</sup>).

**2-(4-Bromo-2-fluorobenzylidene) malononitrile (3j):** off white solid, m. p. 150-152°C (no ref.); FT-

IR (KBr,  $\text{cm}^{-1}$ ): 3100, 2225, 1589, 963, 956, 816;  $^1\text{H}$  NMR (400 MHz,  $\text{CDCl}_3$ )  $\delta$  8.15 (t,  $J=8.0$  Hz, 1H), 8.00 (s, 1H), 7.46 (dd,  $J=21.0, 9.2$  Hz, 2H);  $^{13}\text{C}$  NMR (101 MHz,  $\text{CDCl}_3$ )  $\delta$ ppm 162.04, 159.42, 149.97, 130.52, 129.13, 128.95, 120.4, 120.22, 118.35, 113.11, 112.03, 84.96; MS:  $m/z = 252$  ( $\text{M}^+$ ).

*Ethyl 2-cyano-3-(2-nitrophenyl)acrylate (3k)*: white solid, m. p. 99-101°C (ref. 39); FT-IR (KBr,  $\text{cm}^{-1}$ ): 3097, 3032, 2989, 2944, 2225, 1721, 1618, 1590, 1568, 1496;  $^1\text{H}$  NMR (400 MHz,  $\text{CDCl}_3$ )  $\delta$ ppm 8.69 (s, 1H), 8.25 (d,  $J=8.1$  Hz, 1H), 7.84-7.76 (dd,  $J_1=7.5$  Hz,  $J_2=7.5$  Hz, 2H), 7.69 (t,  $J=7.5$  Hz, 1H), 3.39 (q,  $J=7.0$  Hz, 2H), 1.39 (t,  $J=7.2$  Hz, 3H);  $^{13}\text{C}$  NMR (101 MHz,  $\text{CDCl}_3$ )  $\delta$ ppm 178.5, 161.0, 153.4, 147.2, 134.3, 132.4, 130.5, 127.9, 125.3, 108.8, 72.0, 14.2; MS:  $m/z = 247$  ( $\text{M}^+$ ).

*Ethyl 2-cyano-3-(4-nitrophenyl)acrylate (3l)*: white solid, m. p. 167-169°C (ref. 39); FT-IR (KBr,  $\text{cm}^{-1}$ ): 3092, 3045, 2996, 2942, 2224, 1723, 1615, 1588, 1550, 1493;  $^1\text{H}$  NMR (400 MHz,  $\text{CDCl}_3$ )  $\delta$ ppm 8.34 (d,  $J=9.0$  Hz, 2H), 8.29 (s, 1H), 8.12 (d,  $J=8.7$  Hz, 2H), 4.43 (q,  $J=3.6$  Hz, 2H), 1.42 (t,  $J=7.0$  Hz, 3H);  $^{13}\text{C}$  NMR (101 MHz,  $\text{CDCl}_3$ )  $\delta$ ppm 161.1, 151.5, 149.7, 137.0, 131.1, 124.0, 114.5, 107.1, 63.4, 14.1; MS:  $m/z = 247$  ( $\text{M}^+$ ).

*Ethyl-2-cyano-3-(p-tolyl)acrylate (3m)*: white solid, m. p. 88-90°C (ref. 39); FT-IR (KBr,  $\text{cm}^{-1}$ ): 3028, 2216, 1724, 1595, 1298, 847;  $^1\text{H}$  NMR (400 MHz,  $\text{CDCl}_3$ )  $\delta$ ppm 8.19 (s, 1H), 7.88 (d,  $J=8.0$  Hz, 2H), 7.28 (d,  $J=7.9$  Hz, 2H), 4.35 (q,  $J=7.1$  Hz, 2H), 2.41 (s, 3H), 1.37 (t,  $J=7.1$  Hz, 3H);  $^{13}\text{C}$  NMR (101 MHz,  $\text{CDCl}_3$ )  $\delta$ ppm 162.6, 155.4, 144.7, 131.4, 130.3, 129.1, 115.9, 101.0, 62.4, 21.6, 14.3; MS:  $m/z = 216$  ( $\text{M}^+$ ).

*Ethyl-2-cyano-3-(4-methoxyphenyl)acrylate (3n)*: white solid, m. p. 75-77°C (ref. 39); FT-IR (KBr,  $\text{cm}^{-1}$ ): 3028, 2217, 1718, 1590, 1325, 1191, 825;  $^1\text{H}$  NMR (400 MHz,  $\text{CDCl}_3$ )  $\delta$ ppm 8.18 (s, 1H), 7.33-8.03 (m, 4H), 4.2-4.46 (q,  $J=7.20$  Hz, 2H), 2.35 (s, 3H), 1.35-1.41 (2t,  $J=7.20$  Hz, 6H);  $^{13}\text{C}$  NMR (101 MHz,  $\text{CDCl}_3$ )  $\delta$ ppm 163.3, 154.2, 132, 131.86, 127, 119.41, 115.5, 101.83, 61.42, 14.0; MS:  $m/z = 232$  ( $\text{M}^+$ ).

*Ethyl-3-(2-chlorophenyl)-2-cyanoacrylate (3o)*: off-white solid, m. p. 52-55°C (ref. 39); FT-IR (KBr,  $\text{cm}^{-1}$ ): 3038, 2222, 1728, 1609, 1285, 760;  $^1\text{H}$  NMR (400 MHz,  $\text{CDCl}_3$ )  $\delta$ ppm 8.55 (s, 1H), 7.78 (d,  $J=8.1$  Hz, 1H), 7.52 (m,  $J=7.6$  Hz, 2H), 7.22 (m, 1H), 4.31 (q,  $J=7.1$  Hz, 2H), 1.30 (t,  $J=7.1$  Hz, 3H);  $^{13}\text{C}$  NMR (101 MHz,  $\text{CDCl}_3$ )  $\delta$ ppm 162.3, 153.1, 139.6, 132.0, 129.8, 129.7, 115.4, 103.3, 62.9, 14.1; MS:  $m/z = 236$  ( $\text{M}^+$ ).

*Ethyl-3-(4-chlorophenyl)-2-cyanoacrylate (3p)*: white solid, m. p. 90-92°C (ref. 39); FT-IR (KBr,  $\text{cm}^{-1}$ ): 3036, 2220, 1725, 1564, 795;  $^1\text{H}$  NMR (400 MHz,

$\text{CDCl}_3$ )  $\delta$ ppm 8.20 (s, 1H), 7.94 (d,  $J=8.8$  Hz, 2H), 7.48 (d,  $J=8.8$  Hz, 2H), 4.39 (q,  $J=7.2$  Hz, 2H), 1.40 (t,  $J=7.2$  Hz, 3H);  $^{13}\text{C}$  NMR (101 MHz,  $\text{CDCl}_3$ )  $\delta$ ppm 162.2, 129.9, 115.3, 103.0, 139.1, 153.2, 129.5, 132.3, 62.6, 14.3; MS:  $m/z = 236$  ( $\text{M}^+$ ).

*Ethyl-2-cyano-3-(2,4-dichlorophenyl) acrylate (3q)*: white solid, m. p. 79-81°C (ref. 39); FT-IR (KBr,  $\text{cm}^{-1}$ ): 3031, 2223, 1728, 1614, 1585, 826, 775;  $^1\text{H}$  NMR (400 MHz,  $\text{CDCl}_3$ )  $\delta$ ppm 8.61 (s, 1H), 8.25 (d, 1H,  $J=8.8$  Hz), 7.58 (d,  $J=1.6$  Hz, 1H), 7.40-7.38 (m, 1H), 4.34 (q,  $J=7.2$  Hz, 2H), 1.44 (t,  $J=7.2$  Hz, 3H);  $^{13}\text{C}$  NMR (101 MHz,  $\text{CDCl}_3$ )  $\delta$ ppm 161.5, 149.6, 139.3, 137.2, 130.4, 130.2, 128.2, 127.9, 114.6, 106.3, 63.0, 14.0; MS:  $m/z = 270$  ( $\text{M}^+$ ).

*Ethyl (E)-2-cyano-3-(4-hydroxyphenyl) acrylate (3r)*: light yellow solid, m. p. 170-174°C (ref. 39); FT-IR (KBr,  $\text{cm}^{-1}$ ): 3279, 2987, 2230, 1722, 1586;  $^1\text{H}$  NMR (300 MHz,  $\text{DMSO-d}_6$ )  $\delta$ ppm 10.87 (s, 1H), 8.24 (s, 1H), 7.99-8.02 (d,  $J=9$  Hz, 2H), 6.95-6.98 (d,  $J=9$  Hz, 2H), 4.26-4.33 (q,  $J=9$  Hz, 2H), 1.28-1.33 (t,  $J=6$  Hz, 3H);  $^{13}\text{C}$  NMR (101 MHz,  $\text{DMSO-d}_6$ )  $\delta$ ppm 163.5, 163.1, 155.2, 134.5, 123.0, 117.0, 116.9, 97.5, 62.4, 14.5; MS:  $m/z = 218$  ( $\text{M}^+$ ).

*2-(Furan-2-ylmethylene)malononitrile (3s)*: White solid, m. p. 68-70°C (ref. 42); FT-IR (KBr,  $\text{cm}^{-1}$ ): 3431, 3015, 2220, 1685, 1609, 1418, 1214, 1066, 761;  $^1\text{H}$  NMR (400 MHz,  $\text{CDCl}_3$ ):  $\delta$ ppm 7.55 (s, 1H), 7.37 (d,  $J=3.7$  Hz, 1H), 7.83 (d,  $J=1.6$  Hz, 1H), 6.74 (q,  $J=2.2$  Hz, 1H);  $^{13}\text{C}$  NMR (101 MHz,  $\text{CDCl}_3$ ):  $\delta$ ppm 149.2, 148.5, 143.0, 130.3, 115.8, 112.1, 80.2; MS:  $m/z = 145$  ( $\text{M}^+$ ).

*2-(Thiophen-2-ylmethylene)malononitrile (3t)*: brown solid, m. p. 96-98°C (ref. 43); FT-IR (KBr,  $\text{cm}^{-1}$ ): 3429, 3020, 2219, 1675, 1431;  $^1\text{H}$  NMR (400 MHz,  $\text{CDCl}_3$ ):  $\delta$ ppm 7.93 (s, 1H), 7.50 (d,  $J=4.8$  Hz, 1H), 7.16 (d,  $J=3.6$  Hz, 1H), 6.60 (t,  $J=4.3$  Hz, 1H);  $^{13}\text{C}$  NMR (101 MHz,  $\text{CDCl}_3$ ):  $\delta$ ppm 150.1, 141.5, 135.3, 129.8, 128.1, 113.7, 112.5, 76.2; MS:  $m/z = 161$  ( $\text{M}^+$ ).

*2-(Pyridin-4-ylmethylene) malononitrile (3u)*: off white solid, m. p. 99-101°C (ref. 41); FT-IR (KBr,  $\text{cm}^{-1}$ ): 3029, 2223, 1610, 1548, 1403;  $^1\text{H}$  NMR (400 MHz,  $\text{CDCl}_3$ ):  $\delta$ ppm 7.69 (d,  $J=5.3$  Hz, 2H), 7.83 (s, 1H), 8.88 (d,  $J=5.3$  Hz, 2H);  $^{13}\text{C}$  NMR (101 MHz,  $\text{CDCl}_3$ ):  $\delta$ ppm, 157.6, 151.7, 137.2, 123.4, 113.3, 112.4, 85.0; MS:  $m/z = 155$  ( $\text{M}^+$ ).

## RESULTS AND DISCUSSION

The resin Tulsion-8052 MP catalyzed the Knoevenagel reaction and contributed to its ecofriendly profile due to the aqueous media used. By eliminating the need for organic solvents, this method significantly reduces waste generation and eliminates potential environmental hazards. This green approach aligns with the principles of sustainable chemistry, making it an attractive option for researchers and industries alike. In continuation with our current research contribution in the field of green chemistry [35-38], herein we introduce the resin Tulsion-8052 MP for Knoevenagel reaction as a novel, recyclable, economical, and green catalyst (Scheme 1).



**Scheme 1.** Schematic diagram of Knoevenagel reaction using resin Tulsion-8052 MP catalyst in aqueous medium.

Resin Tulsion-8052 MP catalyst has a unique operating behavior in both aqueous and organic media making it preferred over other reported catalysts. The nature of the catalyst is granular with light brown in color. This catalyst has an active sulphonic acid functional group which participates in reaction to promote reaction. Resin Tulsion-8052 MP catalysts have a wide operating temperature range from 0-80°C. This catalyst has a large pore structure with a high exchange capacity (1.95meq/ml.min). At the outset of the research, the first step is to benchmark Tulsion-8052 MP for condensation of benzaldehyde with malononitrile with another resin catalyst, to verify the catalyst's activity. The reaction was carried out in an aqueous medium at room temperature using Tulsion-8052 MP resin, and the results obtained are summarized in Table 1.

Tulsion-8052 MP resin was the best-performing resin for the Knoevenagel condensation between benzaldehyde and malononitrile in terms of yields, moreover, other acidic resins required longer reaction times. Basic ion exchange resin showed a lower yield in Knoevenagel condensation in aqueous medium.

**Table 1.** Comparative data of resin catalysts in Knoevenagel reaction of benzaldehyde and malononitrile.<sup>a</sup>

Entry	Catalyst	Main functional group	Total exchange capacity (meq/mL)	Reaction Time (h)	Yield (%) <sup>b</sup>
1	Indion 225 H	Sulfonic acid	1.8	2.0	90
2	Dowex 50WX2	Sulfonic acid	0.6	5.0	85
3	Dowex 50WX8	Sulfonic acid	1.7	2.0	89
4	Amberlite IR120 H	Sulfonic acid	1.8	1.5	92
5	Amberlite IRC-50	Carboxylic acid	3.5	1.0	90
6	Amberlite FPA53	Tertiary amines	1.6	2.5	88
7	Amberlite IRA-96	Tertiary amine	1.3	4	86
8	Amberlite IRA-410	Dimethylethanol ammonium	1.25	4	84
9	Tulsion-8052 MP	Sulfonic acid	1.95	1.0	95
10	Tulsion-A-74 MP	Quaternary ammonium	1.0	6.0	75

<sup>a</sup> Reaction conditions: benzaldehyde 1a (1 mmol), malononitrile 2a (1mmol), catalyst (10 mol%), water (5V), <sup>b</sup> isolated yields.

Amberlite IR120 H showed comparatively decent results but not as good as Tulsion-8052 MP resin in aqueous medium. Hence, we chose Tulsion-8052 MP resin for reaction.

Further, various solvents' impact on the condensation of benzaldehyde with malononitrile as a model reaction in the presence of resin Tulsion-8052 MP catalyst (10 mol%) was studied. The solvent-free reaction takes a longer reaction conversion time and yields a sluggish reaction mass. After isolation, the obtained yield is 89% in solvent-free condensation. Then the reaction was carried out in the aprotic solvent acetonitrile and the realized

reaction worked at room temperature but affianced slightly longer reaction time. In protic solvents ethanol and methanol used for condensation reactions the reaction goes well within 4 h and yield was optimum. Based on the solvent study, we moved to carry out a reaction using water. In this practice it was found that the reaction goes well with higher yield and shorter reaction time under stirring at room temperature. Further, we studied the impact of applied temperature on reaction and carried out reactions at 45-50°C, 60-65°C, 75-80°C, which showed no drastic change in reaction time, as well as in yield. Whereas at reflux temperature the reaction

time was shorter, a slight decrease in yield was observed due to catalyst deactivation, as shown in Table 2. Based on Table 2, there is no need for a higher temperature to carry out the reaction using water as a solvent and the reaction can go smoothly at room temperature without loss of product. Also, there is no big change in reaction time by increasing the reaction temperature up to 80°C.

Further, the concentration of the resin Tulsion-8052 MP catalyst in condensation reaction was optimized. In trial run experiments with benzaldehyde (1mmol), malononitrile (1 mmol), and water (5V) were used and the reaction was performed with different concentrations of resin catalyst under stirring at room temperature and the obtained results are summarized in Table 3.

**Table 2.** Solvent with temperature comparison study for condensation of benzaldehyde and malononitrile in presence of resin catalyst.<sup>a</sup>

Entry	Solvents <sup>b</sup>	Temp. (°C)	Reaction time (h)	Yield (%) <sup>c</sup>
1	--	RT	6.0	89
2	Acetonitrile	RT	6.0	81
3	Ethanol	RT	4.0	88
4	Methanol	RT	4.0	86
5	Water	RT	1.0	95
6	Water	45-50°C	1.0	95
7	Water	60-65°C	1.0	96
8	Water	75-80°C	1.0	97
9	Water	Reflux	0.5	90
10	Water	65°C	2.0	94 <sup>[Ref. 44]</sup>
11	Water	50°C	2.0	99 <sup>[d, Ref. 45]</sup>

<sup>a</sup> Reaction conditions: benzaldehyde 1a (1 mmol), malononitrile 2a (1mmol), resin Tulsion-8052 MP (10 mol%), <sup>b</sup>solvent volume (5V), <sup>c</sup>isolated yields, <sup>d</sup>use of excess of malononitrile (1.2 eq.) in reaction.

**Table 3.** Resin Tulsion-8052 MP concentration study in the condensation reaction of benzaldehyde and malononitrile under stirring<sup>a</sup> at room temperature.

Entry	Catalyst conc. (mol%)	Reaction time (h)	Yield (%) <sup>b</sup>
1	--	2.0	14
2	2.5	2.0	46
3	5.0	2.0	78
4	7.5	2.0	87
5	10	1.0	95
6	15	1.0	95
7	20	1.0	97

<sup>a</sup> Reaction conditions: benzaldehyde 1a (1 mmol), malononitrile 2a (1mmol), water (5V), <sup>b</sup>isolated yields.

By varying catalyst concentration, it was found that without a catalyst in an aqueous medium reaction performance is very poor and isolated yield is only 14%. With the increase in catalyst concentration in mol % an increase in yield was

observed which clearly points to the indispensable catalyst role. Based on the above observations, a 10 mol % catalyst concentration with respect to concerned aldehydes was chosen.

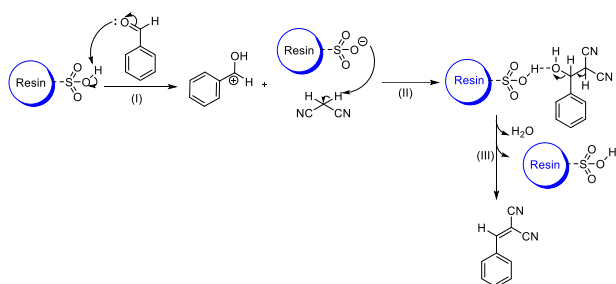
A similar procedure was applied to screen different derivatives for condensation reaction of aldehydes 1(a-k) and active methylene group compounds 2(a and b: CN/CN and CN/COOEt respectively) in the presence of resin Tulsion-8052 MP catalyst in water at room temperature to get condensed products 3(a-r) as shown in Table 4.

**Table 4.** Resin Tulsion-8052 MP catalysed Knoevenagel condensation reaction at room temperature in aqueous medium.

Entry	R	X/Y	Product	Reaction Time (h)	Yield (%) <sup>a</sup>
1	Ph	CN/CN	3a	1.0	95
2	2-NO <sub>2</sub> Ph	CN/CN	3b	1.0	91
3	4-NO <sub>2</sub> Ph	CN/CN	3c	1.0	93
4	4-CH <sub>3</sub> Ph	CN/CN	3d	1.0	96
5	4-CH <sub>3</sub> O Ph	CN/CN	3e	1.0	98
6	2-Cl Ph	CN/CN	3f	1.0	95
7	4-Cl Ph	CN/CN	3g	1.0	96
8	4-F Ph	CN/CN	3h	1.0	94
9	4-OH Ph	CN/CN	3i	1.0	97
10	4-Br, 2-F Ph	CN/CN	3j	1.5	92
11	2-NO <sub>2</sub> Ph	CN/COOEt	3k	2.0	97
12	4-NO <sub>2</sub> Ph	CN/COOEt	3l	2.0	99
13	4-CH <sub>3</sub> Ph	CN/COOEt	3m	2.0	92
14	4-CH <sub>3</sub> O Ph	CN/COOEt	3n	2.0	93
15	2-Cl Ph	CN/COOEt	3o	2.5	95
16	4-Cl Ph	CN/COOEt	3p	2.5	95
17	2,4-Cl Ph	CN/COOEt	3q	3.5	96
18	4-OH Ph	CN/COOEt	3r	2.0	94
19	Furan-2-yl	CN/CN	3s	4.0	95
20	Thien-2-yl	CN/CN	3t	4.5	94
21	Pyrid-2-yl	CN/CN	3u	4.0	91

<sup>a</sup>Isolated yields.

The activity of the catalyst was markedly better in the case of all synthesized aldehyde derivatives and the obtained results were excellent, compared to other reported methods. To understand the reaction pathway, the probable mechanism for Knoevenagel condensation reaction with resin Tulsion-8052 MP catalyst is illustrated in Scheme 2.



**Scheme 2.** Probable mechanistic pathway for the Knoevenagel condensation reaction of benzaldehyde and malononitrile catalyzed by the resin catalyst.

Based on the probable mechanism, the carbonyl functional group on benzaldehyde was activated by the resin sulphonyl acidic proton to proceed reaction of condensation (Scheme 2, step I). Afterward, the next step continues with the attack of the carbanionic anion on the polarized carbonyl group and a new intermediate was generated (Scheme 2, step II).

Meanwhile, with the recovery of the catalyst and loss of water molecules (Scheme 2, step III), the final product is obtained. Therefore, based on the proposed mechanism, one can say that the catalyst can be recycled and reused.

To confirm the reusability of the resin catalyst an experiment was performed with 4-methoxy benzaldehyde (1e) and malononitrile (2a) in water (5V) and Tulsion-8052 MP (10 mol%) at room temperature as shown in Table 5.

In the recycle experiment, after completion of reaction, crude product was isolated by filtration and the wet solid forwarded for crystallization using ethanol. During crystallization a clear solution was obtained which was filtered through filter paper to get recovered catalyst on the surface of the filter paper. After ethanol washing, the recovered catalyst was air dried to remove solvent traces of ethanol and used for the next cycles.

**Table 5.** Tulsion-8052 MP reusability experimental data<sup>a</sup>

Entry	Catalyst cycles	Yield (%) <sup>b</sup>
1	fresh	98
2	1	98
3	2	96
4	3	95
5	4	92
6	5	91

<sup>a</sup> Reaction conditions: 4-methoxy benzaldehyde 1e (1 mmol), malononitrile 2a (1mmol), water (5V). <sup>b</sup> Isolated yields.

According to the results in Table 5, the catalyst slightly lost its activity and yield after the 3<sup>rd</sup> run as compared to fresh use. Catalyst can be recycled for five sequential runs not losing much activity.

Representative condensates were structurally elucidated and confirmed. The developed method is easy to operate and provides products of high purity.

## CONCLUSION

Resin Tulsion-8052 MP catalyst is active, recyclable, economical and easy to operate in Knoevenagel condensation of aromatic aldehydes with active methylene compounds. The reaction proceeds at room temperature in aqueous medium, which makes it ecofriendly. This method has operationally simple work-up procedure, and completes within a shorter time to offer excellent yield. No toxic solvents were used which leads to a green approach for condensation reactions.

**Acknowledgement:** The authors are thankful to The Head, Department of Chemistry, School of Basic, and Applied Sciences, Mahatma Gandhi Mission University Chhatrapati Sambhajinagar, (MS), INDIA for providing laboratory facilities.

## REFERENCES

- H. I. Aljaddua, M. S. Alhumaimess, H. M. Hassan, *Arab. J. Chem.* **15**, 103588 (2022).
- K. Cai, W. Tan, N. Zhao, H. He, *Cryst. Growth Des.* **20**, 4845 (2020).
- B. M. Trost, *Comp. Org. Syn., Pergamon Press, Oxford*, **2**, 341 (1991).
- S. Ramesh, F. Devred, D. P. Debecker, *Chemistry Select*, **5**, 300 (2020).
- F. Freeman, *Chem. Rev.*, **80**, 329 (1980).
- L. F. Tietze, *Chem. Rev.*, **96**, 115 (1996).
- Q. Hu, X. L. Shi, Y. Chen, X. Han, P. Duan, W. Zhang, *J. Ind. Eng. Chem.*, **54**, 75 (2017).
- S. S. Maltsev, M. A. Mironov, V. A. Bakulev, *Mendeleev Commun.*, **16**, 201 (2006).
- S. A. Khan, A. M. Asiri, R. M. Rahman, S. A. Elroby, F. M. S. Aqlan, M. Y. Wani, K. Sharma, *J. Hetero. Chem.*, **54**, 3099 (2017).
- A. Sidhu, J. R. Sharma, M. Rai, *Ind. J. Chem. Sect. B Org. Med. Chem.*, **49**, 247 (2010).
- R. K. Gopalakrishna Panicker, S. Krishnapillai, *Tetrahedron Lett.*, **55**, 2352 (2014).
- M. M. H. Bhuiyan, K. M. M. Rahman, M. A. Alam, M. M. Mahmud, *Pak. J. Sci. Ind. Res. A: Phys. Sci.*, **56**, 131 (2013).
- S. Alwarappan, S. Boyapalle, A. Kumar, C. Z. Li, S. Mohapatra, *J. Phys. Chem.*, **116**, 6556 (2012).
- A. S. Fouda, Y. A. El-Awady, O. M. Abo-El-Enein, F. A. Azizah, *Anti-Corros. Method. M.*, **55**, 317 (2008).
- M. Almasi, V. Zelenak, M. Opanasenko, J. Cejka, *Dalton Trans.*, **43**, 3730 (2014).
- M. Cortes-Clerget, J. Yu, J. R. A. Kincaid, P. Walde, F. Gallou, B. H. Lipshutz, *Chem. Sci.*, **12**, 4237 (2021).
- U. M. Lindstrom, *Chem. Rev.*, **102**, 2751 (2002).
- C. Wei, C. J. Li, *J. Am. Chem. Soc.*, **125**, 9584 (2003).

19. S. Narayan, J. Muldoon, M. G. Finn, V. V. Fokin, H. C. Kolb, K. B. Sharpless, *Angew. Chem. Int. Edn.*, **44**, 3275 (2005).
20. M. Sayed, A. Soliman, H. N. Abdelhamid, *J. Solid State Chem.*, **332**, 124534 (2024).
21. Y. Xu, B. Tian, R. Zhang, P. Li, J. Hu, Z. Chen, *Micropor. Mesopor. Mat.*, **366**, 112959 (2024).
22. R. Kluga, A. Kinens, E. Suna, *A Eur. J.*, **30**(10), e202301136 (2024).
23. P. L. Kalar, K. Jain, S. Agrawal, S. Khan, R. Vishwakarma, A. Shivhare, M. M. Deshmukh, K. Das, *J. Org. Chem.*, **88**(24), 16829 (2023).
24. G. Xu, H. Zheng, X. Zhang, W. Li, L. Zhou, L. Qin, *Mol. Catal.*, **549**, 113447 (2023).
25. E. Saha, H. Jungi, S. Dabas, A. Mathew, R. Kuniyil, S. Subramanian, J. Mitra, *Inorg. Chem.*, **62**(37), 14959 (2023).
26. R. Zhang, T. Chen, G. Wang, Y. Guan, A. Rehemam, Z. Chen, J. Hu, *Catal. Lett.*, **153**(6), 1807 (2023).
27. Q. Liu, X. Chen, N. Yu, Y. Li, K. He, W. Zheng, Y. Zhou, K. Jiang, L. Yang, Y. Wei, *Catalysis*, **13**(9), 5795 (2023).
28. (a) J. N. Appaturi, R. Ratti, B. L. Phoon, S. M. Batagarawa, I. U. Din, M. Selvaraj, R. J. Ramalingam, *Dalton Trans.*, **50**, 4445 (2021). (b) K. V. Beurden, S. D. Koning, D. Molendijk, J. V. Schijndel, *Green Chem. Lett. Rev.*, **13**(4), 349 (2020). (c) S. Johari, M. R. Johana, N. G. Khaligh, *Org. Biomol. Chem.*, **20**, 2164 (2022).
29. D. P. Elder, *J. Chem. Educ.*, **82**(4), 575 (2005).
30. M. J. Zohuriaan-Mehr, H. Omidian, *J. Macromolec. Sci. Part C- Polymer Rev.*, **40**(1), 23 (2000).
31. T. Ramakrishnan, M. D. M. Gift, S. Chitradevi, R. Jegan, P. S. H. Jose, H. N. Nagaraja, R. Sharma, P. Selvakumar, S. M. Hailegiorgis, *Adv. Mater. Sci. Eng.*, **2022**, 1 (2022).
32. Y. W. Rong, Q. H. Zhang, W. Wang, B. L. Li, *Bull. Kor. Chem. Soc.*, **35**(7), 2165 (2014).
33. H. Reymond, S. Vitas, S. Vernuccio, P. R. V. Rohr, *Ind. Eng. Chem. Res.*, **56**(6), 1439 (2017).
34. S. U. Tekale, S. S. Kauthale, R. P. Pawar, *J. Chil. Chem. Soc.*, **58**, 1619 (2013).
35. S. B. Sapkal, K. F. Shelke, B. B. Shingate, M. S. Shingare, *Tetrahedron Lett.*, **50**, 1754 (2009).
36. K. F. Shelke, S. B. Sapkal, G. K. Kakade, S. A. Sadaphal, B. B. Shingate, M. S. Shingare, *Green Chem. Lett. Rev.*, **3**, 17 (2010).
37. A. Sapkal, S. B. Sapkal, B. R. Madje, *Eur. Chem. Bull.*, **8**(11), 352 (2019).
38. S. S. Gadekar, R. A. Joshi, B. R. Madje, S. T. Salunke, S. B. Sapkal, *Results in Chem.*, **6**, 101074 (2023).
39. S. Wang, Z. Ren, W. Cao, W. Tong, *Synth. Commun.*, **31**(5), 673(2001).
40. R. Pal, T. Sarkar, *Int. J. Org. Chem.*, **4**, 106 (2014).
41. K. B. Badiger, K. Kamanna, *Org. Commun.*, **14**(1), 81 (2021).
42. H. B. Ammar, M. Chtourou, M. H. Frikha, M. Trabelsi, *Ultrason. Sonochem.*, **22**, 559 (2015).
43. P. Kudale, K. Gavali, D. Pinjari, G. Chaturbhuj, *Results in Chem.*, **5**, 100833 (2023).
44. F. Bigi, C. Quarantelli, *Curr. Org. Synth.*, **9**, 31 (2012).
45. V. Campisciano, F. Giacalone, M. Gruttadauria, *Chem. Cat. Chem.*, **14**, e202200696 (2022).

## Microbiologically influenced corrosion (MIC) - monitoring and prevention

E. Chorbadzhiyska<sup>1,2\*</sup>, D. Apostolova<sup>3</sup>, V. Dalgacheva<sup>4</sup>, M. Mitov<sup>1,2</sup>

<sup>1</sup>Department of Chemistry, South-West University "Neofit Rilski", Blagoevgrad, Bulgaria

<sup>2</sup>Innovative Center for Eco Energy Technologies, South-West University "Neofit Rilski", Blagoevgrad, Bulgaria

<sup>3</sup>University of Ljubljana, Faculty of Chemistry and Chemical Technology,  
Večna Pot 113, SI-1000 Ljubljana, Slovenia

<sup>4</sup>Department of Geography, Ecology and Environmental Protection, South-West University "Neofit Rilski",  
Blagoevgrad, Bulgaria

In memory of Mario Mitov

Received: July 23, 2024; Revised: September 04, 2024

Microbiologically influenced corrosion is the destruction (corrosion) of various metals, concrete structures and other structural materials in the presence of microorganisms. In this type of corrosion, the process takes place directly or indirectly under the influence of the metabolic activity of microorganisms. Corrosion of pipelines, in addition to deteriorating the integrity of the materials, also leads to environmental pollution. For this reason, it is of great importance to find suitable methods for research and protection against corrosion processes.

In this paper, we present different methods for assessment, monitoring and prevention of microbiologically influenced corrosion (MIC). Electrochemical methods are important for MIC assessment and monitoring due to their sensitivity, rapidity, and ability to provide real-time data. Different electrochemical methods are presented: polarization resistance (PR) method, linear sweep voltammetry (LSV) and electrochemical impedance spectroscopy (EIS).

**Keywords:** microbiologically influenced corrosion (MIC), polarization resistance (PR) method, linear sweep voltammetry (LSV), electrochemical impedance spectroscopy (EIS)

### INTRODUCTION

Microbiologically influenced corrosion (MIC) is the destruction of various metals, concrete structures and other structural materials in the presence of microorganisms. In this type of corrosion, the process takes place directly or indirectly under the influence of the metabolic activity of microorganisms. Damage caused by microbiologically influenced corrosion (MIC) leads to a reduction in the tensile strength of structural materials, their breaking point, workability and other important mechanical properties. Wastewater discharged from industrial enterprises and also from households is one of the main corrosive environments that attracts attention for its high toxicity. Corrosion of pipelines, in addition to deteriorating the integrity of the materials, also leads to environmental pollution. For this reason, it is of great importance to find suitable methods for research and protection against corrosion processes. MIC is a major problem facing global sewer structures and is a hotly debated topic. In general, four main causes are at the basis of corrosion processes - formation of hydrogen sulfide in waste steam, radiation and accumulation of gaseous hydrogen sulfide, generation of sulfuric acid and

deterioration of the structure of construction materials [1]. Water and sewage pipelines are made of different types of materials, divided into iron pipes (spherical cast iron, cast iron and steel), concrete pipes (reinforced concrete and pressure concrete pipes), ceramic-based pipes (bricks and clay) and plastic pipes (polyvinyl chloride, polyethylene) [2] (Fig.1).

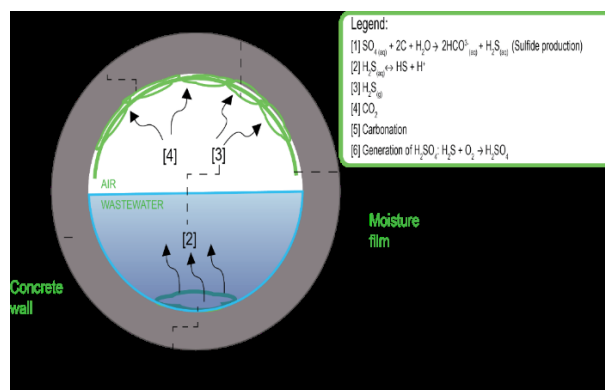


**Fig. 1.** Diagram of a pipeline and the processes taking place in it.

Appropriate application of electrochemical and surface analytical techniques is required for the detection and monitoring of MICs. This is crucial for

\* To whom all correspondence should be sent:  
E-mail: [elli\\_el@swu.bg](mailto:elli_el@swu.bg)

understanding the biocorrosion mechanisms of various structural metals and their alloys.

In bioelectrochemical systems (BES), in which extracellular electron transfer occurs between specific microorganisms and electrodes by mechanisms similar to those causing MIC in natural conditions, these processes have a positive effect with energy generation and wastewater treatment, but in natural conditions the same processes have a destructive effect on construction materials.

Corrosion in general and MIC in particular are among the most dangerous phenomena accompanying the operation of metal equipment in the field of industry. If a precise analysis is made of the economic losses that corrosion causes, the amount is likely to be in the millions.

Appropriate application of MIC detection and monitoring techniques is critical to understanding interaction mechanisms and selecting appropriate prevention and control techniques. In the present work, various methods are presented that can be successfully used for assessment, monitoring and prevention of MIC.

#### METHODS FOR ASSESSMENT AND MONITORING OF MIC

Despite the large number of publications on the subject, the evaluation and prevention of MIC are still difficult to realize. Electrochemical methods are a good solution to the problems posed, in view of the fact that they are useful both for laboratory and field studies. Detailed and reliable information on MIC can be obtained when different electrochemical techniques are combined [3].

##### *Open circuit potential (OCP)*

OCP involves measuring the natural potential of a metal in a specific environment without applying an external current or voltage. Based on the measurements, changes in the electrochemical environment due to microbial activity can be detected and the initiation of corrosion processes can be monitored.

##### *Corrosion potential ( $E_{corr}$ )*

Corrosion potential variation can be measured by determining the difference in voltage between the metal immersed in liquid medium and a suitable reference electrode [4-6]. Since OCP measurements change over time, it is important to estimate the effect of corrosion on the reaction depolarizers. A plot of potential as a function of time can be used [29]. An increase in OCP means depolarization of the cathode and increased corrosion; a drop in potential is evidence for decreased corrosion [7, 8].

*Electrochemical tests to monitor corrosion changes.* The disadvantage is that this technique provides little information because it needs a stable reference electrode (RE), but its surface is constantly changing due to microbial adhesion and biofilm formation. ( $E_{corr}$ ) cannot tell if the corrosion rate is decreasing or increasing. Measuring the polarization resistance ( $R_p$ ) together with ( $E_{corr}$ ) can give a more complete estimate of the MIC as it gives information on the changes in the anodic and cathodic partial reactions (they determine the corrosion rate) [3, 9].

##### *Tafel curves*

Increasing the applied potential in the noble direction away from the corrosion potential causes the specimen to behave as an anode. The anodic current increases with increasing noble potential, giving rise to the measured anodic curve. In theory, both the cathodic and the anodic curves should be linear when the applied potential,  $V$ , is plotted vs the logarithm of the current density,  $i$  ( $A/cm^2$ ), and the two curves should intersect at a point representing the corrosion potential and the corrosion current density. The measured log current vs potential curves both deviate from linearity in the vicinity of the corrosion potential; nevertheless, both often contain linear segments, sometimes referred to as Tafel regions. Extrapolating the linear segments of either the anodic or cathodic curves back to the corrosion potential yields the corrosion current density [10].

Taking polarization curves in Tafel coordinates is a fast and accurate technique for MIC analysis (Fig. 2) [8].

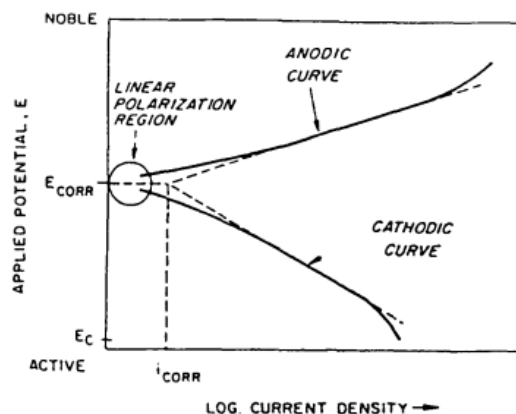


Fig. 2. Idealized polarization curve represented in Tafel coordinates [10]

The technique involves the displacement of the potential in an interval of  $\pm 250$  mV, respectively, from the OCP to record the current values of the system. The Tafel equation represents a kinetically controlled electrochemical half-reaction (1).

$$i = i_0 e^{\left[\frac{2.303(E-E_0)}{b}\right]} \quad (1)$$

In the presented equation, (i) is the current displayed by the system at an input potential (E). The equilibrium voltage is shown by (E<sub>0</sub>) and (b) is the reaction coefficient. The exchange current density is represented by (i<sub>0</sub>). The Tafel equation for both the positive and negative regions of the metal sample is combined to give the Stern-Geary equation (2):

$$i_{corr} = \frac{\beta_a \beta_c}{R_p 2.3(\beta_a + \beta_c)} \quad (2)$$

By the logarithm of (i) with (E) two curves are drawn - cathodic and anodic. Extrapolation of the linear region of the cathode and anode segments gives the value of corrosion current (i<sub>corr</sub>) for the system at their point of intersection. Tafel parameter values are useful in analyzing MICs. Corrosion rate (CR) and polarization resistance (R<sub>p</sub>) can be calculated from these parameters using the following equations (3) and (4):

$$CR(mmpy) = \frac{3272 i_{corr} E}{\rho A} \quad (3)$$

$$R_p = \frac{\beta_a \beta_c}{2.3(\beta_a + \beta_c)(i_{corr})} \quad (4)$$

In the above equations, the cathodic and anodic Tafel slopes are represented by (β<sub>a</sub>) and (β<sub>c</sub>), respectively. The equivalent weight of the corroded metal is represented by (E), (ρ) is density, and the area of the sample is represented by (A).

Each one of the parameters is affected by changes in the corrosion environment and allows predicting the corrosion behavior of the investigated metal. Tafel curves can provide information on the nature of the biofilm in terms of time and rate of corrosion, which can then be used to control MIC [11].

#### *Electrochemical impedance spectroscopy (EIS)*

Electrochemical impedance spectroscopy (EIS) is another important technique frequently used in MIC studies to understand microbial degradation processes. EIS has been shown to be a safe technique for studying microbial corrosion, as it does not cause damage to the biofilm and microbial population [11] and at the same time provides information on electrochemical processes at the surface, including the formation and destruction of biofilms and corrosion products.

EIS records impedance data as a function of frequency of an applied signal at a fixed electrode potential. To obtain a complete impedance spectrum, a wide frequency range must be investigated. The small signals required for EIS do not adversely affect the number, viability and activity of microorganisms

in the biofilm. The EIS data determine the polarization resistance (R<sub>p</sub>) values, which also allow the corrosion rate to be calculated. (R<sub>p</sub>) from EIS data is calculated by (5):

$$R_p = \sum(R_\Omega + R_p) - R_\Omega \quad (5)$$

where (R<sub>Ω</sub>) represents the ohmic resistance of the system.

EIS is a technique that provides information about the properties of the formed layer on the electrode surface by analyzing the polarization resistance values, allowing it to be used in MIC evaluation investigations [3].

#### *Polarization resistance method*

Polarization resistance method is based on the nature of the linear relationship between changes in the applied potential and the resultant current density, when the applied potentials are within about ± 10 mV of the corrosion potential. The technique is based on the assumption that the interface behaves as a simple resistor, whose magnitude is inversely proportional to the corrosion current [12]. The slope of the potential current curve is approximately linear and has units of resistance [10].

By measuring polarization resistance (R<sub>p</sub>), the corrosion rate of any metal can be continuously monitored. The polarization resistance can be determined from (6)

$$R_p = \left(\frac{dE}{di}\right)_{i=0} \quad (6)$$

where (R<sub>p</sub>) is the slope of the potential (E) versus the current density (i) at (E<sub>corr</sub>) where i = 0. The corrosion current density (i<sub>corr</sub>) is calculated from (R<sub>p</sub>) as follows (7), (8)

$$i_{corr} = \frac{B}{R_p} \quad (7)$$

where:

$$B = \frac{\beta_a \beta_c}{2.303(\beta_a + \beta_c)} \quad (8)$$

Accurate calculation of (i<sub>corr</sub>) for a given time requires simultaneous measurements of (R<sub>p</sub>) and anodic and cathodic slopes of the Tafel curve (β<sub>a</sub> and β<sub>c</sub>). Modern instruments are able to determine the exact values of (i<sub>corr</sub>). A simplification of the polarization resistance technique is the linear polarization technique, where the relationship between (E) and (i) is assumed to be linear in a narrow range around (E<sub>corr</sub>). Usually, only two points (E, i) are measured and (B) is assumed to have a constant value of about 20 mV. This approach is applicable to field tests and forms the basis of commercial corrosion rate monitoring.

The polarization resistance can also be defined as the DC limit of the EIS (i.e. at the low frequency limit).

Using the Stern-Geary theory (where the corrosion rate is inversely proportional to  $(R_p)$  at potentials close to  $(E_{corr})$ ) is valid for electron transfer-controlled conditions but not for diffusion-controlled systems as is often happening in MIC.

The advantage of the polarization resistance method is the quick and easy interpretation of the results and it shows a good correlation with the gravimetric method which measures the difference in weight before and after corrosion. Its disadvantage is that it is not applicable in cases of localized corrosion. The presence of a biofilm introduces additional electrochemical reactions that complicate the interpretation of linear polarization, thus potentially leading to nonlinear polarization behavior. This uncertainty is the reason for linking this method with other complementary techniques [3].

#### Cyclic voltammetry (CV)

Cyclic voltammetry (CV) involves cyclically changing the potential of the metal electrode and measuring the resulting current (Fig. 3). This method provides information on reversible and irreversible electrochemical reactions and is suitable for analyzing the redox behavior of microbial metabolites, as well as studying the electrochemical properties of biofilms [8].

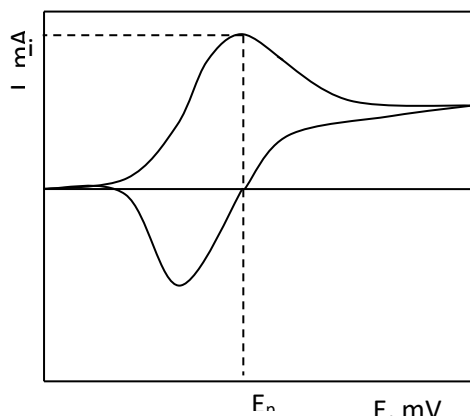


Fig. 3. Typical cyclic voltammetry

#### Integration with other techniques

Electrodes (working, reference, counter), used in all electrochemical techniques, measure the current and/or voltage in order to estimate the corrosion rate. The electrodes undergo changes due to the presence of microorganisms in the system and the thickness and character of the film formed on the electrode. That is why, for more comprehensive MIC assessment and monitoring, electrochemical

methods are often combined by themselves or with other methods, for example with:

*Surface analysis methods:* Scanning electron microscopy (SEM), energy dispersive X-ray spectroscopy (EDS) and X-ray photoelectron spectroscopy (XPS) to analyze the composition and morphology of biofilms and corrosion products.

SEM can be regarded as an effective method in the analysis of organic and inorganic materials on a nanometer to micrometer ( $\mu\text{m}$ ) scale. SEM works at a high magnification reaching to  $300,000\times$  and even  $1,000,000\times$  in producing very precise images of a wide range of materials [13].

Energy dispersive X-ray spectroscopy (EDS) works together with SEM to provide qualitative and semi-quantitative results. X-ray is generated when the electron beam, which is emitted from the gun, penetrates and interacts with the volume beneath the surface of the sample. Electrons entering the coulomb field of a specimen will decelerate and the loss of electron energy emits as a photon. Those photons have energies particular to specimen elements; these provide the SEM the capabilities and are called characteristic X-rays [14]. Both techniques together have the potential to supply fundamental information on material composition of scanned specimens, which could not be provided by common laboratory tests.

X-ray photoelectron spectroscopy is a surface-sensitive analytical technique in which X-rays bombard the surface of a material and the kinetic energy of the emitted electrons is measured. The two major characteristics of this technique that make it powerful as an analytical method are its surface sensitivity and its ability to reveal chemical state information from the elements in the sample [15].

*Microbiological analysis methods:* DNA sequencing, fluorescence microscopy, and culture-based techniques to identify and quantify the microorganisms involved in MIC.

There are four best known DNA sequencing techniques: the Sanger method, the Maxam and Gilbert method, the pyrosequencing<sup>TM</sup> method – DNA sequencing in real time by detection of released pyrophosphate (PPi) and single molecule sequencing with exonuclease (exonuclease digestion of a single molecule composed of a single strand of fluorescently labeled deoxynucleotides) [16]. An astounding potential exists for DNA sequencing methods to bring enormous change in genetic and biological research and to enhance our fundamental biological knowledge [17].

*Methods of chemical analysis:* chromatography and spectroscopy for the detection and quantification of microbial metabolites. Chromatography is based

on the principle that molecules in a mixture are applied onto the surface or into the solid, and fluid stationary phase (stable phase) is separating from each other while moving. Nowadays, chromatography is accepted as an extremely sensitive, and effective separation method [18]. There are various chromatographic methods like column chromatography, thin-layer chromatography (TLC), paper chromatography, gas chromatography, ion exchange chromatography, gel permeation chromatography, high-pressure liquid chromatography, and affinity chromatography [19].

Spectroscopy is a method of studying matter in which rays, sounds or particles emitted, absorbed, reflected or otherwise interacted with the object under study, are analyzed. Spectroscopic methods are widely used to identify substances by the spectrum they emit or absorb.

#### PREVENTION OF MICROBIOLOGICALLY INFLUENCED CORROSION

The assessment and prevention of microbiologically influenced corrosion (MIC) is of critical importance in many industries due to the serious economic consequences that this process can have. MIC causes significant economic losses due to the need for repairs, replacement of damaged parts and interruptions in the production process. MIC assessment helps to detect and reduce these costs early. On the other hand, sudden failures of equipment and structures caused by MIC pose a serious safety risk in various sectors such as oil and gas industry, chemical industry, etc. Regular assessment of MIC is a key factor to preventing accidents and protecting human life.

By monitoring MIC, companies can evaluate the effectiveness of their existing corrosion control systems and optimize them as needed. This includes the use of anti-corrosion coatings, cathodic protection and additives to inhibit microbial growth. Early detection and management of MICs can extend the life cycle of equipment and infrastructure by reducing the need for frequent replacements and repairs, resulting in cost savings.

Systems that are protected from MIC are more reliable and offer better performance. This is especially important in various industrial facilities. Last but not least, MIC can lead to the release of hazardous substances into the environment, which has serious environmental consequences.

MIC prevention helps to avoid such incidents and protect the environment. There are various methods of prevention of MIC [8, 20, 21].

Anti-corrosion coatings create a barrier between the metal surface and the corrosive environment,

preventing contact with microorganisms and corrosive agents. Epoxy and polyurethane coatings can be used, which provide excellent chemical resistance; inhibitor coatings contain substances that inhibit corrosion and growth of microorganisms, and others [22].

Another method is cathodic protection [21]. It reduces the corrosion potential of metals by electrochemical methods, making them less susceptible to corrosion. It is possible to use the so-called sacrificial anode – using anodes that are more reactive than the metal being corroded instead of the protected metal or applying an external electric current to suppress corrosion.

It is possible to influence the MIC by affecting the relevant microorganisms. Chemicals such as biocides and inhibitors are used that kill or inhibit the growth of microorganisms and thus prevent corrosion processes [23]. Microorganisms are able to dramatically alter the electrochemical conditions at the metal/solution interface through biofilm formation. These changes can range from inducing or accelerating corrosion to inhibiting corrosion. Any inhibitory action developed by bacteria may be achieved within the diverse and complex interactions between biofilm/corrosion products occurring on a biocontaminated metal surface [24].

The choice of materials is also important, the more corrosion resistant the better. This is a key factor in minimizing the risk of MIC. Well-known materials with high corrosion resistance are titanium [25, 26] and nickel alloys, as well as stainless steels with a high molybdenum content [27].

Regular maintenance and cleaning prevent the build-up of biofilms and corrosion products that contribute to MIC. Mechanical cleaning is used - removal of biofilms and corrosion products by brushing or jet cleaning; chemical cleaning, by using chemicals to dissolve deposits and kill microorganisms, or ultrasonic cleaning using ultrasonic waves to destroy biofilms.

Another important factor that can significantly reduce the risk of MIC is the control of environmental parameters (temperature, oxygen, pH) which can significantly reduce the risk of MIC. An interesting possibility is the use of competitive microorganisms or enzymes (to degrade biofilms) for corrosion control [3, 28].

#### CONCLUSION

Combining different electrochemical techniques to assess and control MIC leads to comprehensive understanding of MIC processes, which in turn leads to the development of effective prevention and control strategies.

The most effective prevention of microbiologically influenced corrosion is achieved by using a combination of chemical, physical and biological methods. By proper selection and application of these methods, it is possible to significantly reduce the risk of MIC.

The assessment and prevention of microbiologically influenced corrosion is essential to maintain the durability, safety and efficiency of industrial equipment and infrastructure. By applying appropriate monitoring techniques and preventive measures, economic losses can be significantly reduced, the reliability of systems and equipment can be increased, and the environment can be protected.

**Acknowledgement:** This work was supported by the Bulgarian Science Fund, through KP-06-COST/5 /17.05.2022 as national co-financing to the European MIC Network – New paths for science, sustainability and standards, COST Action CA20130.

#### REFERENCES

1. M. Wu, T. Wang, K. Wu, L. Kan, *Construction and Building Materials*, **239**, 117813 (2019), doi: 10.1016/j.conbuildmat.2019.117813.
2. M. E. Tuccillo, Report on condition assessment technology of wastewater collection systems. Cincinnati, Ohio: National Risk Management Research Laboratory, Office of Research and Development, U.S. Environmental Protection Agency, 2010.
3. L. Trif, A. Shaban, J. Telegdi, *Corrosion Reviews*, **36**(4), 349 (2018), doi: 10.1515/correv-2017-0032.
4. V. Scotto, R. D. Cintio, G. Marcenaro, *Corrosion Science*, **25** (3), 185 (1985), doi: 10.1016/0010-938X(85)90094-0.
5. S. C. Dexter, G. Y. Gao, *Corrosion*, **44** (10), 717 (1988), doi: 10.5006/1.3584936.
6. N. M. Noor, K. S. Lim, N. Yahaya, A. Abdullah, *Advanced Materials Research*, **311–313**, 875 (2011), doi: 10.4028/www.scientific.net/AMR.311-313.875.
7. R. M. Rasol, A. A. Bakar, N. M. Noor, N. Yahaya, M. Ismail, *Solid State Phenomena*, **227**, 294 (2015), doi: 10.4028/www.scientific.net/SSP.227.294.
8. B. J. Little, J. S. Lee, in: *Oil and Gas Pipelines*, John Wiley & Sons, Ltd, 2015, p. 387. doi: 10.1002/9781119019213.ch27.
9. R. Javaherdashti, in: *Microbiologically Influenced Corrosion: An Engineering Insight*, in *Engineering Materials and Processes*, R. Javaherdashti (ed.), Cham: Springer International Publishing, 2017, p. 29. doi: 10.1007/978-3-319-44306-5\_4.
10. S. C. Dexter, D. J. Duquette, O. W. Siebert, H. A. Videla, *Corrosion*, **47** (4), 308 (1991), doi: 10.5006/1.3585258.
11. S. N. Victoria, A. Sharma, R. Manivannan, *Journal of the Indian Chemical Society*, **98** (6), 100083 (2021), doi: 10.1016/j.jics.2021.100083.
12. M. Stern, A. L. Geary, *J. Electrochem. Soc.*, **104** (1), 56 (1957), doi: 10.1149/1.2428496.
13. A. Mohammed, A. Abdullah, Proceedings of 2018 International Conference on Hydraulics and Pneumatics – HERVEX, ISSN 1454 – 8003, 2019.
14. J. I. Goldstein et al., *Scanning Electron Microscopy and X-ray Microanalysis*, Third Edn., Boston, MA, Springer US, 2003. doi: 10.1007/978-1-4615-0215-9.
15. F. A. Stevie, C. L. Donley, *Journal of Vacuum Science & Technology A*, **38** (6), 063204 (2020), doi: 10.1116/6.0000412.
16. L. T. C. França, E. Carrilho, T. B. L. Kist, *Quarterly Reviews of Biophysics*, **35** (2), 169 (2002), doi: 10.1017/S0033583502003797.
17. E. R. Mardis, *Annual Review of Genomics and Human Genetics*, **9**, 387 (2008), doi: 10.1146/annurev.genom.9.081307.164359.
18. O. Coskun, *North Clin. Istanbul*, 2016, doi: 10.14744/nci.2016.32757.
19. L. M. Harwood, Accessed: Aug. 27, 2024. [online]. Available: <https://cir.nii.ac.jp/crid/1130282269595476992>
20. M. M. Al-Darbi, Z. M. Muntasser, M. Tango, M. R. Islam, *Energy Sources*, **24** (11), 1009 (2002), doi: 10.1080/00908310290086941.
21. S. L. Wilson, T. R. Jack, in: *Microbiologically Influenced Corrosion in the Upstream Oil and Gas Industry*, CRC Press, 2017.
22. Z. Muntasser, M. Al-Darbi, M. Tango, M. R. Islam, Proc. CORROSION 2002 Conference, OnePetro, 2002, Accessed: Jul. 21, 2024. [online]. Available: <https://dx.doi.org/>
23. B. E. L. Morris, G. M. van der Kraan, in: *Microbiologically Influenced Corrosion in the Upstream Oil and Gas Industry*, CRC Press, 2017.
24. H. A. Videla, L. K. Herrera, *International Biodeterioration & Biodegradation*, **63** (7), 896 (2009), doi: 10.1016/j.ibiod.2009.02.002.
25. N. D. Tomashov, R. M. Altovskiy, G. P. Chernova, *J. Electrochem. Soc.*, **108** (2), 113 (1961), doi: 10.1149/1.2428023.
26. Y. Okazaki, Y. Ito, K. Kyo, T. Tateishi, *Materials Science and Engineering: A*, **213** (1), 138 (1996), doi: 10.1016/0921-5093(96)10247-1.
27. C. A. C. Sequeira, D. S. P. Cardoso, L. Amaral, B. Šljukić, D. M. F. Santos, *Corrosion Reviews*, **34** (4), 187 (2016), doi: 10.1515/correv-2016-0014.
28. A. Harmon, A. Reese, K. Crippen, A. Darzins, Proc. CORROSION 2016 Conference, OnePetro, Mar. 2016, Accessed: Jul. 21, 2024. [online]. Available: <https://dx.doi.org/>
29. O.H. Tuovinen, G. Cragnolino, Proc. Conference on Corrosion Monitoring in Industrial Plants, Montreal, Canada, 1986, p. 413.

## Specific problems in the CVD growth of graphene and carbon nanotubes

P. M. Rafailov<sup>1\*</sup>, V. B. Mehandzhiev<sup>1</sup>, P. K. Sveshtarov<sup>1</sup>, B. S. Blagoev<sup>1</sup>, S. Sotirov<sup>2</sup>,  
S. Boyadjiev<sup>1</sup>, V. Tomov<sup>1</sup>, L. Yankova<sup>1</sup>, D. Spassov<sup>1</sup>, D. Z. Dimitrov<sup>1,3</sup>

<sup>1</sup>*Institute of Solid-State Physics, Bulgarian Academy of Sciences, 72, Tzarigradsko Chaussee Blvd., 1784 Sofia, Bulgaria*

<sup>2</sup>*University of Plovdiv "Paisii Hilendarski", 24, Tsar Assen Str., 4000 Plovdiv, Bulgaria*

<sup>3</sup>*Institute of Optical Materials and Technologies, Bulgarian Academy of Sciences, Acad. G. Bonchev Str, Bl.109, 1113 Sofia, Bulgaria*

Received: August 09, 2024; Revised: September 24, 2024

Graphene films were grown by chemical vapor deposition (CVD) on copper foils of varying thicknesses and on copper layers evaporated onto silicon plates. Plasma enhancement was applied during the CVD process to grow vertically aligned carbon nanotubes as well. The obtained specimens were characterized using micro-Raman spectroscopy, atomic force microscopy, and scanning electron microscopy. The relationship between the number of monolayers in the graphene films and the thickness of the copper catalyst substrate is discussed.

**Keywords:** Carbon nanotubes, Graphene, Chemical vapor deposition, Raman analysis

### INTRODUCTION

A scalable growth method with good parameter control for graphene and related 2D heterostructures is the most important factor for the technological application of the unique properties of these novel materials. Chemical vapor deposition (CVD) has the potential to satisfy these requirements and is currently the dominant growth technique for "electronic-grade" large-area graphene films [1, 2]. Essentially, the CVD of graphene relies on a planar catalytic substrate, which aids the precursor dissociation and graphitic lattice formation at the high process temperatures and can host and maintain the graphene coating in the cooling stage and at ambient conditions [3]. Copper is established as a preferred substrate material because of its ability to form transient soft bonds at its surface facilitating the adsorption of C-species and, on the other hand, the widely assumed low solubility of carbon in copper. [4].

In order to obtain high-quality monolayer graphene containing large single-crystalline grains, the graphene nucleation density in the growth stage must be kept sufficiently low. Although various surface pretreatment methods like electropolishing help decreasing the nucleation density [5], it was recently shown that the decisive factor for its uncontrollable increase during the CVD process is the amorphous/graphitic carbon trapped beyond the thermodynamic solubility in the bulk and the (sub-) surface regions of the copper foil [6] during its production, e.g. along the rolling striations.

Thus, even after a thorough surface pretreatment, failing to deactivate this deleterious carbon may lead to higher nucleation density and possibly to formation of bi- or few-layer graphene regions.

CVD is also one of the most efficient techniques for growth of carbon nanotubes (CNTs) provided suitable catalyst nanoparticles are present [7]. The precursor dissociates at the surface of the catalyst nanoparticle supplying the carbon species needed for nanotube growth. The catalyst particle may get attached either on top (top-growth mode) or stay at the bottom of the nanotube (base-growth mode) [8]. An important advantage of the CVD method is that it allows control over the nanotube morphology and can produce more or less aligned CNTs. However, scalability to large-volume production and reproducibility still remain a challenge for the nanotube CVD [9].

For additional confirmation of the role of the Cu-foil carbon content in the graphene growth process we carried out a typical CVD recipe for single-layer graphene with Cu substrates of different thickness and report the results in this communication. We also report results on plasma-enhanced CVD growth of carbon nanotubes.

### EXPERIMENTAL

Graphene and carbon nanotubes were grown by CVD in a cold-wall Plasmalab System 100 research reactor from Oxford Instruments. According to the established recipe for monolayer graphene (MLG) growth [10] the substrate was first heated to 1065 °C

\* To whom all correspondence should be sent:  
E-mail: rafailov@issp.bas.bg

in an Ar and H<sub>2</sub> flow, with flow rates of 1500 and 150 sccm, respectively, for 30 minutes of annealing. Subsequently, a flow of 10 sccm CH<sub>4</sub> combined with 50 sccm H<sub>2</sub> flow, were introduced into the reaction chamber for 30 minutes for the growth stage. At the end of the process, the sample was quenched to 300 °C at a rate of 15 °C /min in hydrogen/argon atmosphere and then cooled to room temperature in pure Ar.

Carbon nanotubes were grown from acetylene gas precursor in a mix of Ar and H<sub>2</sub> as carrier gases and NH<sub>3</sub> as additional radical source (gas purity 99.999 %) in the temperature range 800–950 °C. The substrates were semiconductor silicon wafers coated with TiN diffusion barrier and 5 nm Ni catalyst film. Capacitively coupled radio-frequency (RF) (13.56 MHz) plasma was ignited in the chamber during both the pretreatment and growth steps. The 5 nm Ni film was activated by the plasma at the growth temperature during the predeposition step and turned into catalyst nanoparticles.

The Raman spectra were measured in backscattering geometry using HORIBA Jobin Yvon Labram HR visible spectrometer equipped with a Peltier-cooled charge-coupled device (CCD) detector. The 633-nm line of a He-Ne-laser was used for excitation. The laser beam was focused on spots of different size using microscope optics.

The AFM images were obtained with a Nanosurf FlexAFM atomic force microscope, using the tapping mode. The AFM microscope is equipped with a silicon AFM probe for operation in non-contact and tapping mode TAP 190 Al-G.

## RESULTS AND DISCUSSION

### *I. Graphene*

As most of the graphene growth experiments so far have been conducted on standard 25 μm thick copper foils, it would be interesting to compare the results of the same recipe carried out on Cu substrates of different thickness. Initially, it was believed that graphene growth takes place in self-limited adsorption-driven mode [4]. However, recent reports on bilayer graphene (BLG) synthesis demonstrated that such CVD growth may not be self-limited for processes at ambient pressure [11]. Therefore, for our experiments we chose a low-pressure growth (4000 mTorr) mode in order to rule out atmospheric pressure as a factor facilitating formation of thicker-than-monolayer graphene. A standard 25 μm thick copper foil and another foil with 125 μm thickness were used as substrates and were subjected to the same pretreatment procedure including electropolishing. Additionally, graphene was also deposited on a 500 nm thick Cu layer evaporated on a standard SiO<sub>2</sub>/Si plate.

Figure 1 shows an AFM image and a height profile that are representative for the surfaces of the samples of both thicknesses after the graphene growth. Although the surfaces are relatively rough compared to the atomic thinness of the graphene, characterization usually reveals almost full graphene coverage as graphene compensates this roughness with increased formation of wrinkles and tears [12]. Furthermore, the lateral grain dimensions of the Cu surface do not limit the size of graphene domains which can easily overgrow their boundaries [13].

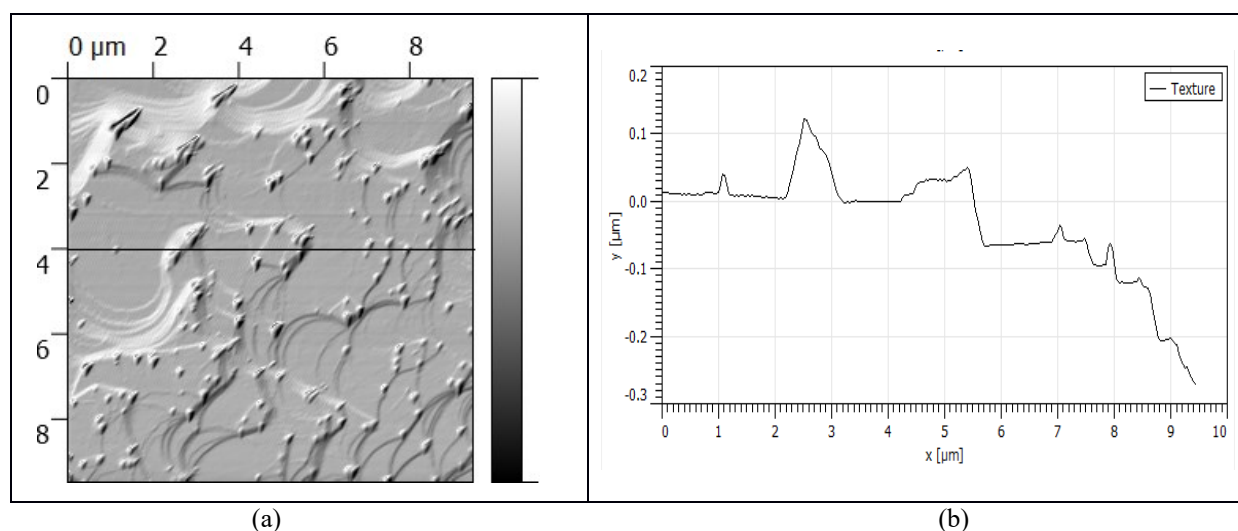


**Figure 1.** (a) AFM image of Cu foil substrate after graphene growth process. (b) Height profile recorded along the horizontal line in panel (a).

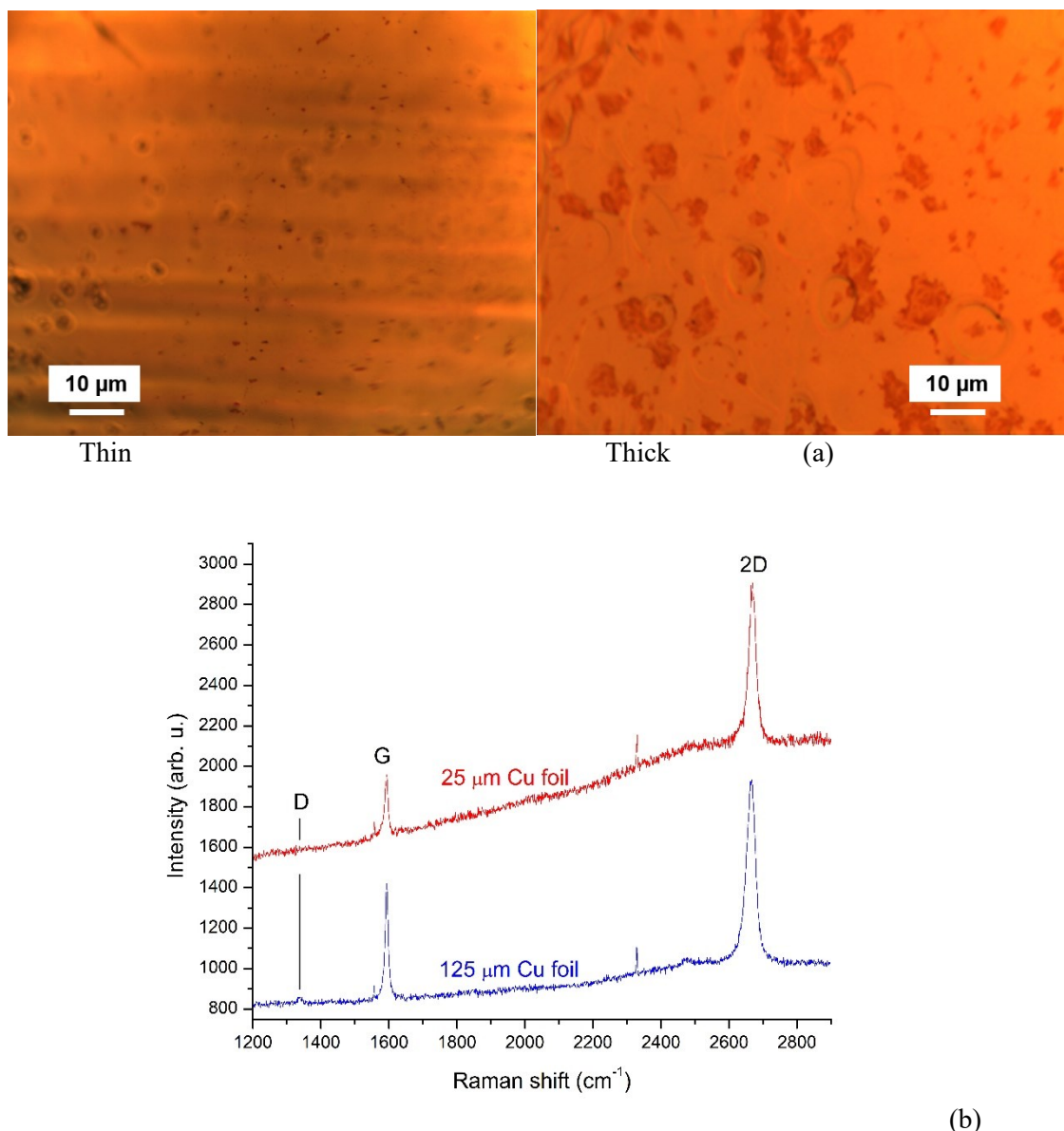


**Figure 2.** (a) Optical micrographs from the thick and thin Cu foil substrates. (b) Representative Raman spectra from these specimens.

**Table 1.** Raman spectral parameters of graphene samples.

Graphene sample on:	Band positions, $\text{cm}^{-1}$		Peak intensity ratio $I(2D)/I(G)$	2D band width, $\text{cm}^{-1}$
	G	2D		
25 $\mu\text{m}$ Cu foil	1593	2665	2.7	26
125 $\mu\text{m}$ Cu foil	1593	2667	1.5	30
500 nm Cu layer on Si	1592	2665	2.2	36
Free-standing MLG (reference)	1585	1630	3	25 - 30

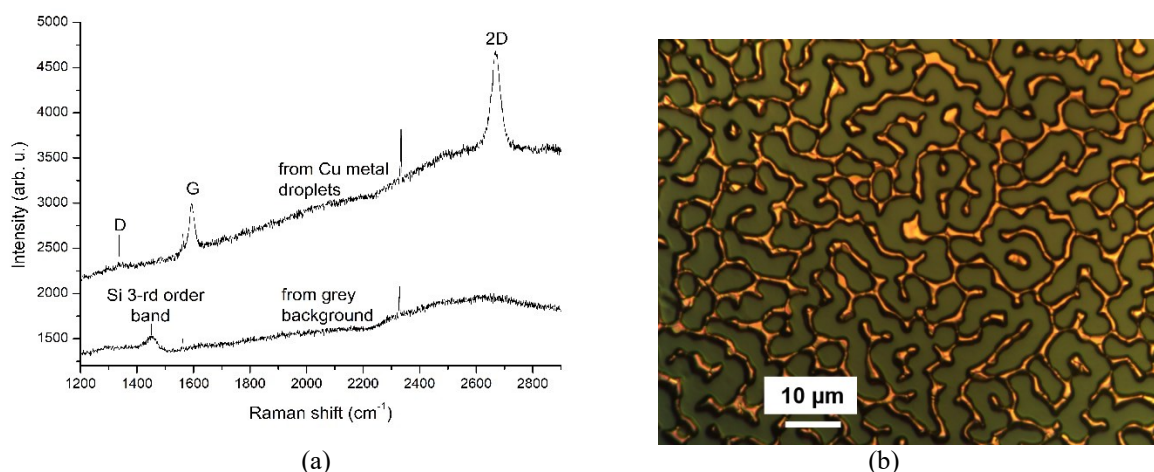
To test the deposited graphene coating, Raman spectra were recorded from several points of the CVD processed copper substrates of different thickness. A full graphene coverage of the copper substrate was established. Figure 2(a) shows microscopic images of the copper foils taken several days after the graphene deposition. The samples

exhibit mainly orange color indicating blank copper with occasional small spots of pale-red (or rosa) color indicating slight copper oxidation ( $\text{Cu}_2\text{O}$ ) which slowly develops beneath the graphene coating [10]. Figure 2(b) depicts typical Raman spectra from the nonoxidized (blank copper) areas. Some important numerical results from these Raman

spectra are summarized in Table 1 along with reference data.

As can be seen from Table 1, the Raman examination finds upshifted graphene bands with low-intensity, which is characteristic of strong graphene coupling to the Cu substrate [14]. The peak intensity ratio  $I(2D)/I(G)$  of the 2D and G bands, which is indicative of the number of monoatomic layers in a graphene film [15] is  $\approx 2.7$  for the graphene grown on the 25  $\mu\text{m}$  foil and  $\approx 1.5$  for that grown on the 125  $\mu\text{m}$  foil. Although  $I(2D)/I(G)$  may be compromised by the graphene-Cu coupling which impacts the intensity of G and 2D band in different ways, these two sharply different values undoubtedly indicate predominantly MLG on the 25  $\mu\text{m}$  foil and a significant presence of BLG on the thicker foil. On the other hand, the examined graphene coatings appear to be of good quality as can be appreciated from the faint D band intensity and the 2D bandwidth which is around  $30\text{ cm}^{-1}$  for

all spectra, i.e. it is not significantly broadened [15]. The Raman characterization thus reveals that a CVD growth recipe, which leads to MLG formation in the standard case, forms BLG on significantly thicker copper foil. Figures 3(a) and 3(b) show Raman spectra from the Cu layer on Si plate after the graphene growth process and an optical micrograph of the specimen, respectively. We conclude that during the CVD process on the thicker Cu foil there is an oversupply of carbon species from its sub-surface regions which leads to enhanced formation of bilayer graphene. This confirms the arguments raised in Ref. [6] for the importance of effectively controlling the carbon content of the Cu substrate for graphene CVD. On the other hand, the thin Cu film on  $\text{SiO}_2/\text{Si}$  coagulates into droplet-like structures which are overgrown with monolayer graphene. However, the bare  $\text{SiO}_2/\text{Si}$  surface, which emerges from this dewetting process, is not coated with graphene.



**Figure 3.** (a) Raman spectra of graphene grown on thin Cu layer evaporated on  $\text{SiO}_2/\text{Si}$ . (b) Optical micrograph from the specimen after the graphene growth process.

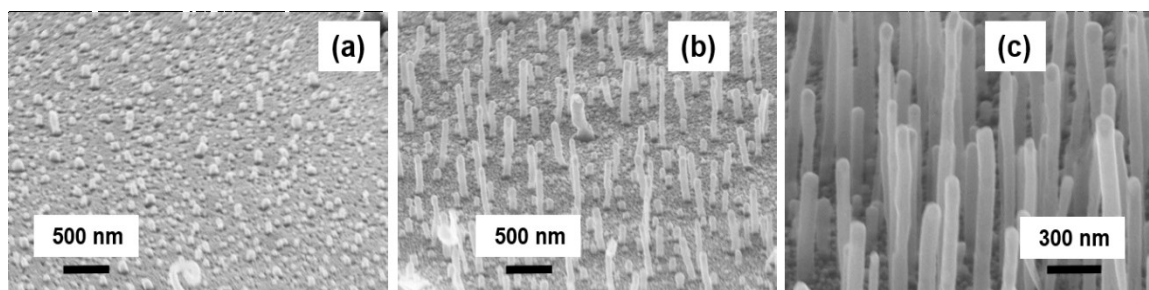


**Figure 4.** SEM micrographs from different stages of the CNT growth process. (a) activated catalyst seeds; (b) growing nanotubes with varied length; (c) straight well aligned CNT array.

## II. Carbon nanotubes

In the present experiments, a Ni/TiN/Si substrate was used. The growth of carbon nanotubes at a reasonable rate requires plasma activation of the reacting species. The thin top Ni layer is decomposed into small nanoparticles in the pre-growth step by electron bombardment in  $\text{NH}_3+\text{H}_2$  plasma, thus providing the catalyst centers for the growth start. Growth takes place *via* carbon species adsorption and trapping at atomic steps at the Ni nanoparticles' surface. It is facilitated by cyano-containing radicals from the ammonia which combine with acetylene-derived species in the plasma [16]. The presence of the intermediate TiN layer favors tip-growth mode [17, 18] which was indeed observed in the present case, the nanotube diameter being to a large extent defined by the catalytic nanoparticle. The RF electric field provides orienting force that facilitates the formation of straight nanotubes aligned perpendicular to the substrate.

Figure 4 displays SEM micrographs of the obtained CNTs in different stages of their growth. They are identified as multi-walled tubes with average diameter of  $\approx 80$  nm and length of about 1 - 2  $\mu\text{m}$ . Figure 5 shows representative Raman spectra from these objects. The spectra display the typical Raman features of multiwalled CNTs. Multiwalled nanotubes typically contain a lot of incommensurate structures and CVD grown CNTs exhibit a high content of impurities, such as graphitic compounds, amorphous carbon, unreacted metal particles etc. The intense and broadened D/G band doublet points to a considerable amount of amorphous carbon. High temperature heat treatment in an oxidizing atmosphere [19] is typically used to remove the amorphous and disordered graphitic phases.

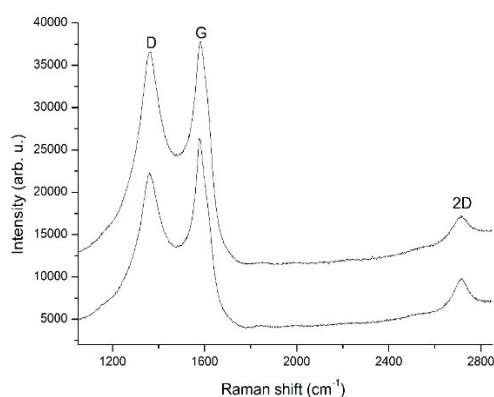


**Figure 5.** Representative Raman spectra from the obtained carbon nanotube arrays.

## CONCLUSIONS

Graphene films were grown by chemical vapor deposition (CVD) on Cu foils of different thicknesses and Cu-layer coated Si plate and characterized by micro-Raman spectroscopy, optical and atomic force microscopy. Raman characterization reveals graphene with low defect density and good homogeneity. However, on the thicker (125  $\mu\text{m}$ ) Cu foil there was an increased formation of bilayer graphene. We attribute the formation of thicker graphene to the oversupply of carbon species from the bulk and (sub-)surface regions of the thicker Cu foil during the growth process. Additionally, vertically aligned carbon nanotubes, perpendicular to the substrate, were grown by plasma-enhanced CVD and confirmed with Raman spectroscopy and scanning electron microscopy.

**Acknowledgment:** *The authors gratefully acknowledge the financial support of this work by the Bulgarian National Science Fund, Contract KII-06-H38/10. We thank Dr. Ravi Sundaram from Oxford Instruments for his help with the SEM characterization.*

## REFERENCES

1. X. Li, W. Cai, J. An, S. Kim, J. Nah, D. Yang, R. Piner, A. Velamakanni, I. Jung, E. Tutuc, S. K. Banerjee, L. Colombo, R. S. Ruoff, *Science*, **324**, 1312 (2009).
2. Z. Yan, Y. Liu, L. Ju, Z. Peng, J. Lin, G. Wang, H. Zhou, C. Xiang, E. L. G. Samuel, C. Kittrell, V. I. Artyukhov, F. Wang, B. I. Yakobson, J. M. Tour, *Angew. Chem. Int. Edn.*, **53**, 1565 (2014).
3. S. Hofmann, P. Braeuninger-Weimer, R. S. Weatherup, *J. Phys. Chem. Lett.*, **6**, 2714 (2015).
4. R. Muñoz, C. Gómez-Aleixandre, *Chemical Vapor Deposition*, **19**, 297 (2013).
5. M. Griep, E. Sandoz-Rosado, T. Tumlin, E. Wetzel, *Nano Lett.*, **16**, 1657 (2016).
6. P. Braeuninger-Weimer, B. Brennan, A. J. Pollard, S. Hofmann, *Chem. Mater.*, **28**, 8905 (2016).
7. M. Meyyappan, L. Delzeit, A. Cassell, D. Hash, *Plasma Sources Sci. Technol.*, **12**, 205 (2003).
8. M. Kumar, Y. Ando, *J. Nanosci. Nanotechnol.*, **10**, 3739-3758 (2010).
9. K. B. K. Teo, C. Singh, M. Chhowalla, W. I. Milne, Catalytic Synthesis of Carbon Nanotubes and Nanofibers, in: *Encyclopedia of Nanoscience and Nanotechnology*, volume X, H. S. Nalwa (ed.) American Scientific Publishers, 2003, p. 1.
10. P. M. Rafailov, P. K. Sveshtarov, V. B. Mehandzhiev, I. Avramova, P. Terziyska, M. Petrov, B. Katranchev, H. Naradikian, S. I. Boyadjiev, C. Cserháti, Z. Erdélyi, I. M. Szilágyi, *Molecules*, **27**, 1789 (2022).

11. P. Trinsoutrot, C. Rabot, H. Vergnes, A. Delamoreanu, A. Zenasni, B. Causat, *Surf. Coat. Technol.*, **230**, 87, (2013).
12. J.-Y. Hong, Y. C. Shin, A. Zubair, Y. Mao, T. Palacios, M. S. Dresselhaus, S. H. Kim, J. Kong, *Adv. Mater.*, **28**, 2382 (2016).
13. V. L. Nguyen, Y. H. Lee, *Small*, **11**, 3512 (2015).
14. E. Cazzanelli, O. de Luca, D. Vuono, A. Policicchio, M. Castriota, G. Desiderio, M. P. de Santo, A. Aloise, A. Fasanella, T. Rugiero, R. G. Agostino, *Journal of Raman Spectroscopy*, **49**, 1006 (2018).
15. A. C. Ferrari, J. C. Meyer, V. Scardaci, C. Casiraghi, M. Lazzeri, F. Mauri, S. Piscanec, D. Jiang, K. S. Novoselov, S. Roth, A. K. Geim, *Phys. Rev. Lett.*, **97**, 187401 (2006).
16. M. S. Bell, K. B. K. Teo, R. G. Lacerda, W. I. Milne, D. B. Hash, M. Meyyappan, *Pure Appl. Chem.*, **78**, 1117 (2006).
17. A. Gohier, T. M. Minea, M. A. Djouadi, J. Jiménez, A. Granier, *Physica E*, **37**, 34 (2007).
18. A. Gohier, C. P. Ewels, T. M. Minea, M. A. Djouadi, *Carbon*, **56**, 1331 (2008).
19. M. Endo, T. Hayashi, Y. A. Kim, H. Muramatsu, *Jpn. J. Appl. Phys.*, **45**, 4883 (2006).

## Contribution to the structural study of $\text{Rb}_3\text{Ln}(\text{PO}_4)_2$ materials (Ln=La, Ce, Pr, Nd, Sm, Eu, Gd and Tb) by vibrational spectroscopy

L. Rghioui\*, L. Benarafa, R. Khaoulaf, A. El Hajji, L. Guennoun, M. Serghini Idrissi

Laboratory of Spectroscopy, Molecular Modeling, Materials, Nanomaterials, Water and Environment, (LS3MN2E-CERNE2D), Department of Chemistry, Faculty of Sciences, Mohammed V University in Rabat, P.O.Box. 1014, Agdal-Rabat, Morocco

Received: August 17, 2024; Revised: October 08, 2024

In this work, structural studies of phosphates with general formula  $\text{Rb}_3\text{Ln}(\text{PO}_4)_2$  (Ln=La, Ce, Pr, Nd, Sm, Eu, Gd and Tb) were performed by vibrational spectroscopy. These materials were synthesized by a solid-state reaction. They crystallized in monoclinic system with space group  $\text{P}2_1/\text{m}$ . A complete vibrational study by infrared and Raman spectroscopy was carried out. These phosphates exhibited a monoclinic  $\text{P}2_1/\text{m} \rightarrow$  trigonal  $\text{P}-3\text{m}1$  phase transition which was studied by Raman spectroscopy.

**Keywords:** Infrared, spectroscopy, Raman, phase transition, monoclinic, trigonal

### INTRODUCTION

Inorganic compounds with general formula  $\text{M}_3\text{Ln}(\text{XO}_4)_2$  (M=K, Rb; Ln=rare earth element and X=P,V) have attracted much attention due to their applications as phosphors, lasers or solid state lighting materials [1-11]. For instance, Kloss *et al.* studied the luminescence phenomenon in  $\text{K}_3\text{Eu}(\text{PO}_4)_2$  and  $\text{Rb}_3\text{Eu}(\text{PO}_4)_2$ . They also studied the  $\text{Rb}_3\text{Ln}(\text{PO}_4)_2$  (Ln=La, Eu and Gd) and  $\text{K}_3\text{Eu}(\text{PO}_4)_2$  compounds by vibrational spectroscopy, but this study is incomplete [1]. The luminescence properties of Ce-activated  $\text{K}_3\text{Lu}(\text{PO}_4)_2$  were analyzed by Wisniewski *et al.* [2]. They concluded that the luminescence of this material is dominated by the d-f emission bands of  $\text{Ce}^{3+}$  and that the Ce-activated  $\text{K}_3\text{Lu}(\text{PO}_4)_2$  is a promising fast and efficient scintillator. Using high-temperature oxide-melt solution calorimetry, Ushakov *et al.* [3] have determined the formation enthalpies for  $\text{K}_3\text{Ln}(\text{PO}_4)_2$  (Ln= Sc, Y, Ce, Nd, Gd, Dy, Ho, Lu) compounds and for  $\text{A}_3\text{Lu}(\text{PO}_4)_2$  phosphates with A= Rb or Cs. Using high-temperature X-ray diffraction and differential scanning calorimetry, the authors followed the phase transition phenomenon exhibited by these compounds. Farmer *et al.* [4] have studied the structure of  $\text{K}_3\text{Lu}(\text{PO}_4)_2$  phosphate as a function of temperature by X-ray and powder neutron diffraction. Two lower-temperature phases were characterized for this compound at 230K and 130K. Crystals of  $\text{Rb}_3\text{Ln}(\text{PO}_4)_2$  (Ln= La, ..., Lu and Y) have been synthesized by Tisdale *et al.* [5]. Their structures were resolved and determined using

X-ray diffraction. The fluorescence emission spectra of  $\text{Rb}_3\text{Eu}(\text{PO}_4)_2$  and  $\text{Rb}_3\text{Tb}(\text{PO}_4)_2$  were also studied [5]. Luminescence characteristics of  $\text{K}_3\text{Lu}(\text{PO}_4)_2$  doped with  $\text{Pr}^{3+}$  were studied by Ivanovskikh *et al.* [6]. The authors showed that these compounds are promising optical materials for scintillation applications and that high concentration of  $\text{Pr}^{3+}$  ions (5%) is found to be favorable for the stabilization of the monoclinic phase. Pelczarska *et al.* [7] synthesized  $\text{Rb}_3\text{La}(\text{PO}_4)_2$  undoped and doped with  $\text{Eu}^{3+}$  ions. The characterization of these two compounds by X-ray diffraction showed that they exhibit a monoclinic structure in the  $\text{P}2_1/\text{m}$  space group by isotypy with  $\text{K}_3\text{Nd}(\text{PO}_4)_2$  phosphate [7]. The authors measured the life time of  $^5\text{D}_0$  excited state at 77K and they found it to be 4 ms. The  $4f^15d^1 \rightarrow 4f^2$  interconfigurational transitions of the  $\text{Pr}^{3+}$  ions were studied by Carrasco *et al.* [8] in  $\text{K}_3\text{Lu}_{1-x}\text{Y}_x(\text{PO}_4)_2$  doped with 1% of  $\text{Pr}^{3+}$ . The authors concluded that the substitution of Lu by Y causes a blue shift of the  $4f^15d^1 \rightarrow 4f^2$  emission.

The present work is a structural study by vibrational spectroscopy on compounds with general formula  $\text{Rb}_3\text{Ln}(\text{PO}_4)_2$  (Ln= La, Ce, Pr, Nd, Sm, Eu, Gd and Tb). It is a continuation of our investigations on phosphates, vanadates and arsenates with general formula  $\text{M}_3\text{Ln}(\text{XO}_4)_2$  and  $\text{M}_2\text{M}'\text{Ln}(\text{XO}_4)_2$  (Ln= rare earth and X= P, V, As) [12-22]. To our knowledge, no detailed vibrational studies have been carried out for  $\text{Rb}_3\text{Ln}(\text{PO}_4)_2$  (Ln= La, Ce, Pr, Nd, Sm, Eu, Gd and Tb) phosphates.

\* To whom all correspondence should be sent:  
E-mail: rghiouilotfi@gmail.com

### EXPERIMENTAL

Syntheses of  $Rb_3Ln(PO_4)_2$  samples (Ln=La,...Tb) were carried out using conventional solid-state reaction techniques. Powdered crystalline samples were prepared from a stoichiometric mixture of  $Rb_2CO_3$ ,  $Ln_2O_3$  ( $CeO_2$ ,  $Pr_6O_{11}$ ,  $Tb_4O_7$ ) and  $(NH_4)_2HPO_4$ . The mixture was ground in an agate mortar and heated at 120°C overnight, at 400°C for 24h and at 600°C for 24h to expel the decomposition products  $NH_3$ ,  $H_2O$  and  $CO_2$  respectively. A final treatment at 1000°C for 48h was realized to obtain the pure product.

The recording of the X-ray diffraction patterns was carried out using a D5000 Siemens diffractometer equipped with Bruker DIFFRAC plus EVA software, Bragg-Brentano geometry with a  $\theta$ -2 $\theta$  goniometer and a copper anode  $K_\alpha$  ( $\lambda = 1.5406\text{\AA}$ ). The angular domain in  $2\theta$  is 10-60°.

Infrared spectra were recorded using two types of spectrometers:

- A Fourier transform spectrometer type Perkin Elmer 1600. The spectral resolution is 4  $cm^{-1}$  over the whole range 4000-450  $cm^{-1}$ .

- A Fourier transform spectrometer I.F.S. 113V type Bruker (700-100  $cm^{-1}$ ). The resolution is estimated at 2  $cm^{-1}$ .

The spectra were obtained after pelleting in potassium bromide KBr (4000-450  $cm^{-1}$ ) or in polyethylene  $(C_2H_4)_n$  (700-100  $cm^{-1}$ ). The pellets in KBr were made from 1 to 2 mg of the product in 100 mg of KBr and those in  $(C_2H_4)_n$  were obtained from 2.5 mg of the product in 50 mg of polyethylene.

Raman spectra were recorded with a DILOR RT30 spectrometer equipped with two types of krypton- and argon-ionized laser Spectra-Physics 2020. Several radiations were used: 647.1 nm,

514.5 nm, 488 nm and 457.9 nm. The resolution is 1 to 2  $cm^{-1}$ . The compounds were examined in the form of powders.

### RESULTS AND DISCUSSION

#### X-ray diffraction study

The powder X-ray diffraction analysis of  $Rb_3Ln(PO_4)_2$  phosphates with Ln=La,..., Tb allowed us to conclude that these compounds crystallize in monoclinic system with space group  $P2_1/m$  by isotypy with  $K_3Nd(PO_4)_2$  phosphate. Our results are in very good agreement with those published by Tisdale *et al.* [5].

The crystal structure of  $K_3Nd(PO_4)_2$  phosphate was described by Hong and Chin [23]. The main structural units of this compound are isolated  $PO_4$  tetrahedra and  $NdO_7$  decahedra. There are two types of  $PO_4$  tetrahedra. The first, denoted P(1), shares two oxygen atoms with the same neodymium atom and shares the other two oxygen atoms with two different neodymium atoms (Figure 1). The second, denoted P(2), shares three oxygen atoms with three different neodymium atoms; the fourth oxygen atom is bound to a potassium atom (Figure 1) [23].

The unit lattice parameters of  $Rb_3Ln(PO_4)_2$  compounds were calculated and their values are given in Table 1.

Figure 2 gives the variation of the unit cell volume of  $Rb_3Ln(PO_4)_2$  compounds as a function of the radius of the rare earth ion. As it is shown in this figure, the volume of the cell regularly decreases when atomic number increases in accordance with the decrease in the ionic radii of the rare earth elements. The values of the ionic radii of the rare earth ions are taken from the Shannon tables [24] with coordination equal to 7.

**Table 1.** Unit lattice parameters of  $Rb_3Ln(PO_4)_2$  compounds

$Rb_3Ln(PO_4)_2$	La	Ce	Sm	Eu	Gd	Tb
r (Å)	1.10	1.07	1.02	1.01	1.00	0.98
(a±0.006)(Å)	9.881	9.832	9.784	9.761	9.752	9.743
(b±0.004)(Å)	5.843	5.840	5.805	5.784	5.762	5.753
(c±0.005)(Å)	7.850	7.832	7.790	7.753	7.724	7.705
(β±0.02) (°)	90.50	90.47	90.23	90.20	90.10	90.08
(V±1) (Å <sup>3</sup> )	453	450	442	438	434	432

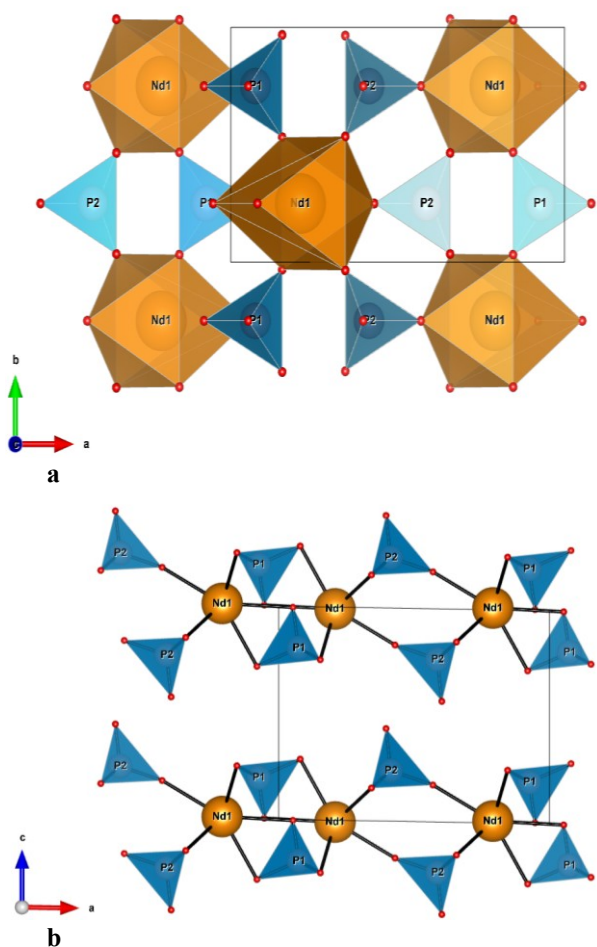


**Fig. 1.** Projection of  $K_3Nd(PO_4)_2$  structure on: a-(001) plan; b-(010) plan [23].

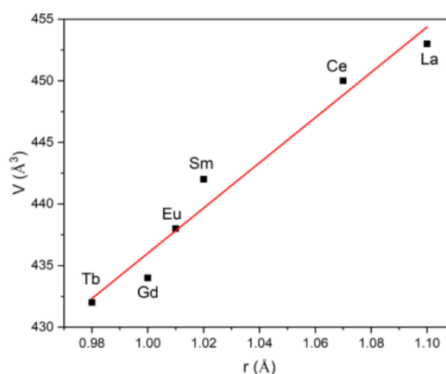


**Fig. 2.** Evolution of the unit cell volume with the radius of the rare earth ion.

### Raman and infrared studies

$Rb_3Ln(PO_4)_2$  phosphates ( $Ln = La, \dots, Tb$ ) have a monoclinic structure type  $K_3Nd(PO_4)_2$  (space group  $P2_1/m$  ( $C_{2h}^2$ ) and  $Z=2$  [23]). The  $Ln$ ,  $Rb$  and  $P$  atoms occupy  $2e$  ( $C_s$ ) sites and the oxygen atoms are distributed between the  $2e$  ( $C_s$ ) and the general  $4f$  ( $C_1$ ) positions. The structure, considered as ionic, is formed by the  $PO_4^{3-}$  groups and the  $Rb^+$  and  $Ln^{3+}$  cations. So, the separation between internal and external vibrations is possible. The factor group analysis was performed using a correlation method [25]. For the internal vibrations of each  $PO_4^{3-}$ , the correlation between molecular group  $T_d$ , site group  $C_s$  and factor group  $C_{2h}$  is given in Table 2-a. The external modes correspond to the rotational movements of  $PO_4^{3-}$  and to the translation movements of  $PO_4^{3-}$ ,  $Rb^+$  and  $Ln^{3+}$ . Table 2-b gives the correlation between site group  $C_s$  and factor group  $C_{2h}$  for these external modes.

**Table 2-a.** Correlation scheme for internal modes of  $PO_4^{3-}$  ions

Internal modes	$T_d$		$C_s$		$C_{2h}$
$\nu_1$	$A_1$	$\rightarrow$	$A'$	$\rightarrow$	$A_g + B_u$
$\nu_2$	$E$	$\rightarrow$	$A' + A''$	$\rightarrow$	$A_g + B_u + B_g + A_u$
$\nu_3$	$T_2$	$\rightarrow$	$2A' + A''$	$\rightarrow$	$2A_g + 2B_u + B_g + A_u$
$\nu_4$	$T_2$	$\rightarrow$	$2A' + A''$	$\rightarrow$	$2A_g + 2B_u + B_g + A_u$

**Table 2-b.** Correlation scheme for external modes of  $PO_4^{3-}$ ,  $Rb^+$  and  $Ln^{3+}$  ions

		$C_s$		$C_{2h}$
External modes	Rotation of $PO_4^{3-}$	$A' + 2A''$	$\rightarrow$	$A_g + B_u + 2B_g + 2A_u$
	Translation of $PO_4^{3-}$	$2A' + A''$	$\rightarrow$	$2A_g + 2B_u + B_g + A_u$
	Translation of $Rb^+$ and $Ln^{3+}$	$2A' + A''$	$\rightarrow$	$2A_g + 2B_u + B_g + A_u$

According to Table 2-a, for each type of PO<sub>4</sub><sup>3-</sup> ion, the symmetric stretching vibration  $\nu_1$  with A<sub>1</sub> symmetry in the molecular group (T<sub>d</sub>) gives one vibration in the site group (C<sub>s</sub>) with A' symmetry and two vibrations in the factor group C<sub>2h</sub> with A<sub>g</sub> and B<sub>u</sub> modes. The symmetric bending  $\nu_2$  with E symmetry in the molecular group is decomposed into two vibrations in the site group with A' and A'' modes and into four vibrations in the factor group (1A<sub>g</sub>, 1B<sub>g</sub>, 1A<sub>u</sub> and 1B<sub>u</sub>). Each vibration of T<sub>2</sub> type in the molecular group gives rise to three vibrations in the site group (2A' and 1A'') and six vibrations in the factor group (2A<sub>g</sub>, 2B<sub>u</sub>, 1B<sub>g</sub> and 1A<sub>u</sub>).

The 36 internal vibrations of the PO<sub>4</sub><sup>3-</sup> groups are subdivided in the C<sub>2h</sub> factor group as follows:

$$\Gamma_{\text{vib}}(\text{PO}_4^{3-}) = 12A_g + 6B_g + 6A_u + 12B_u.$$

The 12 rotations of PO<sub>4</sub><sup>3-</sup> groups are given by the following representation:

$$\Gamma_{\text{R}}(\text{PO}_4^{3-}) = 2A_g + 4B_g + 4A_u + 2B_u.$$

The distribution of the 33 translations of PO<sub>4</sub><sup>3-</sup>, Rb<sup>+</sup> and Ln<sup>3+</sup> is given as follows:

$$\Gamma_{\text{T}}(\text{PO}_4^{3-}, \text{Rb}^+, \text{Ln}^{3+}) = 12A_g + 6B_g + 5A_u + 10B_u \text{ with } \Gamma_{\text{ac}} = A_u + 2B_u.$$

The A<sub>g</sub> and B<sub>g</sub> modes are Raman-active while the A<sub>u</sub> and B<sub>u</sub> modes are infrared-active.

Raman and infrared spectra of the monoclinic Rb<sub>3</sub>Ln(PO<sub>4</sub>)<sub>2</sub> phosphates (Ln=La,...,Tb) are presented in Figures 3-a and 3-b, respectively. A notable similarity is observed for all infrared and Raman spectra. This confirms that these compounds are isostructural. In addition, these spectra are also very similar to those of K<sub>2</sub>RbLn(PO<sub>4</sub>)<sub>2</sub> (Ln= La,..., Dy) and K<sub>3</sub>Ln(PO<sub>4</sub>)<sub>2</sub> (Ln= La,..., Yb) phosphates which have the same symmetry (monoclinic, space group P2<sub>1</sub>/m and Z=2) [12,17]. The peak positions and their assignments are given in Tables 3 and 4.

The interpretation of the spectra can be made on the basis we used for the monoclinic K<sub>2</sub>RbLn(PO<sub>4</sub>)<sub>2</sub> (Ln= La,..., Dy) and K<sub>3</sub>Ln(PO<sub>4</sub>)<sub>2</sub> (Ln= La,..., Yb) phosphates [12,17]. Thus, we can assign the Raman peaks observed between 1081 and 960 cm<sup>-1</sup> to the PO<sub>4</sub><sup>3-</sup> asymmetric stretching vibration  $\nu_3$  with T<sub>2</sub> symmetry in molecular group T<sub>d</sub> and (A<sub>g</sub>, B<sub>g</sub>) modes in factor group C<sub>2h</sub> (Table 3-a). This vibration appears in the infrared spectra between 1100 and 965 cm<sup>-1</sup> with A<sub>u</sub> and B<sub>u</sub> symmetry species in factor group (Table 4-a).

The Raman peaks located between 928 and 960 cm<sup>-1</sup> are attributed to the PO<sub>4</sub><sup>3-</sup> symmetric stretching vibration  $\nu_1$  with A<sub>1</sub> symmetry in molecular group

vibration  $\nu_1$  with A<sub>1</sub> symmetry in molecular group T<sub>d</sub> and A<sub>g</sub> symmetry in factor group C<sub>2h</sub> (Table 3-a). The corresponding bands in the infrared spectra are observed between 928 and 955 cm<sup>-1</sup> with B<sub>u</sub> symmetry in C<sub>2h</sub> (Table 4-a) [12,17].

The asymmetric deformation modes of PO<sub>4</sub><sup>3-</sup> group  $\nu_4$  with T<sub>2</sub> symmetry in T<sub>d</sub> gave rise to six Raman peaks between 605 and 552 cm<sup>-1</sup> type A<sub>g</sub> and B<sub>g</sub> and five infrared bands between 602 and 540 cm<sup>-1</sup> type A<sub>u</sub>, B<sub>u</sub> in C<sub>2h</sub> (Tables 3-a and 4-a) [12,17].

The Raman and infrared bands observed in the range 480- 390 cm<sup>-1</sup> are attributed to the symmetric deformation vibrations  $\nu_2$  with E symmetry in T<sub>d</sub> (Tables 3-a and 4-a) [12,17].

Below 250 cm<sup>-1</sup>, we observed Raman and infrared bands attributed to external vibrations. They correspond to the libration modes of the PO<sub>4</sub><sup>3-</sup> groups and to the translation modes of the PO<sub>4</sub><sup>3-</sup>, Rb<sup>+</sup> and Ln<sup>3+</sup> ions (Tables 3-b and 4-b) [12,17]. The Raman peaks observed between 190 and 245 cm<sup>-1</sup> are assigned to the rotational modes of PO<sub>4</sub><sup>3-</sup> with A<sub>g</sub> and B<sub>g</sub> symmetry. The corresponding bands in the infrared spectra are observed between 138 and 244 cm<sup>-1</sup> with A<sub>u</sub> and B<sub>u</sub> symmetry. The translational modes of PO<sub>4</sub><sup>3-</sup> ions are located between 150 and 190 cm<sup>-1</sup> in the Raman spectra and between 100 and 130 cm<sup>-1</sup> in the infrared spectra. The bands observed in the spectra at wave numbers below 100 cm<sup>-1</sup> are attributed to the translation modes of lanthanide and Rb<sup>3+</sup> ions. The separation between these modes seems difficult.

The vibration wavenumbers of phosphates Rb<sub>3</sub>Ln(PO<sub>4</sub>)<sub>2</sub> (Ln= La,..., Tb) show an evolution by change of the rare earth element. Thus, as an example we present on Figure 4 the evolution of the  $\nu_1$  mode according to the radius of the Ln<sup>3+</sup> ion. A linear shift of this mode towards high frequencies was observed as the radius of the lanthanide decreases. This displacement can be explained by the fact that the replacement of a rare earth by another of smaller size leads to a decrease in the unit cell volume (Table 1 and Figure 2). Consequently, a strengthening of the P-O bonds took place, resulting in an increase in the frequency of vibration.

The slight difference between the slopes of the two straight lines is to be linked to the existence of two types of tetrahedra P(1)O<sub>4</sub> and P(2)O<sub>4</sub> in the crystal lattice [23].

**Table 3-a.** Raman peak positions (cm<sup>-1</sup>) and their assignments (internal modes)

La	Ce	Pr	Nd	Sm	Eu	Gd	Tb	Attribution	
								M.G.(T <sub>d</sub> )	F.G.(C <sub>2h</sub> )
1081	1081	1081	1081	1081	1081	1081	1081		A <sub>g</sub>
1038	1042	1045	1048	1052	-	1058	1058		A <sub>g</sub>
1013	1013	1013	1013	1014	1014	1015	1016	v <sub>3</sub> (T <sub>2</sub> )	A <sub>g</sub>
1002	996	994	994	991	-	-	-		B <sub>g</sub>
976	976	979	979	981	990	986	986		A <sub>g</sub>
960	960	960	962	964	969	971	971		B <sub>g</sub>
952	953	955	956	959	960	960	960	v <sub>1</sub> (A <sub>1</sub> )	A <sub>g</sub>
928	929	929	930	931	932	932	932		A <sub>g</sub>
598	600	601	601	603	603	605	605		A <sub>g</sub>
583	583	584	583	584	584	584	585		B <sub>g</sub>
573	573	573	573	573	573	575	576	v <sub>4</sub> (T <sub>2</sub> )	A <sub>g</sub>
568	568	569	568	568	569	569	570		A <sub>g</sub>
560	558	561	560	560	561	561	562		B <sub>g</sub>
554	554	554	554	553	552	552	552		A <sub>g</sub>
442	443	445	447	450	451	452	453		A <sub>g</sub>
417	417	419	418	423	421	421	422	v <sub>2</sub> (E)	B <sub>g</sub>
413	413	414	414	416	415	415	416		B <sub>g</sub>

M.G.: molecular group, F.G.: factor group

**Table 3-b.** Raman peak positions (cm<sup>-1</sup>) and their assignments (external modes)

La	Ce	Pr	Nd	Sm	Eu	Gd	Tb	Attribution in M.G.	Attribution in F.G.
216	220	224	225	234	237	240	245		B <sub>g</sub>
207	210	214	-	216	217	217	-	Rotation of PO <sub>4</sub> <sup>3-</sup>	A <sub>g</sub>
-	-	-	210	-	212	214	215		A <sub>g</sub>
190	192	194	195	200	202	204	205		B <sub>g</sub>
182	184	-	-	187	190	191	194		A <sub>g</sub>
173	173	181	180	175	178	179	179	Translation of PO <sub>4</sub> <sup>3-</sup>	B <sub>g</sub>
163	166	169	170	172	174	-	-		A <sub>g</sub>
154	155	157	156	159	159	160	157		A <sub>g</sub>
133	135	136	136	139	139	140	141		A <sub>g</sub>
116	117	116	116	117	-	-	-		A <sub>g</sub>
108	109	109	109	111	112	112	111		A <sub>g</sub>
100	101	101	101	103	104	104	104		B <sub>g</sub>
92	94	95	95	98	99	98	98		A <sub>g</sub>
85	87	87	87	90	-	89	90	Translation of Rb <sup>3+</sup> and lanthanides	B <sub>g</sub>
77	77	77	77	79	77	76	-		A <sub>g</sub>
68	69	69	69	71	72	71	71		A <sub>g</sub>
60	60	60	60	68	-	-	60		A <sub>g</sub>
50	50	50	50	50	50	-	-		A <sub>g</sub>
44	44	45	43	46	46	-	44		A <sub>g</sub>
37	37	39	36	39	39	-	38		A <sub>g</sub>

M.G.: molecular group, F.G.: factor group

**Table 4-a.** Infrared peak positions (cm<sup>-1</sup>) and their assignments (internal modes)

La	Ce	Pr	Nd	Sm	Eu	Gd	Tb	Attribution	
								M.G.(T <sub>d</sub> )	F.G.(C <sub>2h</sub> )
-	-	1085	1085	1091	1097	1100	1100		
1069	1071	1070	1069	1071	1075	1075	1075		
-	-	-	-	1052	1055	1057	1060	v <sub>3</sub> (T <sub>2</sub> )	A <sub>u</sub> , B <sub>u</sub>
1005	1004	1005	1003	996	1000	1000	998		
965	965	967	967	967	980	975	974		
947	948	952	950	953	955	955	955	v <sub>1</sub> (A <sub>1</sub> )	B <sub>u</sub>
-	-	928	930	928	928	928	928		
590	593	595	595	600	600	602	602		
-	-	-	-	-	-	-	587		
579	580	580	581	581	583	582	582	v <sub>4</sub> (T <sub>2</sub> )	A <sub>u</sub> , B <sub>u</sub>
570	570	570	570	573	573	574	573		
545	544	543	543	542	545	541	540		
457	460	466	469	470	472	472	473		
411	412	412	412	413	413	413	413	v <sub>2</sub> (E)	A <sub>u</sub> , B <sub>u</sub>
403	403	405	403	402	401	402	402		
395	395	395	395	394	394	394	395		

M.G.: molecular group, F.G.: factor group

**Table 4-b.** Infrared peak positions (cm<sup>-1</sup>) and their assignments (external modes)

La	Ce	Pr	Nd	Sm	Eu	Gd	Tb	Attribution	
-	218	220	226	234	238	240	244		
208	193	196	194	202	206	206	204	Rotation of PO <sub>4</sub> <sup>3-</sup>	
172	172	174	174	180	184	186	186	(A <sub>u</sub> , B <sub>u</sub> )	
138	138	138	136	138	139	139	138		
124	126	128	126	134	131	130	131		
112	112	114	115	130	116	120	-	Translation of PO <sub>4</sub> <sup>3-</sup>	
104	105	106	109	116	110	110	-	(A <sub>u</sub> , B <sub>u</sub> )	
91	92	92	94	109	94	96	98		
79	78	78	78	94	78	78	78	Translation of Rb <sup>3+</sup> and lanthanides	
74	74	-	74	74	78	-	-	(A <sub>u</sub> , B <sub>u</sub> )	
70	-	-	69	74	-	-	-		
64	64	64	-	68	68	-	-		
58	58	61	62	61	57	65	65		
-	-	54	54	54	54	58	54		

M.G.: molecular group, F.G.: factor group

*Study of the phase transition by Raman spectroscopy*

Tisdale *et al.* [5] followed the structural evolution of Rb<sub>3</sub>Ln(PO<sub>4</sub>)<sub>2</sub> phosphates as a function of temperature. They showed that these compounds exhibit a phase transition from the monoclinic (P2<sub>1</sub>/m) to the trigonal (P-3m1) space group. The transition temperature depends on the nature of the rare earth ion and the trigonal phase is of glaserite type [5].

For our part, we have examined the evolution of our materials symmetry with temperature using differential thermal analysis technique. The increase in temperature causes a phase transition. Table 5

gives the values of the phase transition temperatures for the compounds studied. These values are very close to that published by Tisdale *et al.* [5].

By comparison with M<sub>2</sub>CsLn(PO<sub>4</sub>)<sub>2</sub> phosphates (M = K, Rb) and Rb<sub>2</sub>KDy(VO<sub>4</sub>)<sub>2</sub> and Cs<sub>1.52</sub>K<sub>1.48</sub>Gd(VO<sub>4</sub>)<sub>2</sub> vanadates which have a glaserite structure [16, 18, 22], we can conclude that in Rb<sub>3</sub>Ln(PO<sub>4</sub>)<sub>2</sub> phosphates (at high temperature), the Rb atoms occupy two sites of symmetry, C<sub>3v</sub> and D<sub>3d</sub>, respectively, the rare earth element is logged in a site of D<sub>3d</sub> symmetry, while the phosphorus atom is located in a site of C<sub>3v</sub> symmetry.

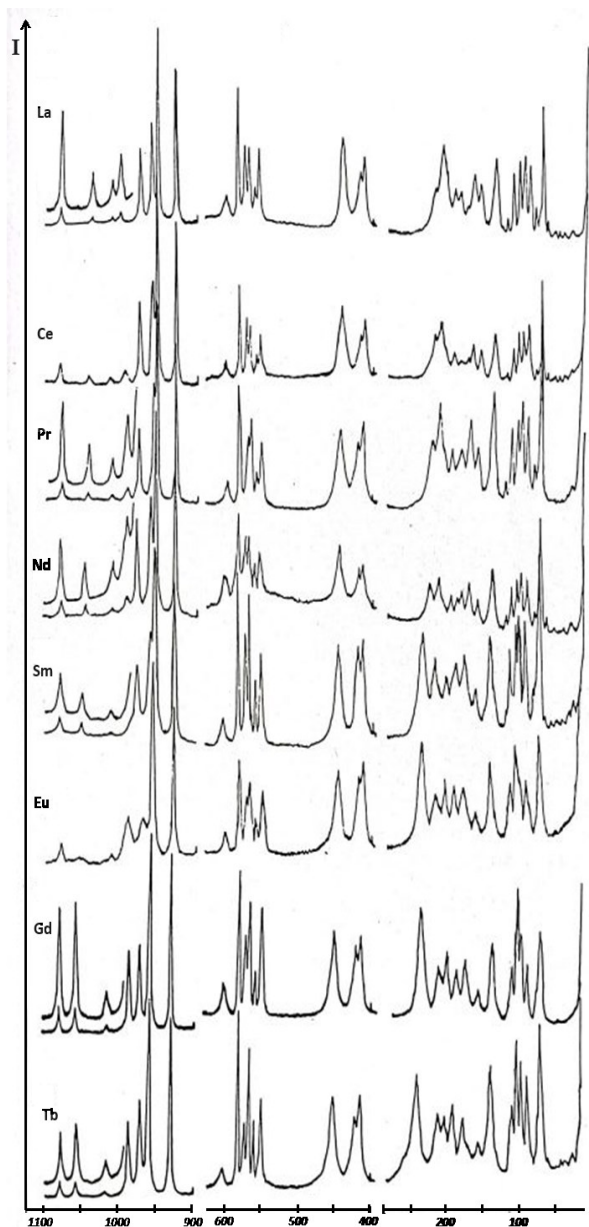


**Fig. 3-a.** Raman spectra of  $Rb_3Ln(PO_4)_2$  phosphates (Ln=La,..., Tb)

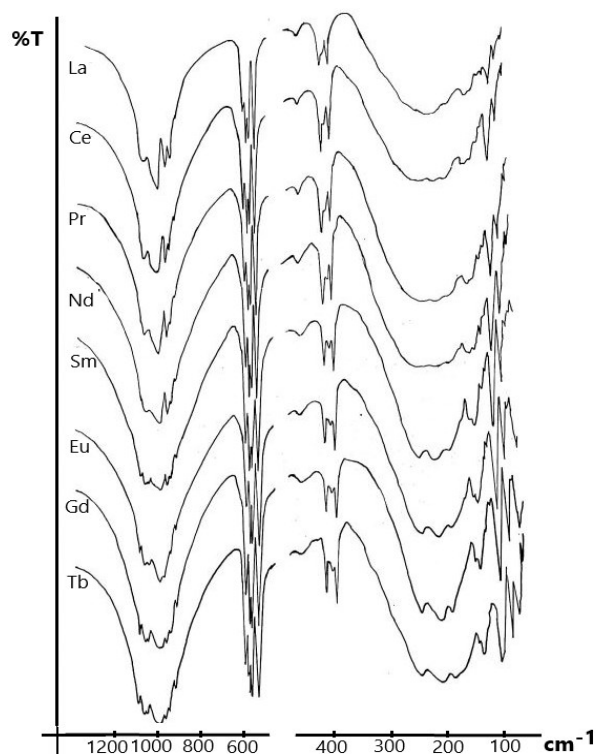


**Fig. 3-b.** Infrared spectra of  $Rb_3Ln(PO_4)_2$  phosphates (Ln=La,..., Tb)

The 18 internal vibrations of the  $PO_4^{3-}$  groups are subdivided as follows:

$$\Gamma_{\text{vib}}(PO_4^{3-}) = 3A_{1g} + 3A_{2u} + 3E_g + 3E_u$$

The 6 rotations of  $PO_4^{3-}$  groups are given by the following representation:

$$\Gamma_R(PO_4^{3-}) = A_{1u} + A_{2g} + E_g + E_u$$

The distribution of the 15 translations of  $PO_4^{3-}$ ,  $Rb^+$  and  $Ln^{3+}$  is given as follows:

$$\Gamma_T(PO_4^{3-}, Rb^+, Ln^{3+}) = 2A_{1g} + 3A_{2u} + 2E_g + 3E_u \text{ with } \Gamma_{\text{ac}} = A_{2u} + E_u$$

The  $A_{1g}$  and  $E_g$  modes are Raman-active while the  $A_{2u}$  and  $E_u$  modes are infrared-active. The  $A_{2g}$  and  $A_{1u}$  modes are inactive.

**Table 5:** Values of the temperature transition for  $Rb_3Ln(PO_4)_2$  phosphates

Ln	La	Ce	Pr	Nd	Sm	Eu	Gd	Tb
T(°C)	1080	990	940	845	680	520	380	90

## CONCLUSIONS

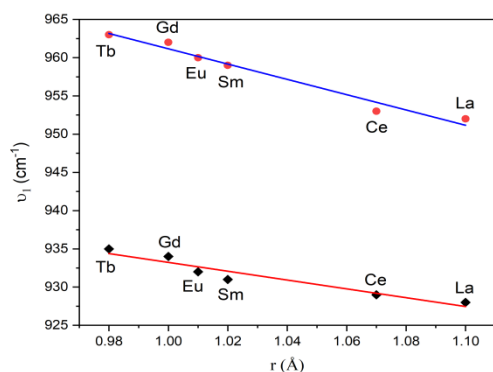


**Fig.4.** Evolution of  $\nu_1$  mode with the radius of the rare earth

The Raman spectrum of  $Rb_3Eu(PO_4)_2$  was recorded between ambient temperature and  $700^\circ C$ . Figure 5 shows the Raman spectra at ambient temperature and at  $600^\circ C$ . The change observed in the spectrum at  $600^\circ C$  indicates that the phosphate  $Rb_3Eu(PO_4)_2$  exhibits a phase transition at high temperature. In addition, the Raman spectrum at  $600^\circ C$  is very similar to those of  $K_2CsLn(PO_4)_2$  and  $Rb_2CsLn(PO_4)_2$  phosphates which have a glaserite type symmetry (trigonal, P-3m1 space group)[18]. This confirms that  $Rb_3Eu(PO_4)_2$  phosphate has a glaserite type structure at high temperature.

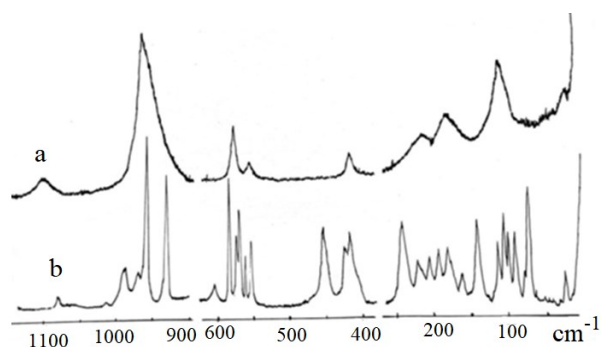


**Fig. 5.** Raman spectra of  $Rb_3Eu(PO_4)_2$  at  $600^\circ C$  (a) and at ambient temperature (b)

The spectrum recorded at  $600^\circ C$  shows two broad peaks at  $956\text{ cm}^{-1}$  attributed to the  $PO_4^{3-}$  symmetric and asymmetric stretching vibrations ( $\nu_1$  and  $\nu_3$ ) and at  $1100\text{ cm}^{-1}$  due to the  $\nu_3$  mode. Between  $600$  and  $500\text{ cm}^{-1}$ , two bands are observed and are assigned to the asymmetric deformation modes of  $PO_4^{3-}$  group ( $\nu_4$ ). The Raman peak observed at around  $400\text{ cm}^{-1}$  is attributed to the symmetric deformation mode ( $\nu_2$ ). The external vibrations give rise to four lines, three of which are very wide. The width of the bands can be explained by the thermal effect.

In this work, we carried out a study of the powder X ray diffraction and the vibrational spectra of  $Rb_3Ln(PO_4)_2$  phosphates ( $Ln = La, Ce, Pr, Nd, Sm, Eu, Gd$  and  $Tb$ ). The analysis of the spectra allowed us to conclude that these phosphates crystallize in monoclinic system with space group  $P2_1/m$  by isotypy with  $K_3Nd(PO_4)_2$  compound. The comparison between the Raman and infrared wave numbers shows that the majority of them are not coincident. This confirms that the space group of these phosphates is centrosymmetric.

The attribution of the infrared bands and the Raman lines of these systems is realized in molecular group  $T_d$  and factor group  $C_{2h}$  on the basis of the bibliographic data.

The comparative study of the vibrational spectra of these compounds shows that the substitution of a rare earth ion by another of smaller size, leads to a shift of the wave numbers to higher values. Consequently, a strengthening of the P–O bonds takes place.

The  $Rb_3Ln(PO_4)_2$  phosphates exhibit a phase transition monoclinic ( $P2_1/m$ )  $\rightarrow$  trigonal (P-3m1). This phase transition was highlighted by Raman spectroscopy. In fact, the Raman spectrum of  $Rb_3Eu(PO_4)_2$  was recorded at  $600^\circ C$ . This spectrum is very similar to the Raman spectra of  $K_2CsLn(PO_4)_2$  and  $Rb_2CsLn(PO_4)_2$  which have a trigonal structure (P-3m1 space group). The bands observed were attributed by comparison with  $K_2CsLn(PO_4)_2$  and  $Rb_2CsLn(PO_4)_2$  Raman spectra.

## REFERENCES

1. M. Kloss, L. Schwarz, J. P. K. Hölsä, *Acta Phys. Polon. A*, **95**(3), 343 (1999).
2. D. Wisniewski, A. J. Wojtowicz, W. Drozdowski, J. M. Farmer, L. A. Boatner, *J. of Alloys and Compounds*, **380**, 191 (2004).
3. S. V. Ushakov, A. Navrotsky, J. M. Farmer, L. A. Boatner, *J. of Mat. Res.*, **19**(7), 2165 (2004).
4. J. M. Farmer, L. A. Boatner, B. C. Chakoumakos, C. J. Rawn, D. Mandrus, R. Jin, J. C. Bryan, *J. of Alloys and Compounds*, **588**, 182 (2014).
5. H. B. Tisdale, M. S. Christian, G. Morrison, T. M. Besmann, K. Sun, G. S. Was, H. Loye, *Chem. Mater.*, **34**(8), 3819(2022).
6. K. V. Ivanovskikh, V. A. Pustovarov, S. Omelkov, M. Kirm, F. Piccinelli, M. Bettinelli, *J. of Lumin.*, **230**, 117749 (2021).
7. A. Pelczarska, A. Watras, P. Godlewska, E. Radomska, L. Macalik, I. Szczgiel, J. Hanuza, P. J. Deren, *New J. of Chemistry*, **39**(11), 8474 (2015).
8. I. Carrasco, K. Bartosiewicz, F. Piccinelli, M. Nikl, M. Bettinelli, *J. of Lumin.*, **189**, 113 (2017).
9. X. Han, C. Xin, S. Wang, J. Wu, Z. Ye, H. Yu, H. Zhang, *Inorg. Chem.*, **62**(24), 9679 (2023).

10. S. Ibragimov, F. Ruziev, B. Bobojonov, F. Khudoykulov, *Int. J. of Sci. and Techn. Res.*, **9(2)**, 3133 (2020).
11. S. Guo, R. Zhong, K. Gornicka, T. Klimczuk, R. J. Cava, *Chemistry of Mat.*, **32(24)**, 10607 (2020).
12. L. Rghioui, L. Benarafa, M. Saidi Idrissi, A. Lorriaux, F. Wallart, *Spectrochimica Acta Part A*, **52(4)**, 419 (1996).
13. L. Rghioui, R. Nejjar, N. El Jouhari, L. Benarafa, M. Knidiri, A. Lorriaux, F. Wallart, *Can. J. of Anal. Sci. and Spectrosc.*, **43(3)**, 90 (1998).
14. R. Nejjar, L. Rghioui, L. Benarafa, M. Saidi Idrissi, M. Knidiri, *Can. J. of Anal. Sci. and Spectrosc.*, **43(4)**, 107 (1998).
15. L. Rghioui, L. El Ammari, L. Benarafa, M. Knidiri, A. Lorriaux, F. Wallart, H. Krautscheid, *Can. J. of Anal. Sci. and Spectrosc.*, **44(3)**, 86 (1999).
16. L. Rghioui, L. El Ammari, L. Benarafa, J. P. Wignacourt, *Acta Cryst. C*, **58(7)**, i90 (2002).
17. L. Benarafa, L. Rghioui, R. Nejjar, M. Saidi Idrissi, M. Knidiri, A. Lorriaux, F. Wallart, *Spectrochimica Acta Part A*, **61(3)**, 419 (2005).
18. L. Rghioui, L. Benarafa, S. Zaydoun, A. Lorriaux, F. Wallart, *Physical and Chemical News*, **31**, 70 (2006).
19. L. Benarafa, L. Rghioui, S. Zaydoun, M. Saidi Idrissi, A. Lorriaux, F. Wallart, *Physical and Chemical News*, **46**, 111 (2009).
20. L. Rghioui, L. Benarafa, J. El Jastimi, A. El Hajji, A. Lorriaux, F. Wallart, *J. of Materials and Environmental Science*, **3(1)**, 57 (2012).
21. L. Rghioui, L. Benarafa, F. Guédira, S. Zaydoun, A. Lorriaux Rubbens, F. Wallart, *J. of Materials and Environmental Science*, **6(11)**, 3015 (2015).
22. L. Rghioui, L. El Ammari, A. Assani, M. Saadi, *Acta Cryst.*, **E75**, 1041 (2019).
23. H. Y.P. Hong, S. R. Chinn, *Mater. Res. Bull.*, **11**, 421 (1976).
24. R. D. Shannon, *Acta Cryst.*, **A32**, 751 (1976).
25. W.G. Fateley, F.R. Dolish, N. T. Mc Devit, F. T. Bentley, *Infrared and Raman Selection Rules for Molecular and Lattice Vibrations - The Correlation Method*, New York, Wiley, 1972.

# Mechanical properties, EDM process optimization, and wear performance of Al 7075-based NiCr-graphite reinforced metal matrix composites

R. Palani<sup>1\*</sup>, S. Ilaiyavel<sup>2</sup>, Mathanbabu Mariappan<sup>3</sup>

<sup>1</sup>Department of Mechanical Engineering, Vel Tech High Tech Dr. Rangarajan Dr. Sakunthala Engineering College, Chennai, Tamil Nadu, 600062, India

<sup>2</sup>Department of Mechanical Engineering, Sri Venkateswara College of Engineering, Pennalur, Sriperumbudur, Chennai-602 117, India

<sup>3</sup>Department of Mechanical Engineering, Government College of Engineering, Bargur, Krishnagiri, Tamilnadu-635104, India

Received: August 06 2024; Revised: November 05, 2024

Aluminum matrix composites are increasingly popular in the automobile and aerospace sectors due to their enhanced stiffness, low weight, and high strength. This study aims to enhance the quality of aluminum metal matrix composites by incorporating nickel, chromium, and graphite using the stir casting method. The influence of varying proportions of nickel, chromium, and graphite on the material's behavior was analyzed by altering the reinforcement composition. The mechanical properties of the composite were assessed through tensile, impact, and hardness testing. The machining characteristics in wire electrical discharge machining (WEDM) were optimized using the Taguchi method across various parameters. Wear analysis of wire-cut specimens was conducted using a pin-on-disc apparatus. Results indicated that the specimen with 4% graphite and 10% nickel-chromium exhibited superior mechanical properties and wear resistance compared to other specimens. Optimization results revealed that a material removal rate (MRR) of 0.055978 g/min and a surface roughness (SR) of 3.2  $\mu\text{m}$  were achieved with input parameters of 50 V, 6 A current, 6  $\mu\text{s}$  pulse-on time, and 14  $\mu\text{s}$  pulse-off time in WEDM, resulting in a smooth surface finish. Post-wear microstructural evaluation was conducted using scanning electron microscopy (SEM); energy dispersive spectroscopy (EDS) was employed to analyze the elemental distribution within the material. EDS analysis confirmed a uniform distribution of reinforcement materials throughout the composite.

**Keywords:** Aluminum metal matrix, optimization, wear, machining parameters, SEM, EDS

## INTRODUCTION

Composites are materials with phases that are dissimilar, with a distinct surface separating them. They exhibit extraordinary mechanical and thermal properties and find large applications in the field of material science [1]. Ceramics, metals, and polymers may be utilized as matrices for composites. Metal matrix composites are formed when a metal is used as the matrix or supporting structure. A metal matrix is made up of two phases: one that serves as a supporting framework and the other that serves as a disseminated phase [2]. Aluminum is one of the engineering materials with high strength utilized extensively for structural applications. Aluminum composites possess excellent properties compared to pure aluminum or alloys of aluminum [3]. The making of metal matrix composites (MMC) can be done using many methods like powder metallurgy, stir casting under friction, hot forging, stir casting and squeeze casting [4]. Stir casting is a commonly utilized method for fabrication of metal matrix composites [5]. Nickel,

chromium and graphite showcase good tribological properties, so they are used mostly for reinforcing with metal matrix in which there is chance of wear [6]. The graphite in the MMC acts as a self-lubricating medium which in turn lowers the rate of wear [7]. Metal matrix composites embedded with ideal material in it are unique and have tremendous opportunity in design of special components in the automotive field [8].

Research is going on in the field of material engineering to produce materials with good qualities. A lot of researchers have contributed to material science by using aluminum as the metal matrix for their reinforced composites using various materials for reinforcement. Madeva Nagaral *et al.* [9] used stir casting to create an Al7475 metal matrix supplemented with 5% wt. of nano  $\text{Al}_2\text{O}_3$ . According to ASTM standards, it was tested for hardness, ultimate yield strength, and elongation. The wear analysis was done using a pin-on-disc device experiment with stable speed and variable weights. Bharath *et al.* [10] used the unique notion of two-step reinforcements in the stir casting method

\* To whom all correspondence should be sent:  
E-mail: [rpalani456@gmail.com](mailto:rpalani456@gmail.com),  
[palani@velhightech.com](mailto:palani@velhightech.com)

to manufacture  $Al_2O_{14}$  with  $Al_2O_3$  ceramic. SEM and microstructure analyses indicated that the  $Al_2O_3$  distribution was quite uniform. The wear rate identified by particle refinement was determined using XRD spectroscopy. Experimentation reveals that the optimal mixer combinations resulted in a hardness of 68.54 percent (15 wt. percent) and a tensile strength of 29.03 percent (15 wt. percent). Greater wear resistance qualities were obtained from the composites, and worn surfaces were investigated by SEM analysis.

Han *et al.* [11] indicated that the machining of MMC is difficult due to the difference in properties between the metal matrix and reinforced materials. An experimental investigation was done to evaluate the impact of process factors responsible for machining metal matrix on the final surface finish. The results indicated that selecting optimized parameters is paramount for producing a finished and smooth surface. Palaniswamy *et al.* [12] experimentally studied and optimized aluminum MMC. The machine factors, like discharge current and pulse timing, were optimized to improve the metal removal rate and reduce the rate of tool wear. The findings of the study show that the discharge current is an important parameter in governing the surface finish produced.

In the current work, Al7075 is employed as the base material which is stir-cast with Ni-Cr and graphite. The addition of Ni-Cr improves the properties of the MMC, which directly influences its ability to withstand abrasive forces and reduces the wear rate. Graphite, known for its solid lubricating properties, helps in decreasing the coefficient of friction, thereby reducing wear and improving the machinability of the composite. The improved hardness by Ni-Cr and the lubrication by graphite systematically contribute to the superior wear resistance and durability of the composite. The combination of materials utilized for MMC is not used so far in the literature for making MMC out of aluminum. The distinguishing feature of the present study is optimization of EDM-machining characteristics of the novel MMC with wear and mechanical characteristics.

## EXPERIMENTAL

The fabrication and characterization are done in five phases: fabrication, mechanical testing, EDM machining optimization and wear test followed by morphological analysis. The basic material is an Al7075 polished rod shown in Figure 1. The needed amount of Al7075 is cut from the raw material, cleaned, and accurately weighed before casting. Ni-Cr and graphite are taken in the form of powder. The

fabrication of aluminum metal matrix reinforced with Ni-Cr and graphite follows the steps: mold preparation, raw materials melting using the stir casting method followed by pouring into the mold cavity and finally machining the cast aluminum metal matrix for testing. The different composition percentage fractions of Al7075 reinforced with Ni-Cr and graphite utilized to make three specimens are given in Table 1.

**Table 1.** Al7075, Ni-Cr and graphite proportions

Specimen	Al7075 %	Ni-Cr %	Graphite %
1 (A)	93	5	2
2 (B)	86	10	4
3 (C)	79	15	6

### Mold preparation

A wooden pattern is made depending on the required specimen dimensions. The area between the pattern and the mold box is filled with sand, finer sand inside (facing sand) and coarser sand outside (backing sand). The pattern is carefully removed so that no harm is done to the mold cavity (Figure 1).



**Figure 1.** Aluminum base material and mold

### Stir casting

The main process involved in MMC fabrication is stir casting, which is the most commonly used method due to its simplicity and viability [13]. The stir casting device, shown in Figure 3, was utilised for melting the ingredients. It is constructed from a conical graphite crucible that can hold on heat up to 680°C. The crucible is put in the alumina ceramic muffle. The heating element Kanthol-A1 is wrapped around the muffle. This furnace uses resistance heating. To avoid oxidation, the stirring operation is done in an enclosed steel chamber filled with nitrogen and inert gas. The current temperature of the liquid is measured using a K-type thermocouple with a working temperature of -200°C to 1250°C. EN24 is a stirrer shaft material that is resistant to corrosion. One end of the shaft is connected to a 0.5 hp PMDC motor through a flange connection. Four blades are fused at the opposite end of the shaft at 45°C. To minimise particle coagulation and segregation when employing a hopper, a consistent feeding rate of reinforcement particles is essential.

The polished Al7075 rod is heated in the furnace. The molten matrix is swirled gently at 30 rpm, then the rate raised to 300-600 rpm using a speed controller. A combination of Ni-Cr and graphite is integrated into the MMC at a semisolid level at 640°C for a scattering duration of 5 min. The mixture is then warmed above the melting point temperature before being poured into the mold. The composite slurry in molten state is then poured into the rectangular sand mold.

Then, the Al7075 composite material which is rectangular in shape, is prepared as shown in Figure 2. The composite material is separated and cut into pieces by a milling machine after it has cooled and taken out from the mold, as shown in Figure 2 (c).

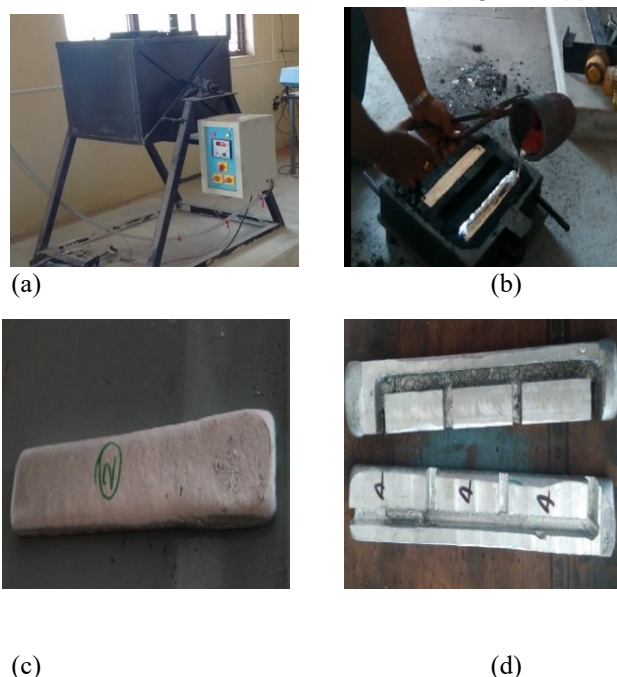


**Figure 2.** (a) Stir casting apparatus, (b) Pouring process, (c) Al 7075 composite test bar and (d) Al 7075 composite material after milling.

### Mechanical testing

Rockwell hardness tester was utilized for testing the hardness of the obtained metal matrix composite. An indenter with a ball of 2.5 mm diameter at a pressure of 500 N pressure is used for hardness testing [14]. ASTM B-557 is followed for carrying out a tensile test [15]. Charpy impact test is used to study the load absorption capability of the MMC. ASTM E23 is followed for carrying out an impact test [16].

### Wire cut electrical discharge machine (WEDM)

The wire cut EDM machine of CNC is utilized for machining the specimens. The model's name of the machine is YCM W350. The machining is done by a thin electric wire in which the tool acts as an

electrode and a dielectric fluid is passed between the tool and work piece, which carries away the vaporized or moisturized debris coming from the machining [17]. The wire cut EDM process was carried out on three specimens of various proportions. The specimens of the novel metal matrix composite (MMC) used for WEDM are shown in Figure 3.

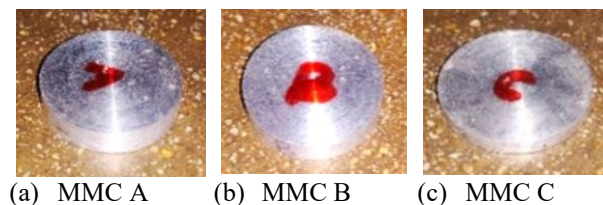


**Figure 3.** (a-c) Metal matrix composites used for EDM.

### Optimization of WEDM by the Taguchi method

Taguchi method is an optimization technique which helps in identifying the impact of the parameters involved in the experiment on the mean and variance of a particular process output. This type of optimization will reduce the experimentation work and the cost involved. The performance of the system is analyzed using signal-to-noise ratio (S/N) which is defined as the ratio between the desired value to the undesired value [18]. The input parameters of the wire cut electrical discharge machine, such as current, pulse-on time, voltage, pulse-off time were optimized to get the output parameters material removal rate (MRR) and surface roughness (SR). Taguchi method is utilized in expert design optimization [19, 20]. For obtaining the optimized parameters, the levels of process parameters involved in WEDM are initially set. The set levels of process parameters [21] are presented in Table 2.

**Table 2.** EDM process parameters

Parameters	1	2	3
Peak current	7	11	13
Servo voltage	54	51	51
Pulse-on time	3	2	5
Pulse-off time	21	20	16

### Wear testing

Wear testing is done on the specimens machined using wire cut EDM. The pin-on-disc method ASTM designation G99 procedure is used as a standard procedure to acquire the wear results from specimens [22]. The pin-on-disc apparatus used has a load carrying capacity up to 60 N, rotational speed 500 N, frictional force up to 20 N and compound wear up to 1200  $\mu\text{m}$ .

**Table 3.** Input parameters for optimization

Exp. No.	Current (A)	Voltage (V)	Pulse-on time (μs)	Pulse-off time (μs)
1	8	55	2	20
2	8	53	3	19
3	8	52	4	17
4	10	55	3	17
5	10	53	4	20
6	10	52	2	19
7	12	55	4	19
8	12	53	2	17
9	12	52	3	20

The typical pin specimen is cylindrical in shape. The diameter and the thickness of the disc specimen range from 30 to 100 mm and 2 to 10 mm, respectively. Before testing, the specimen is cleaned and dried with non-chlorinated, non-film-forming cleaning chemicals and solvents. Drying removes the residues of fluids entrapped in the material during cleaning. Steel (ferromagnetic) specimens that have residual magnetism are also demagnetized. The weight of the specimens measured is appropriately around 0.0001 g. To maintain the proper contact conditions, the pin-shaped specimen is carefully placed in its holder and adjusted so that it is perpendicular (61° degree) to the disc surface when in contact. A mass of 2 kg is added to the system lever to force the pin against the disc. The motor is started and set to a speed of 300 rpm while keeping the pin specimen away from the disc. The specimen is weighed before the testing using a weighing scale. Then it is brought in contact with the disc under load. After 10 min, the test is terminated. Tests should not be paused or resumed. The specimen is removed and cleaned, and the surface is examined for protrusions, displaced metal, discoloration, micro cracking, and spots. To acquire statistically significant findings, the specimen is measured again and the test is repeated with multiple specimens. The pin-on-disc experiment parameters are tabulated in Table 4.

**Table 4.** Pin-on-disc apparatus parameters

Parameters	Value	Unit
Force	2	kg
Speed	300	rpm
Duration	10	min

*Morphology*

Surface morphology of the specimens which have been subject to wear, were studied using SEM and EDS. SEM helps in identifying the surface defects encountered after the specimen have been subject to wear. EDS is utilized for identifying the

presence of reinforcement added to the aluminum metal. The amount of reinforcement present in the final material can be easily identified by XRD patterns observed during EDS analysis [23].

**RESULTS AND DISCUSSION**

*Mechanical characteristics*

Hardness is the property which helps the MMC in withstanding the surface wear and tear. As the hardness of the MMC increases, the property of the MMC to withstand wear also increases. The presence of chromium and nickel along with graphite have improved the hardness of the composite. Especially nickel provides an additional hardening effect [24].

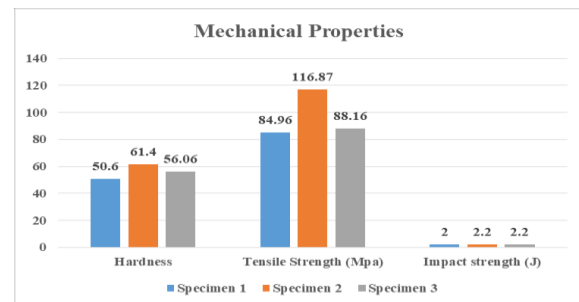


**Figure 4.** Mechanical strength of MMC

Specimen 2 shows the highest hardness among all specimens. The results of tensile and impact test also show that the performance of specimen 3 is best with 116.16 MPa of tensile strength and 2.2 J of impact strength. The improved tensile strength is due to the presence of graphite [25].

*Machining characters*

- *Rate of material removal and surface finish*

The rate of material removal is directly proportional to the weight difference between initial specimen before machining (WBM) and final specimen after machining (WAM), and inversely proportional to the machining time (MT).

$$\text{Material removal rate} = \text{WBM} - \text{WAM} / \text{MT}$$

Surface roughness (SR) indicates the texture. Surface roughness can cause irregular surface which will be easily corroded. If the surface layer is substantial, the surface will become rough; if the surface variations are minor, the surface will be smooth. Surface roughness is measured with a profile gauge. The minimal surface roughness value is for specimen 3 - 3.2 μm. The greatest surface roughness value is for specimen 2 - 6.6 μm, as shown in Table 5. Table 5 shows that 4 of the 9 specimens had higher surface roughness values calibrated using a surface profile gauge.

**Table 5.** Material removal rate (MRR) and surface roughness (SR)

Exp. No.	WBM (g)	WAM (g)	MT (min)	MRR (g/min)	SR (μm)
1	17.2955	17.0336	5.25	0.049885	3.4
2	17.6479	17.3934	5.66	0.044964	6.6
3	19.1614	18.8606	5.33	0.055978	3.2
4	17.6483	17.3766	5.08	0.053484	6.2
5	17.2082	16.9372	5.03	0.053876	3.8
6	18.0875	17.7942	5.16	0.056841	5.6
7	17.2947	17.0086	4.93	0.058032	3.9
8	18.5701	18.2610	5.65	0.054707	6.5
9	17.4121	17.1202	4.65	0.062774	5.0

**Table 6.** Input parameters and output parameters

Exp. No.	Input parameters				Output parameters	
	Machining parameters (WEDM)				MRR(g/min)	SR(μm)
	Current (A)	Voltage (V)	Pulse -on Time (μs)	Pulse -off Time (μs)		
1	8	55	2	20	0.049885	3.4
2	8	53	3	19	0.044964	6.6
3	8	52	4	17	0.055978	3.2
4	10	55	3	17	0.053484	6.2
5	10	53	4	20	0.053876	3.8
6	10	52	2	19	0.056841	5.6
7	12	55	4	19	0.058032	3.9
8	12	53	2	17	0.054707	6.5
9	12	52	3	20	0.062774	5.0

**Table 7.** Output response for MRR and SR

Response for MRR				
Level	Current	Voltage	Pulse-on Time	Pulse-off Time
1	0.04985	0.05789	0.05247	0.05244
2	0.05372	0.05102	0.05289	0.05216
3	0.05960	0.05270	0.05465	0.05681
Delta	0.00790	0.00650	0.00225	0.00215
Rank	1	2	3	4
Response for SR				
Level	Current	Voltage	Pulse-on Time	Pulse-off Time
1	4.326	4.394	4.992	5.112
2	5.231	4.987	5.223	4.936
3	5.102	4.365	3.564	4.326
Delta	0.675	1.32	2.356	1.289
Rank	4	3	1	2

**Table 8.** Signal-to-noise ratio

Exp. No.	MRR		SR	
	S/N Ratio	Mean	S/N Ratio	Mean
1	-25.0982	0.045691	10.6296	3.4
2	-26.9427	0.044964	16.3909	6.6
3	-24.9690	0.056435	10.3703	3.3
4	-25.4355	0.053484	15.8478	6.2
5	-25.3721	0.053876	11.5957	3.8
6	-24.9068	0.056841	14.9638	5.6
7	-24.7266	0.058032	11.8213	3.9
8	-25.2391	0.054707	16.2583	6.5
9	-24.0444	0.062774	13.9794	5.0

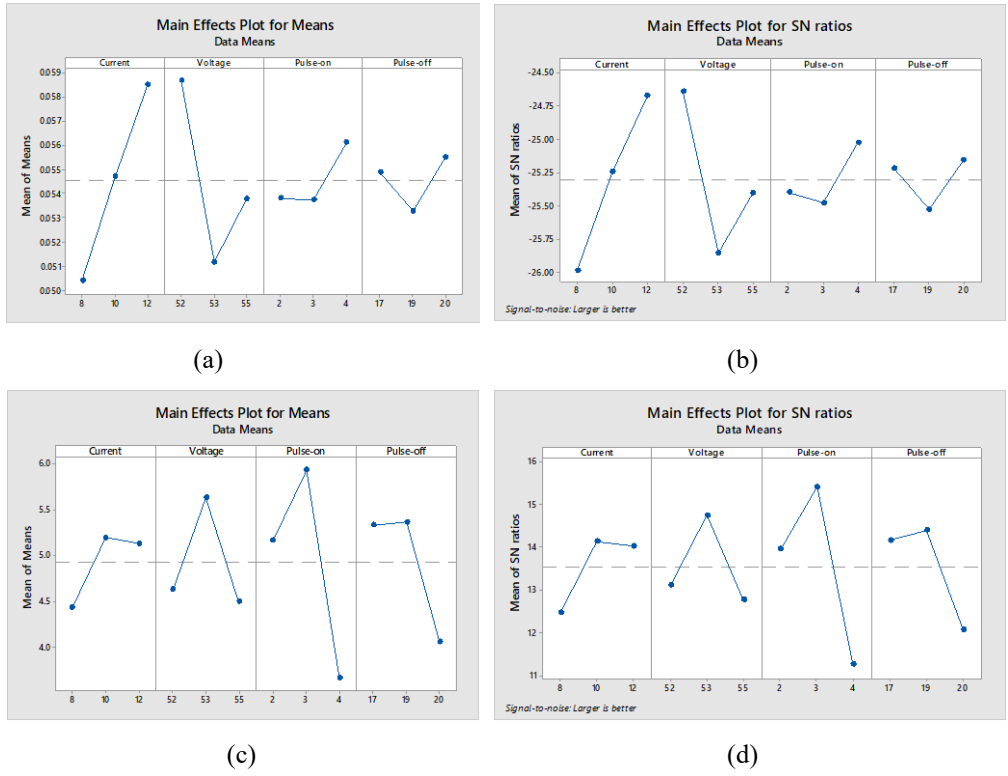


Figure 5. (a-d) Mean effect plots

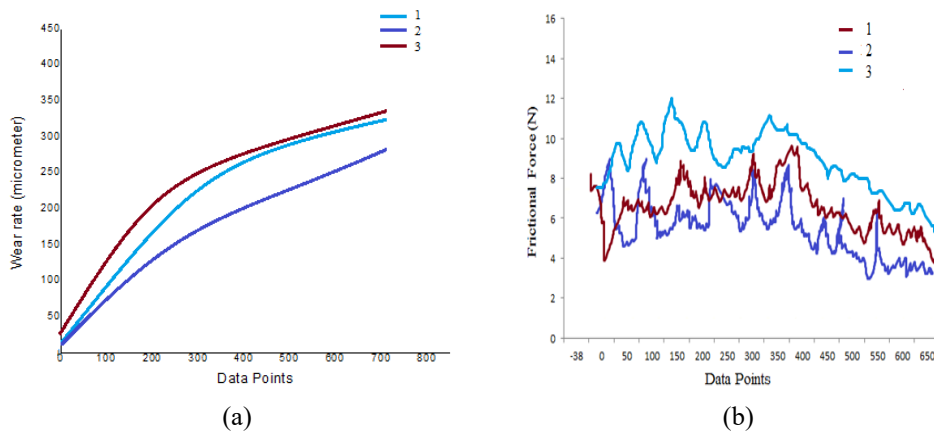


Figure 6. (a and b) Wear in  $\mu\text{m}$  and friction force in N, for MMC of various proportions

*Analysis of MRR and SR*

Surge in pulse-on time leads to a surge in discharge energy, resulting in stronger explosions and higher MRR [26]. Increased cutting speed leads to greater surface roughness [27]. Surge in pulse-on duration and peak current result in more electrons hitting the work surface, causing greater material erosion per discharge. Table 6 shows the input parameters and output parameters.

Table 7 shows the mean responses for material removed and surface roughness based on input parameters of WEDM. From the results obtained it is clear that the discharge current has an important impact on the finish of the surface obtained and the

rate of material removal of the specimen.

The plot of means is shown in Figure 10. The mean of effect plots help in identifying the impact of a particular process parameter on the output response (MRR and SR) [28]. From the graph it is clear that both current and voltage impact the MRR. Pulse-on time and pulse-off time impact the surface finish. The lower the S/N ratio, the parameters are most suited. From the table it is clear that the parameters used in the third experiment show the lowest S/N ratio, which shows that the third set of parameters is the optimal one.

*Wear analysis*

The weight loss due to wear of Al7075/Ni-

Cr/graphite composite is calculated by using the difference in weight loss before experiment to weight loss after experiment. Weights of the pieces range from 10.49 to 11.11 g. The resistance to wear of the composite altered when the percentages of reinforcements were adjusted. Figure 6 (a) depicts the findings of wear rate in  $\mu\text{m}$ . The specimen 3 with 6 % graphite and 15 % nickel-chromium content, has the worst wear resistance. When the graphite proportion steps, the specimen becomes more ductile and the composite's resistance to wear decreases. This is because addition of graphite leads to an increase in the Van der Waals forces between the particles, which will weaken the surface [29].

Test specimen 2 contains 4 % graphite and 10 % nickel-chromium and has a higher wear resistance. The nickel-chromium combination reduces the dislocation which increases the wear resistance. As the nickel-chromium content increases, the material's hardness improves, resulting in improved wear resistance [30]. The addition of graphite in a low amount will help self-lubricating the material and thereby improving the wear characteristics [31].

The friction force observed for the specimens is shown in Figure 6 (b). The higher friction force will simultaneously lead to a higher wear rate. For specimen 2, the friction factor is very low in comparison to the other specimens. The lower friction of specimen 2 is due to the strong bonding at the interface of the material while in specimen 3, the friction force is in an upward trend due to the weak inter-bonding at the interface of the material. This consequently leads to a higher frictional force and an increased wear rate.

Figure 7 depicts the wear rate for specimens of different proportions. The graph depicts the weight reduction (g) after the specimens have been subjected to wear test.

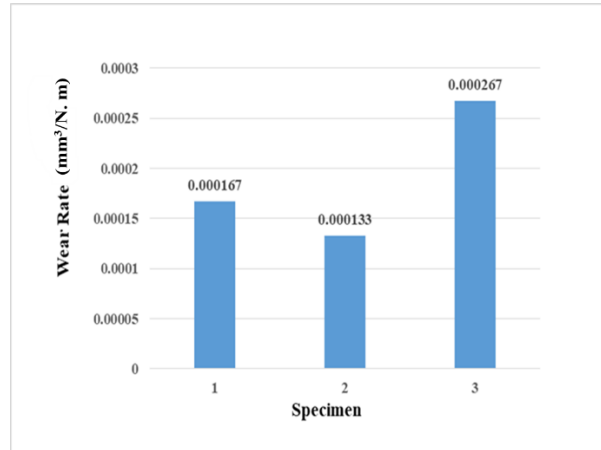
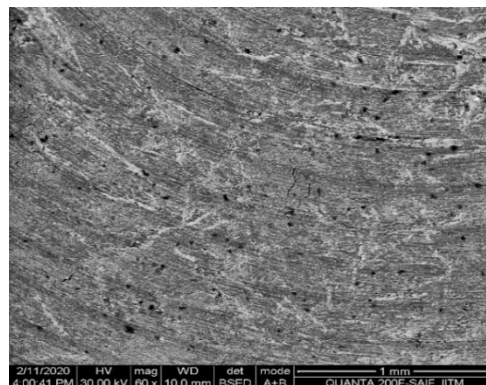


Figure 7. Wear test data comparison

#### Scanning electron microscopy (SEM) analysis

Figures 8-10 show the surface morphology image of the test specimens at different magnifications. It was revealed from the specimen SEM images, as shown in Figure 8 for specimen 1, that some parts of the specimen had crack development, which leads to a brittle fracture. The worn-out area of the surface indicates that its microstructure had fracture propagation. Lumps are also seen, which may be due to the clustering during reinforcement [32, 33].

The test specimen 2 was examined by scanning electron microscopy at magnifications of 10, 20, 50, and 100 m, as shown in Figure 9, and it was discovered that some parts of the specimen had a portion of fused particles, patches, grooves, and crack formation in a smaller amount. This is due to the less brittle structure due to the presence of 10 % Ni-Cr and the addition of 4 % graphite in the mixture. These factors resulted in a less wear character.



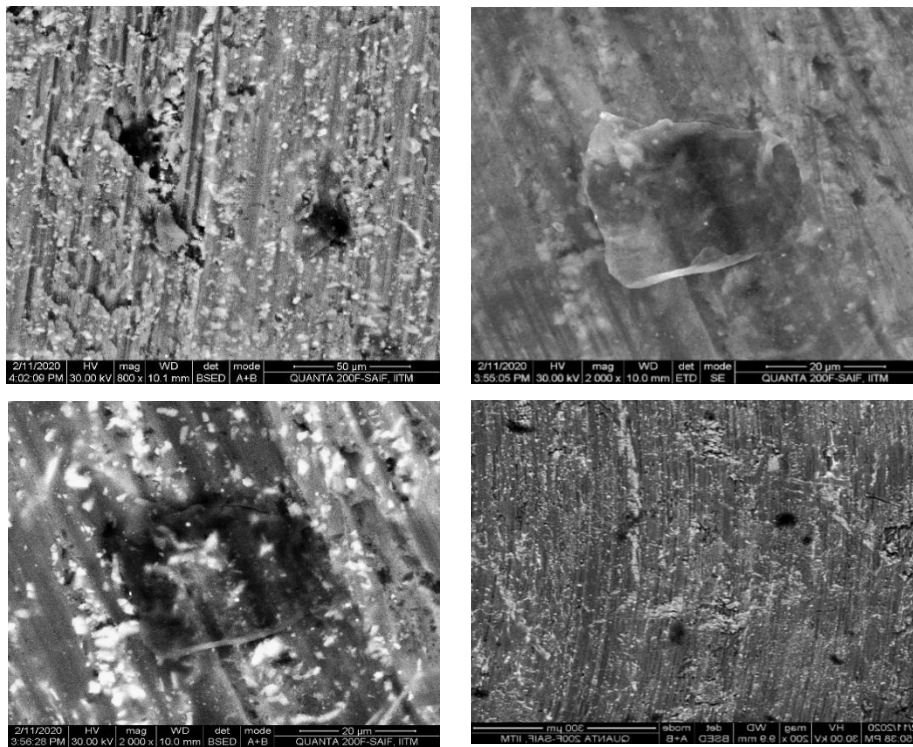


Figure 8. Specimen “1” SEM image analysis at various magnifications

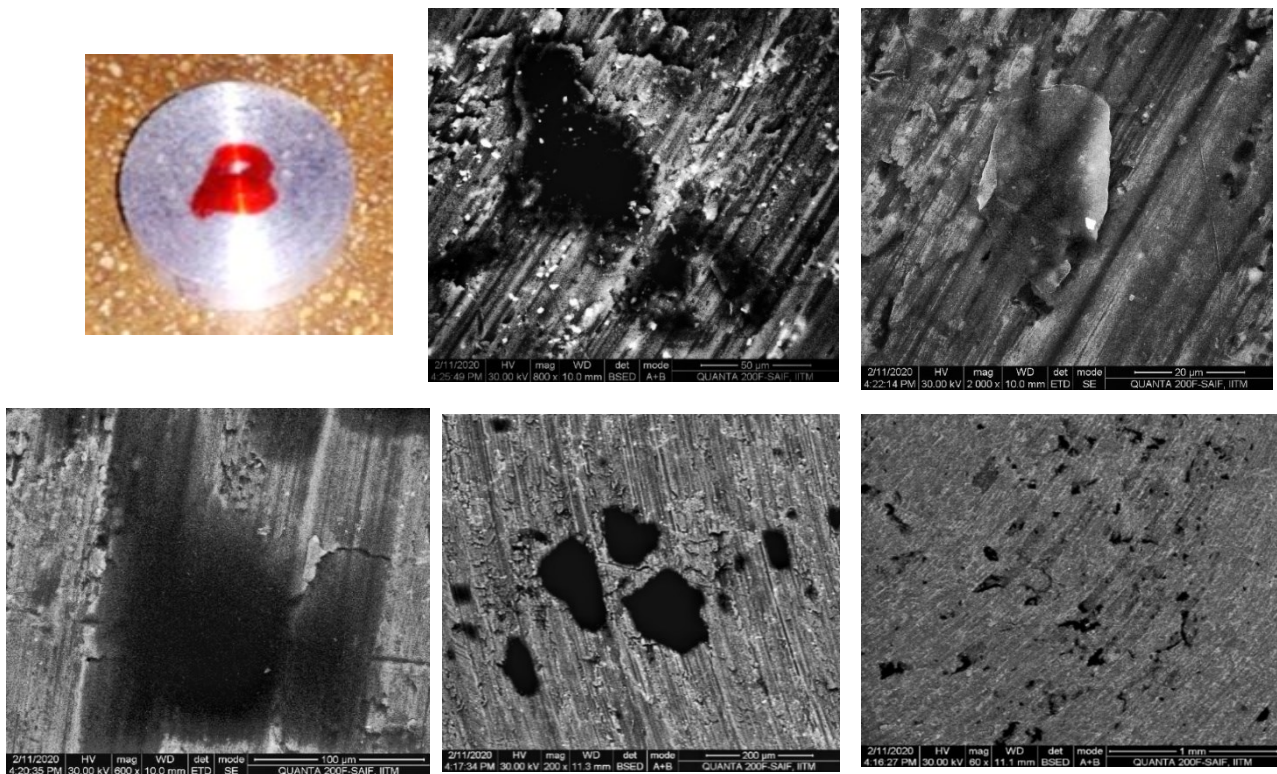


Figure 9. Specimen “2” SEM image analysis at various magnifications

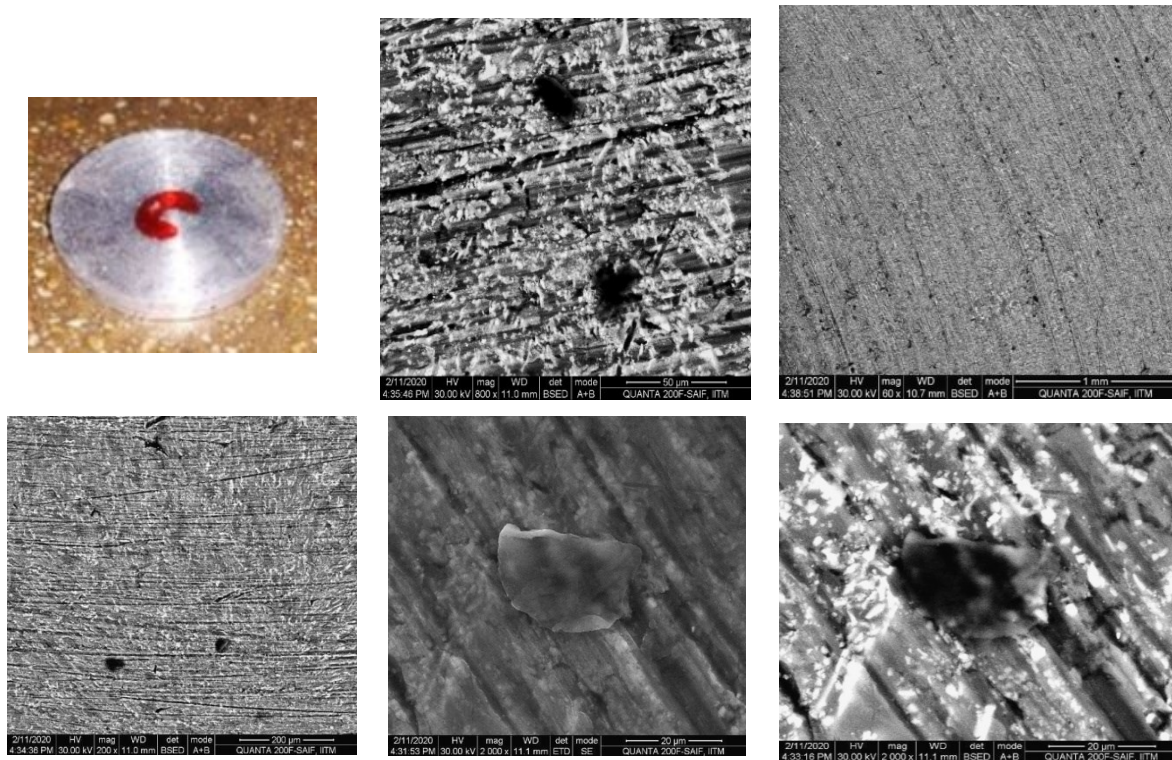
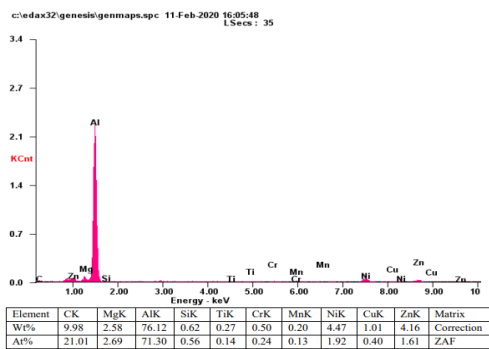
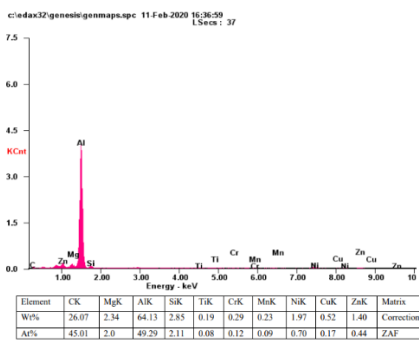


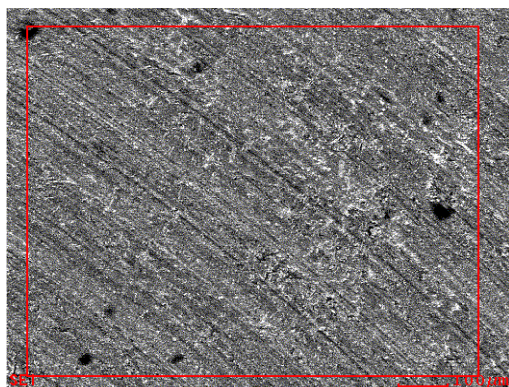
Figure 10. Specimen “3” SEM image analysis at various magnifications



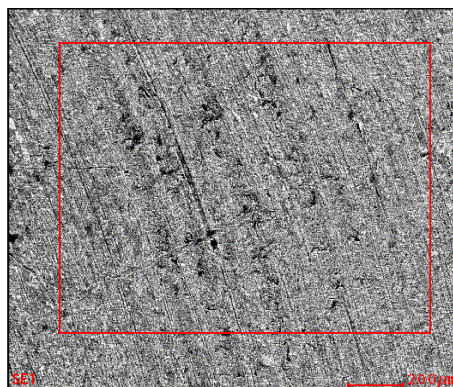
(a) EDS spectrum of specimen 1



(b) EDS spectrum of specimen 2



(c) EDS image of specimen 1



(d) EDS image of specimen 2

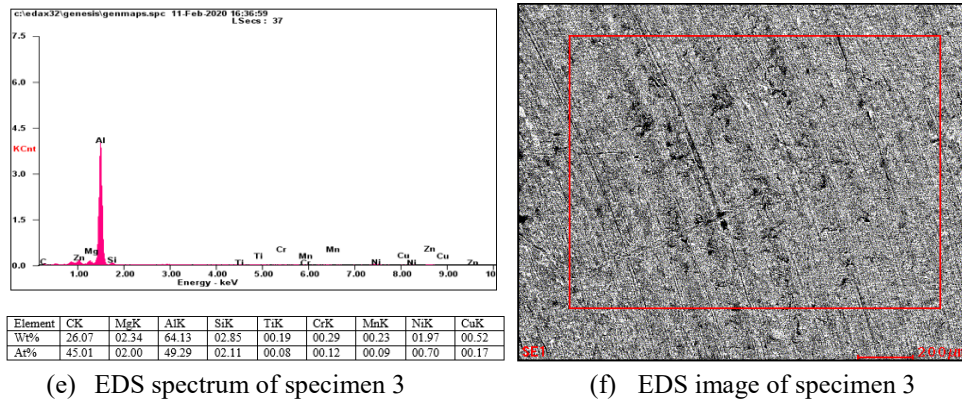


Figure 11. (a-f): EDS spectra and images obtained for MMC of various proportions

### EDS analysis

The graphs showing the dispersion of energy through-out are presented in Figure 11. The concentration of all reinforced materials is presented in the EDS spectra. The presence of nickel, chromium and graphite peaks is clearly visible in the EDS spectra. From the quantitative table of EDS spectra it is seen that the metal matrix phase of aluminum is dominant with highest percentage in terms of weight.

### CONCLUSIONS

An Al7075/Ni-Cr/graphite composite material was successfully fabricated using the stir casting process. Mechanical testing of the MMC was conducted, revealing satisfactory tensile strength, hardness, and impact strength values. The pin-on-disc apparatus was used to evaluate different stir-cast specimen combinations, with wear results calculated based on the weight difference of specimens before and after testing. The wear characteristics and mechanical properties of the Al7075/Ni-Cr/graphite composite were analyzed, with findings indicating that the composite containing 4% graphite and 10% nickel-chromium outperformed other material combinations. The machining behavior of the MMC in WEDM was optimized using the Taguchi method prior to wear testing. The optimization revealed that current and voltage significantly impact output parameters such as surface finish and material removal rate (MRR). The composite material's properties improve with the addition of graphite up to a certain percentage, beyond which they decline due to strong interfacial bonding between the particles. Furthermore, the incorporation of nickel and chromium enhances the composite material's wear resistance. Overall, the data indicates that specimens with less than 4% graphite and higher nickel-chromium content exhibit superior wear resistance compared to other reinforced

compositions. Substituting the Al7075 alloy with the Al7075/Ni-Cr/graphite composite material can minimize wear and extend the material's lifespan. Future research could involve utilizing the Taguchi method in pin-on-disc testing, varying load, speed, and duration to optimize the reinforcement proportions in the base metal.

### REFERENCES

1. K. K. Chawla, Composite materials: science and engineering. Springer Science & Business Media, 2012.
2. T. Trzepieciński, S. M. Najm, M. Sbayti, H. Belhadjsalah, M. Szpunar, H. G. Lemu, *J. Compos. Sci.*, **5**, 217 (2021).
3. V. Chak, H. Chattopadhyay, T. L. Dora, *J. Manuf. Process.*, **56**, 1059 (2020).
4. N. K. Singh, S. Balaguru, *Silicon*, **16**, 45 (2024).
5. N. Sreedhar, S. Balaguru, *Int. J. Mech. Prod. Eng. Res. Dev.*, **10**, 391 (2020).
6. D. Davis, G. Marappan, Y. Sivalingam, B. B.; Panigrahi, S. Singh, *ACS Omega*, **5**, 14669 (2020).
7. M. L. Parucker, A. N. Klein, C. Binder, W. Ristow Junior, R. Binder, *Mater. Res.*, **17**, 180 (2014).
8. F. Nturanabo, L. Masu, J. B. Kirabira, *Aluminum Alloys Compos.* (2019).
9. V. Madeva Nagaral, S. A. Auradi, S. V. Kori, V. Hiremath, *J. Mech. Eng. Sci.*, **13**, 4623 (2019).
10. V. Bharath, V. Auradi, S. Madeva Nagaral, S. Babu Boppana, *J. Bio-Tribo-Corros.*, **6**, 45 (2020).
11. X. Han, D. Xu, D. Axinte, Z. Liao, H. N. Li, *J. Mater. Process. Technol.*, **288**, 116875 (2021).
12. D. Palanisamy, A.; Devaraju, N.; Manikandan, K.; Balasubramanian, D. Arulkirubakaran, *Mater. Today: Proc.*, **22**, 525 (2020).
13. R. Butola, C. Pratap, A. Shukla, Walia, *Mater. Sci. Forum*, **969**, 253 (2019).
14. K. R. Padmavathi, R. Ramakrishnan, *Procedia Eng.*, **97**, 660 (2014).
15. M. V. Krishna, A. M. Xavior, *Procedia Eng.*, **97**, 918 (2014).
16. D. Das, D. K. Roy, M. P. Satpathy, B. K. Nanda, R. K. Nayak, *Mater. Today: Proc.*, **18**, 3080 (2019).

17. K. Raju, M. Balakrishnan, C. B. Priya, M. Sivachitra, D. Narasimha Rao, *Adv. Mater. Sci. Eng.* **2022**, 4438419 (2022).
18. D. Dash, S. Samanta, R. N. Rai, *Adv. Mater. Process. Technol.*, **8**, 3344 (2022).
19. R. Bobbili, V.; Madhu, A. K. Gogia, *Eng. Sci. Technol. Int. J.*, **18**, 664 (2015).
20. E. Ekici, A
21. . R. Motorcu, A. Kuş, *J. Compos. Mater.*, **50**, 2575 (2016).
22. S. Madhavarao, V. V. S. Kesava Rao, C. Rama Bhadri Raju, T. Buddi, D. V. Nemova, R. D. Nautiyal, *Cogent Eng.*, **11**, 2328822 (2024).
23. G. C. da Silva Simioni, T. D. V. Pinheiro, G. D. L. Vasques, R. V. Lantmann, M. M. Lopes, M. Wettergreen, C. A. Dos Santos, *IEEE Trans. Instrum. Meas.*, 2023.
24. R. A. Manikandan, T. V. Arjunan, *Compos. Part B Eng.*, **183**, 107668 (2020).
25. M. Sánchez, J. Rams, A. Ureña, *Compos. Part A Appl. Sci. Manuf.*, **41**, 1605 (2010).
26. J. L. Li, Y. C. Xiong, X. D. Wang, S. J. Yan, C. Yang, W. W. He, S. L. Dai, *Mater. Sci. Eng. A*, **626**, 400 (2015).
27. R. T. Yang, C. J. Tzeng, Y. K. Yang, M. H. Hsieh, *Int. J. Adv. Manuf. Technol.*, **60**, 135 (2012).
28. S. Sarkar, S. Mitra, B. Bhattacharyya, *Int. J. Adv. Manuf. Technol.*, **27**, 501 (2006).
29. M. Subrahmanyam, T. Nancharaiah, *Mater. Today: Proc.*, **23**, 642 (2020).
30. D. Chen, J. Li, K. Sun, J. Fan, *Int. J. Adv. Manuf. Technol.*, **125**, 2925 (2023).
31. K. Kumar, B. M. Dabade, L. N. Wankhade, *Mater. Today: Proc.*, **44**, 2726 (2021).
32. A. Chatterjee, S. Sen, S.; Paul, K. Ghosh, M. Ghosh, G. Sutradhar, *J. Inst. Eng. India Ser. D*, **104**, 587 (2023).
33. A. Coyal, N. Yuvaraj, R. Butola, L. Tyagi, *SN Appl. Sci.*, **2**, 1 (2020).

## Silica gel chemically modified with ionic liquid – efficient sorbent for Au, Ir, Pd and Pt

O. Veleva<sup>1</sup>, K. Bacheva<sup>2</sup>, I. Dakova<sup>3</sup>, M. Karadjov<sup>1\*</sup>

<sup>1</sup>Geological Institute, Bulgarian Academy of Sciences, Acad. G. Bonchev Str. Bl. 24, 1113 Sofia, Bulgaria

<sup>2</sup>Research Center for Environment and Materials, Macedonian Academy of Sciences and Arts, Bul. Krste Misirkov 2, P.O. Box 428, 1000 Skopje, Republic of Nord Macedonia

<sup>3</sup>Faculty of Chemistry and Pharmacy, University of Sofia “St. Kl. Ohridski”, 1 Blvd. J. Bourchier, 1164 Sofia, Bulgaria

Received: October 01, 2024; Revised: November 20, 2024

The efficiency of sorption of noble metals on the sorbent synthesized *via* chemical modification of silica gel with ionic liquid containing methylimidazolium group was studied. The surface of the sorbent is positively charged, and results obtained indicate quantitative retention of negatively charged chlorido complexes of noble metals. Experiments carried out defined an optimal HCl concentration range (0.05-0.1 M HCl) for quantitative retention of Au, Ir, Pd and Pt using 30 min sorption time. Complete elution of sorbed elements was achieved with 0.5 M of thiourea in 0.5 M HCl. In addition, high selectivity of the sorbent was found toward the sorption of base metals (Fe, Cu, Mn, Ni, Zn) usually coexisting with noble metals in industrial and environmental samples. Analytical procedure was developed and validated for the determination of Au, Ir, Pd and Pt in soils and geological samples.

**Keywords:** ionic liquids, noble metals, sorption, soils, geological samples

### INTRODUCTION

Noble metals (Au, Ru, Rh, Pd, Os, Ir, Pt) are widely used in various industrial fields due to their properties such as electrical resistance, inertness to chemical attacks, hardness, excellent catalytic activity, which requires their reliable determination in environmental samples, raw materials, as well as in final products. Atomic spectrometric and mass spectrometric methods allow measurement of noble metals at low concentration levels, however the practical application of these methods in real samples is restricted by strong matrix interferences [1]. That is why separation and enrichment steps are generally included in most of the analytical procedures used for noble metals determination in environmental and industrial samples.

Solid phase extraction (SPE) is a preferable separation procedure because of its simplicity, reduced amounts of organic solvents used, high preconcentration factors and clean extracts. The properties of the incorporated sorbent are the most important factor for the high effectiveness of the developed SPE procedure. Various sorbents have been proposed for the SPE of noble metals [2–8]. Polymeric sorbents with high selectivity toward precious metals include functional groups such as thiourea [9], thiazole [10], dithiocarbamate [11], cysteine [12], ethylenediamine [13], 8-aminoquinoline [14], etc. Ionic liquids have been also used for SPE of noble metals in connection with

their ability to exchange negatively charged ions, e.g., for Au [15-19], Pd [20], Pt [21] and Pt(IV), Pt(II), and Pd(II) [22] in which imidazolium derivatives are bound to a polymer matrix.

In this paper, we use silica gel, an inert support chemically modified with 1-methylimidazolium groups (SiG-MIA) as a sorbent for SPE of noble metals. Extraction efficiency of the sorbent toward Au, Ir, Pd, Pt was studied in batch mode and optimal hydrochloric acid concentrations, contact time, and sorbent amount were defined. The results obtained indicate quantitative sorption of the chlorido complexes of Au, Ir, Pd, Pt from 0.05 M HCl with high selectivity even in the presence of base transition metals (Fe, Cu, Mn, Zn, Ni). The elution of the retained metals was achieved with 0.5 M thiourea in 0.5 M HCl. Based on the properties of the SiG-MIA sorbent an analytical procedure was developed for noble metals determination in soils, ore samples and copper concentrate. The accuracy and repeatability of the developed analytical procedures was confirmed by the analysis of certified reference materials.

### EXPERIMENTAL

#### *Apparatus*

The concentrations of noble metals were measured on an inductively coupled plasma optical emission spectrometer (ICP-OES, Jobin Yvon

\* To whom all correspondence should be sent:  
E-mail: [metodi@geology.bas.bg](mailto:metodi@geology.bas.bg)

Ultima 2) equipped with Meinhard glass concentric nebulizer and glass cyclonic chamber at optimal instrumental parameters (sheath gas 0.2 L/min, sample uptake 1 ml/min, plasma gas 12 L/min). All measurements were carried out at least in triplicate. The most sensitive wavelengths were used: Au 242.795 nm; Ir 224.268 nm; Pd 340.458 nm; Pt 214.423 nm.

Elemental analysis was performed using Euro EA CHNS-O elemental analyzer (EuroVector, Italy). An EBA 20 centrifuge (DJB Labcare Ltd., Newport Pagnell, England) was used to separate the silica particles from the solution containing noble metals in batch experiments.

#### Reagents and materials

All used reagents and solvents were of analytical-reagent grade. The stock standard solutions for Au, Ir, Pd and Pt were Sigma–Aldrich (Germany) in 5% HCl. The stock standard solutions for Cd, Cu, Co, Fe, Ni, Pb and Zn (1000 mg/L) were Titrisol, Merck (Darmstadt, Germany) in 2% HNO<sub>3</sub>. Working aqueous standard solutions were daily prepared by appropriate dilution with doubly distilled water. The elution solutions were prepared from nitric acid, hydrochloric acid, L-cysteine and thiourea (Merck, Darmstadt, Germany). All acids used in sorption, elution and digestion procedures are Suprapur, Merck, Germany.

Certified reference material OREAS 45d, Ferruginous soil; certified reference material OREAS 13d, gabbro (prepared from ores of platinum group elements (PGEs), copper, nickel and gold dispersed in a gabbro matrix), certified reference material OREAS 505d (porphyry Cu-Au certified reference material prepared from a blend of ores, barren granodiorite and minor additions of copper and molybdenum concentrates).

Reagents used to prepare the SiG-MIA sorbent were silica gel 60 (Merck, Darmstadt, Germany), 1-

methylimidazole (MIA), 3-(chloropropyl)-trimethoxysilane (TMSP) (Sigma–Aldrich, Munich, Germany) and methanol (Labscan, Dublin, Ireland).

#### Procedures

• *Sorbent synthesis.* A three-step synthesis procedure was used:

*First step:* The silica gel (SiG) surface was activated by refluxing (10 g SiG with 80 mL 6 M HCl for 8 h). After cooling, the activated silica gel (aSiG) was filtered and washed with deionized water until a neutral reaction and dried under vacuum at a temperature of 60°C for 8 h.

*Second step:* Synthesis of 1-(trimethoxysilyl propyl)-3-methylimidazolium chloride ([TMSP-MIA]Cl) was carried out according to the procedure described by Valkenberg *et al.* with some modifications [12]. A mixture of 1-methylimidazole (2.84 g, 34.5 mmol) and 3-(chloropropyl)-trimethoxysilane (6.86 g, 34.5 mmol) was refluxed under nitrogen for 48 h at 70°C. The obtained product was a yellow-colored viscous liquid which was purified by extraction with diethyl ether (twice).

*Third step:* The chemical grafting of ([TMSP-MIA]Cl) onto aSiG was performed by autocondensation and co-condensation of the silanol groups and methoxy groups of the TMSP-MIA chloride. For this purpose, 1.7 g of [TMSP-MIA]Cl was dissolved in 20 mL of methanol and 1 g of aSiG was dispersed in this solution. The resulting suspension was stirred continuously for 1 day at room temperature. After completion of the reaction, the solid phase was separated by centrifugation and washed three times with methanol to remove the unreacted [TMSP-MIA]Cl, and then the resulting material (SiG-MIA) was dried under vacuum at 60°C for 8 h. Schematically, the synthesis of the sorbent is presented in Figure 1.

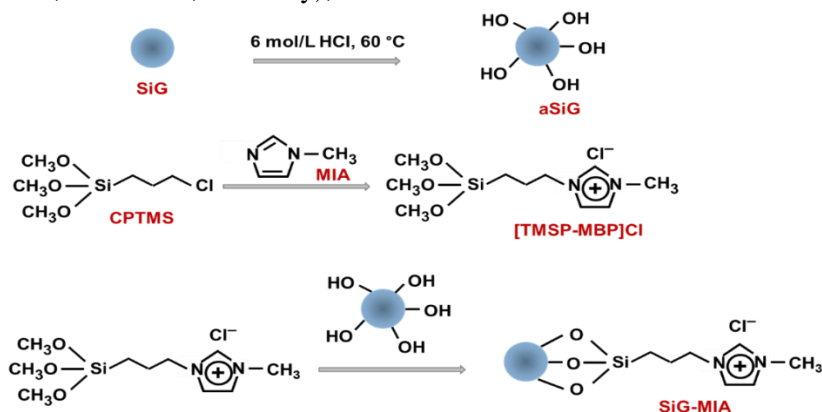


Fig. 1. Schematic representation of the synthesis of SiG-MIA.

- *Batch sorption procedure* The sorption efficiency of SiG-MIA toward chlorido complexes of Au, Ir, Pd and Pt was studied in a batch mode. The influence of HCl concentration on the degree of sorption of the analytes was investigated in the range 0.001 – 3 M. Aqueous solutions of HCl solution with desired concentration were mixed with 2 µg/ml of Au, Ir, Pd and Pt and 100 mg of SiG-MIA and shaken for 30 min. Samples were centrifuged (5800 rpm) for 10 min, supernatants were removed and concentrations of analytes were measured by ICP-OES. Degrees of sorption were calculated as follows:

$$D_S(\%) = \frac{A_i - A_{\text{eff}}}{A_i} \times 100, \quad (1)$$

where  $A_{\text{eff}}$  (µg) is the amount of the analyte in the supernatant solution and  $A_i$  (µg) is the initial amount of Au, Ir, Pd and Pt added.

- *Desorption studies.* Several mixtures of HCl acid and thiourea at different concentration levels were tested as potential eluents. All experiments were done after loading the sorbent with 2 µg of Au, Ir, Pd and Pt at optimal conditions, followed by treatment with 5.0 mL of each eluent for 30 min on an electrical shaker. Degree of elution ( $D_E$ , %) was defined as follows:

$$D_E(\%) = \frac{A_{\text{el}}}{A_i - A_{\text{eff}}} \times 100, \quad (2)$$

where  $A_{\text{el}}$  (µg) is the amount of Au, Ir, Pd and Pt in the eluate.

*A. Selectivity studies.* Model solutions containing 1000 µg/L of Fe, Cu, Mn, Zn, Ni were prepared in 0.05 M HCl, spiked with 100 µg/L of Au, Ir, Pd and Pt and mixed with 100 mg of SiG-MIA. The solutions were shaken for 30 min and centrifuged at 5000 rpm. The supernatant was removed and all elements were measured by ICP-OES. The SiG-MIA particles were washed with distilled water and shaken with 5 mL of 0.5 M thiourea in 0.5 M HCl for 30 min. After centrifugation the elements Au, Ir, Pd and Pt were measured in the eluate by ICP-OES. The degrees of sorption and elution were calculated using equations 1 and 2, respectively.

*B. Procedure for Pd, Pt u Rh determination in soils after aqua regia digestion.* A sample of approximately 2000 mg of soil sample was weighed in a PTFE beaker covered with a glass watch. A mixture of 21 ml conc. HCl and 7 ml conc. HNO<sub>3</sub> was added and samples were left to stay overnight. The sample solution was digested for about 3 h in the PTFE beaker covered with a glass watch. Then the watch glass was removed, 20 ml of HF were added and digestion continued until near dryness. The residue was dissolved in 5 mL of 0.5 M HCl on the

hot plate, the solution was transferred to a 25 mL volumetric flask and diluted up to the mark with doubly distilled water. A sample of 20 mL was filtered and transferred to a centrifuge tube. About 100 mg of the SiG-MIA sorbent was added and the sample was shaken for 30 min. After centrifugation, supernatant was removed, sorbent was washed with doubly distilled water and elution was carried out with 5 mL of 0.5 M thiourea in 0.5 M HCl. After centrifugation Au, Ir, Pd and Pt were measured in the supernatant by ICP-OES at optimal instrumental parameters.

*C. Procedure for Au determination in ore and copper concentrate.* A sample of copper concentrate of approximately 1000 mg was weighed in a PTFE beaker, a mixture of 12 mL of conc. HCl and 4 mL of conc. HNO<sub>3</sub> was added and the sample was left to stay overnight. The sample solution was digested for about 6 h in the PTFE beaker covered with a watch glass. Then the watch glass was removed and digestion continued until near dryness. The residue was dissolved in 5 mL of 0.5 M HCl, transferred to a 25 mL volumetric flask and diluted up to the mark with doubly distilled water. Two parallel samples of 10 mL were filtered and transferred to centrifuge tubes. About 100 mg of SiG-MIA sorbent was added and both samples were shaken for 30 min. After centrifugation, the supernatant was removed, sorbent was washed with doubly distilled water and elution was carried out with 5 mL of 0.5 M thiourea in 1 M HCl. After centrifugation Au, Pd, and Pt were measured in the supernatant by ICP-OES at optimal instrumental parameters.

## RESULTS AND DISCUSSION

### *Sorbent synthesis*

The successful synthesis of the sorbent was demonstrated by comparing the infrared spectra of the starting material (aSiG) and the final product (SiG-MIA). The bands at 473, 802 and 1097 cm<sup>-1</sup> observed in the spectra of both investigated materials are related to the Si–O–Si group in the silica gel. The broad band in the interval 3200–3600 cm<sup>-1</sup>, present in both spectra, is due to the vibrations of the silanol –OH groups. The spectrum of SiG-MIA shows bands at 2854, 2926 and 2971 cm<sup>-1</sup> which prove the occurrence of C–H vibrations due to the presence of –CH<sub>2</sub> groups in the propyl residue in [TMSP-MIA]Cl. The bands at 1571 cm<sup>-1</sup> and 1653 cm<sup>-1</sup> are due to the C=C and C=N groups in the imidazole ring, respectively. This is evidence that SiG-MIA contains methylimidazole groups. The success of the synthesis procedure was also evaluated by elemental analysis of the prepared SiG-MIA.

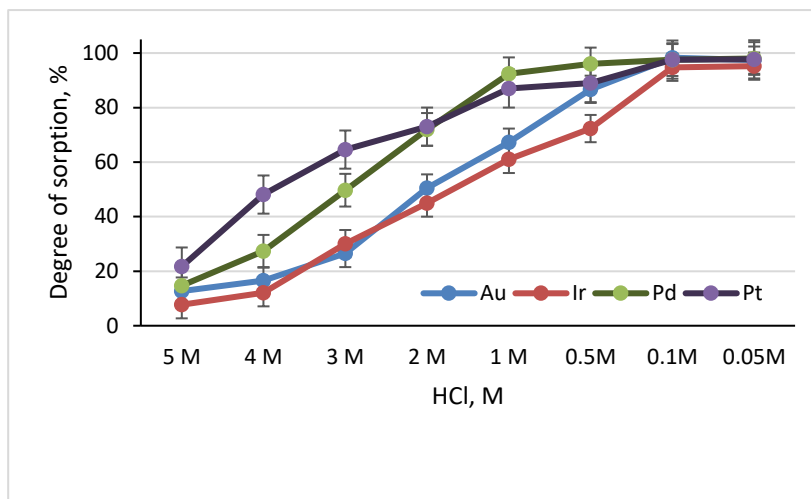


**Fig. 2.** The effect of HCl concentration on the degree of sorption of Au, Ir, Pd and Pt with SiG-MIA (three parallel experiments).

The results (7.27 wt. % C and 1.84 wt. % N) proved that the 1-(trimethoxysilylpropyl)-3-methylimidazolium fragment was successfully bound to the silica gel surface. The content of 1-methylimidazole groups was calculated to be 0.76 mmol per gram of sorbent.

#### Optimization studies of the extraction efficiency

- *Sorption efficiency.* The sorbent SiG-MIA might be accepted as a strongly basic anion exchanger due to the positively charged 1-methylimidazolium functional groups on its surface. This suggests the adsorption of the anionic chlorido-complex species of the studied noble metals which will depend on the HCl concentration.



The effect of HCl concentration on the degree of sorption of Au, Ir, Pd and Pt on MIA-PG was investigated in a wide range of HCl concentrations from 0.05 to 3.0 M and the results are presented in Figure 2. The main conclusions that can be drawn from these results are as follows:

- in all cases the degree of sorption of the corresponding analyte increases with decreasing hydrochloric acid concentration;
- quantitative sorption is achieved at HCl concentration: for Au at 0.05 – 0.1 M HCl; for Ir at 0.05 – 0.1 M HCl; for Pd at 0.05 – 0.5 M HCl; for Pt at 0.01 M – 0.05 M HCl.

The first conclusion might be explained by the fact that there is competition between chloride anions and anions of chlorido complexes of metals for a positively charged binding site on the sorbent surface. At high concentrations of hydrochloric acid the interaction with the chloride anions predominates, while at low concentrations the interaction with the anions of the chlorido complexes

of the metals prevails. Results obtained undoubtedly showed that at the optimal 0.05 M HCl, the proposed SiG-MIA sorbent ensures quantitative sorption for Au, Ir, Pd, and Pt. Experiments were performed to optimize the amount of SiG-MIA particles for the highest degree of sorption. Results showed that for the studied range 50–150 mg sorbent, the sorption was quantitative with at least 100 mg of SiG-MIA sorbent.

- *Sorption kinetics.* The sorption kinetics is an important characteristic of sorbents for its practical application. The sorption kinetics of Au, Ir, Pd and Pt was determined in a batch mode at the selected optimal concentration of hydrochloric acid of 0.05 M HCl for a sorption time ranging from 5 to 60 min. The results indicate a relatively fast sorption process. All studied analytes Au, Ir, Pd and Pt were quantitatively retained on the sorbent surface in 30 min, so this time was used in further experiments.

- *Desorption step.* The SiG-MIA sorbent, as a strong basic anion exchanger, is highly efficient for the retention of negatively charged chlorido complexes of Au, Ir, Pd and Pt from acidic media, but this also means relatively difficult desorption in the presence of any acid used as an elution reagent. As seen from the data presented in Table 1, the degree of elution is very low even if 3M HCl is used (higher HCl concentration affects the stability of functional groups on the surface of the sorbent). This means that the competitive complex formation using a chelating agent would be more effective in such case since the elution will be due to the decomposition of the chlorido complexes of Au, Ir, Pd and Pt and the formation of new more stable chelate complexes with the chelating agent used. The ligands thiourea and L-cysteine are well-known for their ability to form stable complexes with Au, Ir, Pd and Pt due to the presence of both amine and

sulfur groups. Experiments were carried out with mixtures of thiourea and L-cysteine in HCl in various concentrations, showing quantitative desorption of Au, Ir, Pd and Pt in 30 min. with 0.5 M thiourea in 0.5 M HCl (see Table 1).

**Table 1.** Degree of elution ( $D_E$ , %) for Au, Ir, Pd and Pt from SiG-MIA using different eluents.

Eluent	Degree of elution, %			
	Au	Ir	Pd	Pt
3 M HCl	32±5	12±3	22±5	18±5
0.2 M TU + 0.2 M HCl	85±6	81±5	88±5	86±5
0.5 M TU + 0.5 M HCl	98±2	96±3	97±3	95±3
0.5 M TU + 1 M HCl	99±2	98±2	98±2	96±2
0.2 M Cys + 0.2 M HCl	80±5	75±5	77±5	74±5
0.5 M Cys + 0.5 M HCl	90±4	80±4	81±4	83±5
0.5 M Cys + 1 M HCl	92±4	82±4	85±4	84±5

**Desorption kinetics.** To determine the desorption kinetics of the chlorido complexes of Au, Ir, Pd and Pt from the surface of SiG-MIA, experiments were performed in a static mode using the elution mixture 0.5 M thiourea in 0.5 M HCl with desorption times ranging from 10 to 60 min. It was found that complete elution is achieved for all studied analytes with 2-5 ml of 0.5 M thiourea in 0.5 M HCl for 30 min.

**Selectivity studies (Solid phase extraction of a mixture of base transition and noble metal).** Matrix interferences are the most serious problem for the determination of Au, Ir, Pd and Pt in complicated samples such as soils and geological samples. That is why the selectivity of the sorbent is of utmost importance. The selectivity of SiG-MIA was studied following the procedure described in paragraph A. Results obtained are presented in Table 2 and undoubtedly showed that even in the presence of high levels of coexisting base metals the recovery of Pd, Pt, Ir, and Au ions is more than 95% at the optimal HCl concentration of 0.05 M.

These results are expectable because Fe, Cu, Zn, Mn, Ni, Cd and Pb exist in sample solution as positively charged ions and are repelled by the

positively charged methylimidazole group on the surface of the sorbent. This makes SiG-MIA a highly suitable and promising sorbent for the quantification of noble metals in complicated matrices, ensuring interference-free measurement by ICP-OES.

**Table 2.** Selectivity studies – degree of sorption  $D_s$  (%) (mean±SD) of Au, Ir, Pd and Pt in the presence of 500 mg/L of base metals (three parallel experiments).

Element	Degree of sorption, $D_s$ [%]
Au	98±2
Ir	96±2
Pd	97±1
Pt	98±2
Fe	<3
Cu	<1
Zn	<3
Mn	<1
Ni	<4
Cd	<4
Pb	<3

**Determination of Pd and Pt in soils.** The sorbent SiG-MIA was used in an analytical procedure based on solid phase extraction for the determination of Pd, Pt, Ir, and Au in soil samples. The soil sample was digested on a hot plate with a mix of HCl+HNO<sub>3</sub>+HF for about 4 h. The dry residue obtained after soil digestion was dissolved in 5 mL of 0.5 M HCl, transferred to a 25 mL volumetric flask and diluted up to the mark, ensuring final optimal HCl concentration for the subsequent separation of Pd and Pt. Two parallel samples were used for the determination of Pd and Pt following the procedure described in paragraph B. The developed analytical procedure was applied to the CRM OREAS 45d, results obtained are presented in Table 3. Recoveries achieved for both elements, calculated based on the certified values were above 95%. Relative standard deviations varied between 6 and 11%. Calculated limit of quantification (10  $\sigma$  criterion) based on the purity of acids used is 15 ppb for all analytes. The developed procedure is suitable for the analysis of soil samples.

**Table 3.** Recoveries achieved for studied elements and results for certified values (presented as in the certificate), (three parallel samples).

Sample	Element	Recovery, (%)	Certified values	Results
			Mean, ppb (sd)	Developed procedure
			Mean, ppb (sd)	Mean, ppb (sd)
CRM OREAS 45d (soil)	Au	96±2	23 (2)	22 (2)
	4	98±2	34.6 (2.3)	34 (3)
	Pt	101±2	48.5 (3.1)	49 (4)
CRM OREAS 13b	Au	98±2	211 (13)	208 (16)
	Pd	101±3	131 (9)	132 (12)
	Pt	97±2	197 (13)	191 (15)
CRM OREAS 505d	Au	99±2	552 (23)	549 (29)

*Determination of Au, Pd, Pt in polymetallic ore and copper concentrate.* Several copper mines are situated in Bulgaria and determination of Au, Pd and Pt in copper ore and copper concentrate is an important analytical task. The high selectivity of the SiG-MIA sorbent permits the development of an analytical procedure for Au, Pd, and Pt determination in copper concentrate. In this case *aqua regia* is conventionally used for sample digestion although the sample is only partially dissolved (experimental results confirmed complete dissolution of Au, Pd, and Pt). Analytical procedure described in paragraph C was applied to the CRMs OREAS 13b and OREAS 505d. The data, presented in Table 3, demonstrate a very good agreement between obtained results and certified values, thus confirming the validity of the developed procedure. Relative standard deviations varied between 7-12%. Calculated limit of quantification (10  $\sigma$  criterion) based on the purity of acids used is 30 ppb for all analytes. The procedure is simple and easy to apply, suitable for laboratory practice in mining and industrial laboratories.

Model experiments showed that the extraction efficiency of the sorbent statistically dropped down after at least 20 sorption/desorption cycles. In addition, the sorption efficiency of the sorbents prepared by different batches is almost identical, confirming the repeatability of synthesis procedure.

#### CONCLUSION

In the present study, a new sorbent was synthesized based on the grafting of 1-(trimethoxysilylpropyl)-3-methylimidazolium chloride onto the surface of submicron silicon spheres, which was characterized by elemental analysis and IR spectroscopy. The sorbent showed high selectivity: in 0.05 M HCl the retention of Au, Ir, Pd and Pt is quantitative, while the sorption of base transition metals is negligible. The sorbed noble metals are effectively eluted with 0.5 M thiourea in 0.5 M HCl. Based on these results, the sorbent was incorporated in analytical procedures developed for the determination of Au, Pd and Pt in soils, polymetallic ore and copper concentrate. The validity and versatility of the proposed analytical procedure was confirmed by the analysis of suitable certified reference materials.

#### REFERENCES

1. G. Schlamp, Noble metals and noble metal alloys, in: Springer Handbook of Materials Data. H. Warlimont, W. Martienssen (eds.), Springer: Berlin, Heidelberg, Germany, 2018; p. 339.
2. E. Mladenova, I. Karadjova, D. Tsalev, *J. Sep. Sci.*, **35**, 1249 (2012).
3. K. Pyrzynska, Application of solid sorbents for enrichment and separation of platinum metal ions. in: platinum metals in the environment, F. Zereini, C. Wiseman (eds.), Springer: Berlin, Heidelberg, Germany, 2015, p. 67.
4. H. Ehrlich, T. Buslaeva, T. Maryutina, *Russ. J. Inorg. Chem.*, **62**, 1797 (2017).
5. Z. Chang, L. Zeng, C. Sun, P. Zhao, J. Wang, L. Zhang, Y. Zhu, X. Qi, *Coord. Chem. Rev.*, **445**, 214072 (2021).
6. S. Sharma, A. Kumar, N. Rajesh, *RSC Adv.*, **7**, (2017).
7. P. Cyganowski, *Solvent Extr. Ion Exch.*, **38**, 143 (2020).
8. D. Kong, S. Foley, L. Wilson, *Molecules*, **27**(3), 978 (2022).
9. T. Dharmapriya, D. Lee, P. Huang, *Recycle. Sci. Rep.*, **11**, 19577 (2021).
10. C. Xiong, S. Wang, L. Zhang, Y. Li, Y. Zhou, J. Peng, *Polymers*, **10**, 159 (2018).
11. H. Kinemuchi, B. Ochiai, *Adv. Mater. Sci. Eng.*, **1**, (2018).
12. E. Mladenova, I. Dakova, I. Karadjova, M. Karadjov, *Microchem. J.*, **101**, 59 (2012).
13. A. Nastasovic, S. Jovanovic, D. Jakovljevic, S. Stankovic, A. Onjia, *J. Serbian Chem. Soc.*, **69**, 455 (2004).
14. B. Zhang, S. Wang, L. Fu, L. Zhang, *Polymers*, **10**, 437 (2018).
15. J. Yang, F. Kubota, N. Kamiya, M. Goto, *J. Chem. Eng. Japan*, **48**(3), 197 (2015).
16. Z. Xu, Y. Zhao, W. Liang, P. Zhou, Y. Yang, *Inorg. Chem. Front.*, **5**, 922 (2018).
17. X. Liu, R. Liu, Y. Lu, Q. Sun, W. Xue, M. Cheng, Y. Yang, *Sep. Purif. Technol.* **328**, 125049 (2024).
18. X. Liu, R. Liu, X. Yin, Y. Wang, W. Xue, Y. Yang, *Chem. Eng. J.*, **483**, 149124 (2024).
19. W. Gui, Y. Shi, J. Wei, Z. Zhang, P. Li, X. Xu, Y. Cui, Y. Yang, *New J. Chem.*, **44**, 20387 (2020).
20. X. Kou, Y. Huang, Y. Yang, *J. Hazard. Mater.*, **420**, 126623 (2021).
21. X. Zhang, Y. Yang, Y. Wu, X. Xu, Z. Huang, *J. Environ. Chem. Eng.*, **11**, 110683 (2023).
22. Z. Xu, Y. Zhao, P. Wang, X. Yan, M. Cai, Y. Yang, *Ind. Eng. Chem. Res.* **58**, 1779 (2019).

# The application of an energy metric (EROI) for the analysis of a city energy profile

I. K. Iliev<sup>1\*</sup>, A. V. Fedyukhin<sup>2</sup>, Y. V. Yavorovsky<sup>2</sup>, H. I. Beloev<sup>3</sup>

<sup>1</sup>Department of Heat, Hydraulics and Environmental Engineering, "Angel Kanchev" University of Ruse, 7017 Ruse, Bulgaria

<sup>2</sup>Department of Energy Efficiency and Hydrogen Technology, National Research University Moscow Power Engineering Institute, Moscow 111250, Russia

<sup>3</sup>Department of Agriculture Machinery, "Angel Kanchev" University of Ruse, 7017 Ruse, Bulgaria

Received: November 09, 2024; Revised: November 20, 2024

Energy return on investment (EROI) is an energy metric used to build models comparing different energy extraction, transport, and use options. Its demand to date is determined by two limitations: the development of correct calculation and forecasting methods, as well as establishing the limits of practical applicability. This article proposes a solution to the second limitation, namely, the calculation of the weighted average EROI of a city's electrical energy consumption system. This value can be useful in the analysis of the fuel and energy balance, economic development potential, and sustainability of a city energy system. The authors calculated the balance of the energy system based on the volume of electrical energy consumption for 4 megacities of the world: Toronto-Hamilton-Oshawa, New York, London, and Moscow, indicating the estimated weighted average EROI based on the world average values of each energy resource. A comparison of the weighted average EROI of London and Moscow calculated using global and local values is presented. The results show that EROI for local energy resources allows for a more reliable calculation for individual cities.

**Keywords:** EROI, urban planning, urban energy system, energy consumption, energy conservation, urban metabolism.

## INTRODUCTION

There are about 20 cities in the world with a population of over 10 million people. Moreover, this value is typically used to designate a city not as a set of historically developed areas, but as a modern urban agglomeration consisting of several settlements. Examples of such agglomerations are Toronto - Hamilton - Oshawa or Tokyo - Yokohama. Electrical energy consumption by the world's megacities accounts for approximately 10% of global consumption. In turn, modern trends towards energy saving and carbon neutrality are in clear contradiction with the positive dynamics of energy consumption growth that have been established over the past decades. Of research interest is the question of the practical applicability of an indicator such as EROI for analyzing a city's supply of energy resources. This article analyzes certain aspects of the energy structure of the world's megacities with the prospect of obtaining an answer to the above question.

## APPLICATION OF EROI AS AN ENERGY, ECONOMIC AND SOCIAL INDICATOR

The structure of power generation in megacities is extremely diverse, especially taking into account the fact that electricity can be transmitted over tens or hundreds of kilometers, and power plants are located outside the cities and regions in question. It is

customary to highlight EROI as one of the indicators of energy resource efficiency: energy return on investment - the ratio of energy received to energy expended or energy profitability [1, 2]. This indicator is often used when constructing economic models to compare different options for energy production, transport and use [3, 4], as well as to select a priority energy transition model [5].

Article [6] is devoted to a review of economic assessments of oil and gas resources, including EROI. The authors note the appeal of using EROI compared to traditional methods of economic assessment: net present value, differential rent due to its comprehensiveness and consideration of an expanded range of costs: energy production, transport, environmental safety, energy efficiency. In addition to analyzing methodological approaches, the article presents statistical data on a number of energy carriers, for example, EROI of shale oil in the United States in the period from 2010 to 2015.

EROI is often used to analyze the prospects for the use of renewable energy sources (RES). In particular, in [7] this indicator is considered as one of the barriers to the development of renewable energy sources, along with a shortage of fresh water, rare earth metals and the intermittent nature of generation. In [8], along with the energy and economic applicability of EROI, the authors note its social significance. It is noted that EROI = 12 is the

\* To whom all correspondence should be sent:  
E-mail: iki@uni-ruse.bg

minimum for the existence of a society, conversely an EROI = 5 is associated to a possibility of famine.

A similar analysis is presented in works [9, 10], which establish a connection between EROI and the human development index, along with other social indicators. Noting the correlation between these indicators, the authors emphasize the need to increase the availability of energy resources with a high EROI in developing countries [9]. Table 1 shows the minimum EROI value for the existence of various types of activities according to [8].

In [11], EROI is considered as a dynamic indicator of the profitability of an energy source. It is shown that the EROI of oil and gas in the US decreased markedly over the 100 years spanning the period between 1910 - 2010 from 1200 to just 10, with that trough having already been reached in the 1960s. Moreover, it has shown extremely weak negative dynamics since then. In Canada the EROI of oil and gas was 16 in 2005. It is important to note that the EROI of oil and gas is typically calculated jointly, since oil and gas fields are often coupled.

**Table 1.** Minimum EROI value for the existence of various types of activities

Activity	Minimum EROI
Art	14
Medicine	12
Education	9 – 10
Family support	8 – 9
Healthy eating	5
Transport	3
Energy recycling	1.2
Energy generation	1.1

In [12] the dynamics of oil and gas EROI are also analyzed on average both worldwide and for some individual countries: USA, Canada, China, Mexico, Norway. It is shown that the world average for the period from 1990 to 2010 decreased from 32 to 20. For individual countries, the EROI of oil and gas is respectively: USA - 12 (2007), Canada - 15 (2010), China - 10 (2010). Mexico – 45 (2009), Norway – 21 (2008).

In [13] EROI values are given for all energy resources used in the UK: 3.6 – coal, 1.7 – oil, 14 – natural gas, 30 – nuclear energy, 1.1 – biomass, 58 – hydropower, 18 – wind energy, 3.3 – 8.6 – solar energy. The average EROI for all types of energy carriers in the UK is 9.0 [14]. The papers [15, 16] present data on EROI for gas in China produced from various sources: oil and gas fields, shale gas, etc. The indicator, as a rule, varies from 10 to 13, with the exception of synthetic gas from coal, for

which the EROI is 5. Similar data for China can be found in [17]: 10.0 – oil and gas, 25 – coal. For Russian natural gas, EROI is 74 according to data for 2016 [18]. At the same time, this value has been in the 70-83 range for 12 years.

Article [19] is an extensive study devoted to methodological approaches for assessing EROI for renewable energy sources. Researchers consider 3 global scenarios for the energy transition by 2060 with a share of renewable energy sources equal to 50, 75 and 100%, respectively. It is predicted that for the first scenario the integral world EROI in 2060 will be 10, and for the second and third scenarios - 6 and 3 – 5 respectively. It is rightly noted that scenarios 2 and 3 will lead to a decrease in EROI below the threshold values (EROI = 10 – 15) necessary for the functioning of modern industrial society. An additional factor limiting the development of renewable energy sources is the excess of the required volume of valuable metals in relation to the known one. In particular, for Scenario 3 (100% renewable energy sources by 2060), the estimated total mining demand will exceed current reserve levels for tellurium, indium, tin, silver and gallium. When planning an energy transition, it is usually assumed that the only significant constraints are political and economic (i.e., government political will and monetary investment). However, the results presented in [19] show that the EROI of the power system is also an important factor that should be taken into account when assessing the rate of implementation of renewable energy sources.

There are a number of publications devoted to a specific energy carrier. In particular, in [20] the EROI of solar energy is calculated for Swiss conditions. Depending on the calculation method, this indicator varies from 7 to 10, which, according to the authors, is a decent result for the energy carrier in question. However, the weak point of such studies is often the neglect of the need for energy storage, especially given the significant contribution grid-tied storage makes a to the EROI for renewable energy sources. At the same time, there are works in which the optimal storage capacity is calculated based on the problem of maximizing the “solar power plant – electrochemical storage” energy unit. In [21] it is shown that a correctly selected storage device can increase the EROI of a power plant using renewable energy sources by 1.5 – 2.0 times, although, as a rule, the need to introduce network storage devices reduces the technical and economic indicators of such installations [22].



**Fig. 1.** Forecast of global average EROI for various types of energy resources until 2050

In [23] a forecast of the global average EROI for various types of energy resources until 2050 is presented.

The authors consider several scenarios for the energy transition with different shares of renewable energy sources in the future. Fig. 1 shows data only for the base scenario.

Based on the review, it becomes obvious that there are several different methods for calculating EROI, which take into account different amounts of energy costs for obtaining, transporting the energy resource and waste disposal during its use. For example, the wide spread of EROI for nuclear energy (from 5 to 75) is due to both the availability of the initial resource for an individual country and the cost of processing or disposal of waste.

#### EROI OF A CITY ENERGY SYSTEM

As a practical application of EROI, it is proposed to use the following criterion: the weighted average EROI of the given city’s electrical energy consumption system:

$$EROI_{city} = \frac{\sum_{i=1}^n W_i \cdot EROI_i}{W_{sum}}$$

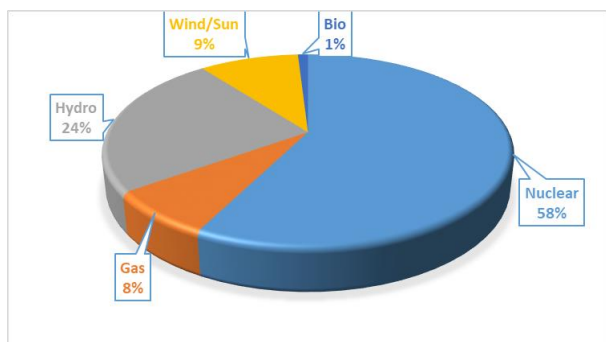
where:  $EROI_{city}$  is the weighted average EROI of the city’s electrical energy consumption system;  $EROI_i$  is the EROI value of the  $i$ -th energy resource used to generate electrical energy for the needs of the city;  $W_i$  is the volume of electricity consumption in the city using the  $i$ -th energy resource;  $W_{sum}$  is the total volume of electricity consumption in the city.

It is important to note that from a practical point of view, to obtain a snapshot for the reporting period (month, quarter, year), it is necessary to use the

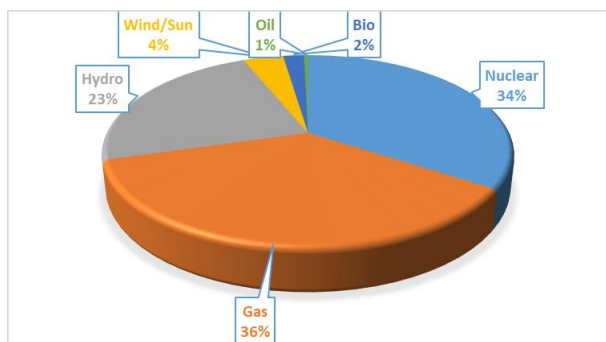
actual electricity production from various sources / the volume of electricity consumption by the city, and not the installed capacity of a power plant. In that case, it is possible to track the seasonality factor and the influence of the load factor on the city’s energy balance. For example, power plants using renewable energy sources (solar, wind) often have a load factor several times lower than that of power plants using fossil fuels. Then their share in the city’s energy balance in terms of installed capacity can reach 10–20%, and in terms of output – 3–5%, which results in increased accuracy through adjustments to the calculation of the weighted average EROI of the city’s electrical energy consumption system.

Fig. 2 shows the balance of the energy system based on the volume of electrical energy consumption for 4 megacities of the world: Toronto-Hamilton-Oshawa, New York, London, Moscow, indicating the estimated weighted average EROI based on the world average values of each energy resource [23]. For Moscow, natural gas is accepted as the only type of fuel, for the other cities - data from official government sources is used: Toronto-Hamilton-Oshawa [24], New York [25], London [26].

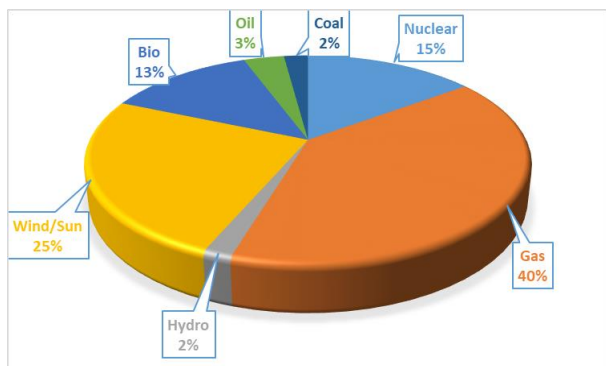
Based on the data presented in Fig. 2 we can conclude that the weighted average EROI of the world’s megacities under consideration is approximately the same ranging between 11 - 14 and weakly depends on the structure of electrical energy consumption. However, this logic is sound only if we operate with the world average EROI of energy resources according to [23,31,32]. When working with EROI for local (national) energy resources, the situation is in sharp contrast.



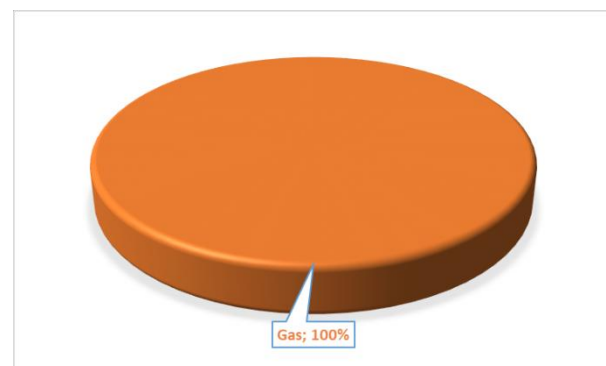
a) Toronto-Hamilton-Oshawa,  $EROI_{city}=11.3$



b) New York,  $EROI_{city}=12.3$



c) London,  $EROI_{city}=11.7$



d) Moscow,  $EROI_{city}=13.9$

**Fig. 2.** Balance of urban electricity consumption and weighted average EROI

Figure 3 shows a comparison of the weighted average EROI of London and Moscow calculated

using global averages [23] and local values, respectively [13, 18].

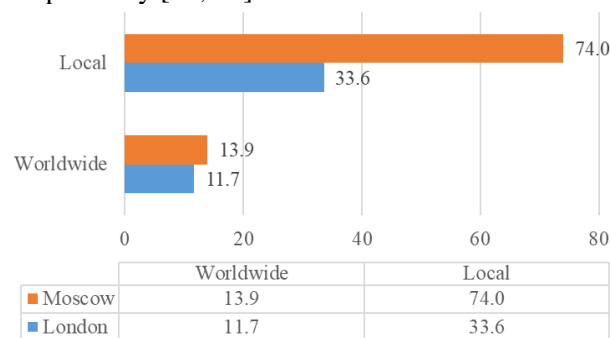


**Fig. 3.** Weighted average EROI of the electrical energy consumption system of Moscow and London calculated using global average and local values

From Fig. 3 it follows that EROI for local energy resources allows for a more reliable calculation for individual cities, obtaining results that are several times higher than the results when calculating using world average values. It is important to note that for both London and Moscow, the weighted average EROI is multiple times higher than the threshold values ( $EROI = 10 - 15$ ) necessary for the functioning of a modern industrial society.

Another significant result that can be obtained by analyzing global average data through tracking the projected dynamics of the EROI for the period up to 2050. The data presented in [23] indicate that EROI for renewable energy sources have negative dynamics in the future 2050, and the EROI of oil and gas – positive. Obviously, this factor will lead to an additional reduction in the weighted average EROI of the electrical energy consumption system of a city or state when implementing “green” energy transition measures.

#### ANALYSIS OF MEGACITIES ENERGY TRENDS

The electronic resource Metabolism of Cities [27] has an extensive database of statistics on the consumption of fuel and energy resources by cities over the past 20–25 years, indicating the source of information (usually scientific publications in international ranking journals). Figs. 4 – 7 present data on the dynamics of energy consumption, water and the volume of waste disposal in the largest cities of the world, built on the basis of the Metabolism of Cities resource.

The presented figures demonstrate that in the first decade of the twenty first century there was a significant (in some cases two- and three-fold increase) consumption of energy and fresh water by the world's megacities. The task of adequately

comparing the climate (energy and ecological) efficiency of large megacities remains not only significantly relevant, on the contrary, the reckless use of conventionally calculated indicators of greenhouse gas emissions (without taking into account the main abundant greenhouse gas - steam) in the mythical coverage areas of large agglomerations does not provide a sufficient understanding of the essence of what is happening in cities., Gaining an insight into the real energy-ecological efficiency of the urban metabolism, would aid the development of effective measures to increase efficiency.

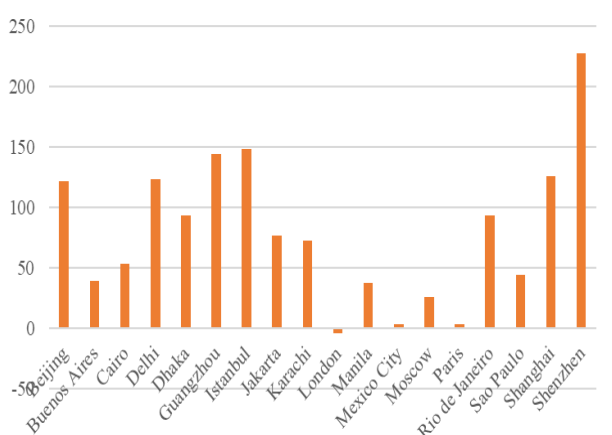


**Fig. 4.** Dynamics of energy consumption by stationary sources, % 2001 - 2011

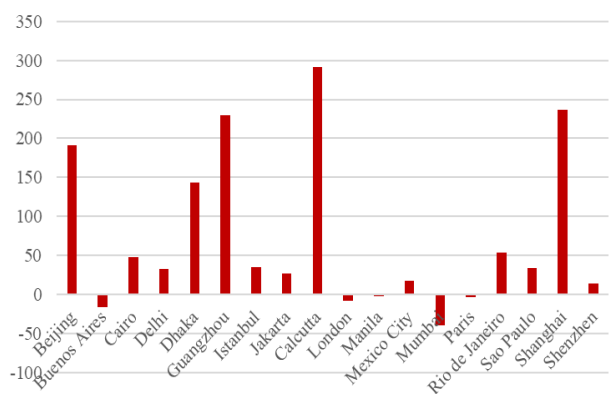


**Fig. 5.** Dynamics of energy consumption by transport, % 2001 - 2011

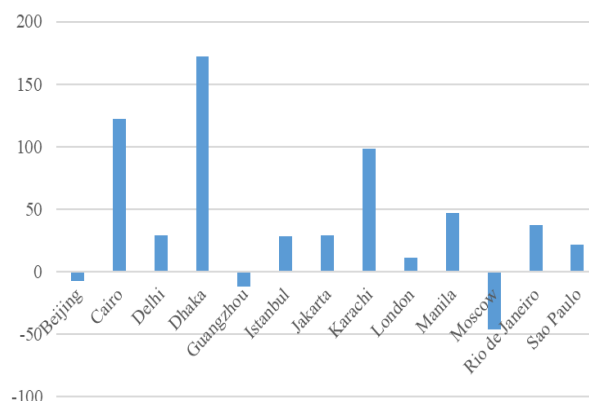


**Fig. 6.** Dynamics of water consumption, % 2001 - 2011

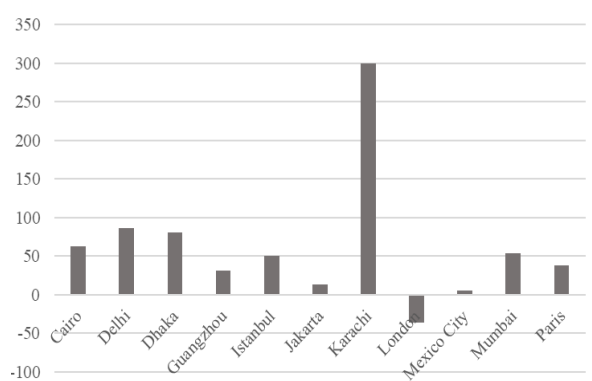


**Fig. 7.** Dynamics of waste disposal, % 2001 - 2011

Global challenges to environmental safety include the impacts of climate change on the planet, the increased consumption of natural resources amidst declining reserves, the loss of biodiversity and more. Among the mechanisms for implementing state policy in this area is the creation of an environmental audit system, informing the population and organizations about dangerous hydrometeorological and geophysical phenomena, the environmental state, and the introduction of comprehensive environmental permits for environmentally hazardous industries using the best available technologies.

Fig. 8 shows the results of calculating the specific consumption of electric energy from a city's population. For easier interpretation of the graphical information, only cities with an annual electricity consumption exceeding 5000 kWh/person are labelled on the scatter plot.

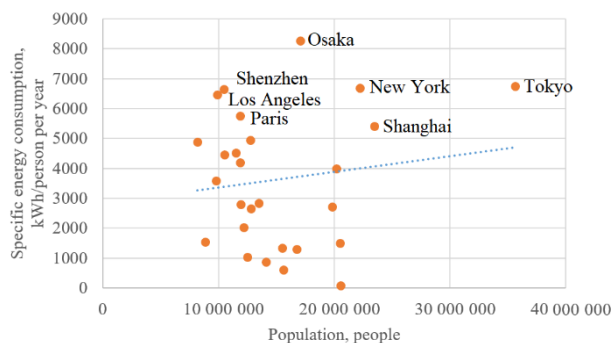


**Fig. 8.** Electricity specific consumption of population (kWh/person/year)

The trend line (marked in blue) shows a weak growth dynamics of the indicator as a function of population, which may signify that the energy limit under the modern structure of electric energy consumption by the city is about 7000 kWh/person per year. Further population growth of the city to 15, 20 or 30 million people represents a repetition of existing practices of energy production and consumption, adjusted for regional and climatic features. For instance, for Moscow this figure is only 4516 kWh/person per year.

Fig. 9 shows the dependence of the density of electric energy consumption on the density of the population. In this calculation, the population density was calculated not per square kilometer of urban territory, but per square kilometer of urbanized territory within the city.

Despite some dispersion of values due to the different social and economic specifics of the megacities of the world, in Fig. 9 one can observe an established trend of growth in the density of electric energy consumption, which is about 30 GWh/km<sup>2</sup> with an increase in population density by 10 thousand people/km<sup>2</sup>. Thus, an increase in the density of living per person increases electricity consumption by an average of 3,000 kWh/person per year. By analogy with Fig. 8, Fig. 9 shows only the largest cities in terms of the indicator under consideration.

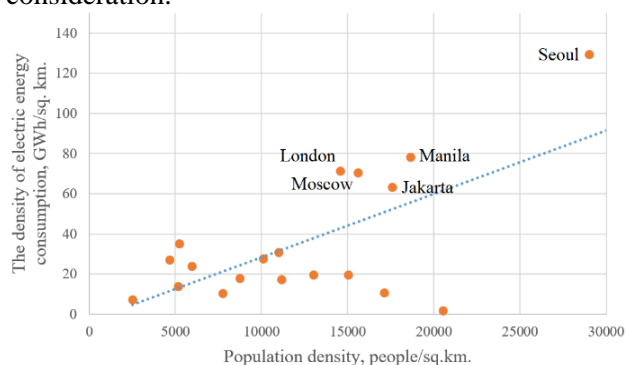


**Fig. 9.** The density of electricity consumption of population (GWh/km<sup>2</sup>).

Table 2 presents 5 groups of urban metabolism factors: energy, climate, environmental, municipal and economic.

**Table 2.** Groups of factors of the metabolic profile of the city

Groups of factors	Factors
Energy	Consumption of electrical energy Energy consumption by mobile units
Climate	Solar radiation Precipitation
Ecology	Harmful substances emissions Greenhouse gas emissions Greenhouse gas absorption capacity
Municipal	Water consumption Solid municipal waste disposal
Economy	GDP (gross domestic product) EROI (energy returned on energy invested)

The factors listed are of interest both in absolute and specific (for example, per capita) terms. At the same time, the key point in building a metabolic profile is the correctness of the initial data, especially when it comes to comparing different cities. This also applies to the collection of information within the framework of environmental reporting of enterprises. Table 3 presents the initial data for the construction of metabolic profiles using the example of two world megacities: London and Moscow, which have comparable indicators for many factors.

It should be noted that in Moscow, the main fuel is natural gas, unlike London, where, along with hydrocarbons, nuclear energy and renewable energy sources are present in the city's balance sheet. Thus, the structure of electricity consumption directly affects the volume of harmful substances and greenhouse gases emissions. In addition, as stated earlier the use of conditionally calculated indicators of greenhouse gas emissions in the coverage areas of large agglomerations does not provide an understanding of the essence of the processes taking place in cities.

**Table 3.** Metabolic values in London and Moscow

Factors	London (pop.: 12 400 000) [28]	Moscow (pop.: 13 600 000) [28]
Consumption of electrical energy, TJ (GW·h) [28]	143 804.67 (39 945.74)	187 035.48 (51 954.30)
Energy consumption by mobile units, TJ [28]	182 955.66	263 052.06
Solar radiation, kW·h/m <sup>2</sup> [28]	1 050.00	1 020.70
Precipitation, mm [28]	601.00	698.00
Harmful substances emissions	n/a	n/a
Greenhouse gas emissions, mln. tonnes/year [29, 30]	70.00	120.00
Greenhouse gas absorption capacity	n/a	n/a
Water consumption, mln. m <sup>3</sup> [28]	707.27	1 496.00
Solid municipal waste disposal, th. tonnes [28]	1 696.00	4 003.20
GDP (gross domestic product), mln. USD [28]	386 900.00	664 420.00
EROI (energy returned on energy invested) [13, 18]	33.6	74.0

**Acknowledgement:** This study is financed by the European Union-NextGenerationEU, through the National Recovery and Resilience Plan of the Republic of Bulgaria, project № BG-RRP-2.013-0001-C01.

### CONCLUSIONS

EROI is a fairly specific energy indicator at the intersection of technical, economic and social sciences. Its usage to date is determined by two limitations: the development of correct calculation and forecasting methods, as well as the determination of the limits of practical applicability. This article proposes a solution to the second limitation, namely, the calculation of the weighted average EROI of a city's electrical energy consumption system. This value can be useful in the analysis of the fuel and energy balance, economic development potential and sustainability of a city energy system.

At the same time, an increase in the share of energy resources with low EROI in a city's balance, for example, as part of a "green" energy transition, can lead to a decrease in the level of urban metabolism of the city and a drop in the weighted average EROI to socially and industrially significant values. A potential task is to build a metabolic profile of cities and search for reserves for energy saving, including taking into account the current and future values of a city's EROI.

Promising areas for the study of urban metabolism include:

- Calculation of the fuel and energy balances of cities, considering the dynamics they are under in the context of the last 10-25 years.
- Development of a list of absolute and specific criteria for the typologization of cities.

- Building models for predicting the level of metabolism and a list of strategic activities for groups of cities with similar energy and environmental profiles.

- Assessment of the energy saving potential in urban energy.

- Search for avenues to improve the environmental characteristics of enterprises and their involvement in the fuel and energy balance of a city.

### REFERENCES

1. V. Court, F. Fizaine, . *Ecological Economics*, **138**, 145 (2017), ISSN 0921-8009, <https://doi.org/10.1016/j.ecolecon.2017.03.015>.
2. R. Atlason, R. Unnthorsson, *Energy*, **67**, 241 (2014), ISSN 0360-5442, <https://doi.org/10.1016/j.energy.2014.01.096>.
3. D. Weißbach, G. Ruprecht, A. Huke, K. Czerski, S. Gottlieb, A. Hussein, *Energy*, **52**, 210 (2013), ISSN 0360-5442, <https://doi.org/10.1016/j.energy.2013.01.029>.
4. J.-P. Oosterom, Ch. A. S. Hall, *Energy Policy*, **168**, 112953 (2022), ISSN 0301-4215, <https://doi.org/10.1016/j.enpol.2022.112953>.
5. A. Jackson, T. Jackson, *Ecological Economics*, **185**, 107023 (2021), ISSN 0921-8009, <https://doi.org/10.1016/j.ecolecon.2021.107023>.
6. J. Yan, L. Feng, A.N. Steblyanskaya, S. Fu, *Finance: Theory and Practice*, **24**(2), 50 (2020), <https://doi.org/10.26794/2587-5671-2020-24-2-50-59>.
7. Yu. I. Sokolov, *Issues of Risk Analysis*, **18** (4), 28 (2021), <https://doi.org/10.32686/1812-5220-2021-18-4-28-47>.
8. E. V. Otrubyannikov, M. V. Terekhova, B. Ali, Design, technologies and innovations in the textile and light industry (INNOVATIONS-2022): Collection of materials of the International scientific-technical conference, Moscow, November 16, 2022. Part 3, Moscow, Federal State Budgetary Educational

- Institution of Higher Education A. N. Kosygin Russian State University (Technology. Design. Art), 2022. p. 69, EDN BIOTCZ. (In Russ.)
10. J. G. Lambert, Ch. A. S. Hall, S. Balogh, A. Gupta, M. Arnold, *Energy Policy*, **64**, 153 (2014), ISSN 0301-4215, <https://doi.org/10.1016/j.enpol.2013.07.001>.
  11. F. Fizaine, V. Court, *Energy Policy*, **95**, 172 (2016), ISSN 0301-4215, <https://doi.org/10.1016/j.enpol.2016.04.039>.
  12. Ya. E. Shklyarsky, M. A. Gubarev, V. A. Vorobyova, Yu. N. Kuznetsova, Problems of the mineral resource complex through the eyes of young scientists: Materials of the All-Russian scientific and educational seminar students, St. Petersburg, April 08, 2022, A. B. Makhovikov (ed.), St. Petersburg: Cultural and Educational Partnership, 2023, p. 107, EDN UNRBRG. (In Russ.)
  13. Ch. A. S. Hall, J. G. Lambert, S. B. Balogh, *Energy Policy*, **64**, 141 (2014), ISSN 0301-4215, <https://doi.org/10.1016/j.enpol.2013.05.049>.
  14. M. Raugei, E. Leccisi, *Energy Policy*, **90**, 46 (2016), ISSN 0301-4215, <https://doi.org/10.1016/j.enpol.2015.12.011>.
  15. Ch. A. S. Hall, *Joule*, **1** (4), 635 (2017), ISSN 2542-4351, <https://doi.org/10.1016/j.joule.2017.09.010>.
  16. Zhaoyang Kong, Xi Lu, Xiucheng Dong, Qingzhe Jiang, Noah Elbot, *Energy Strategy Reviews*, **22**, 179 (2018), ISSN 2211-467X, <https://doi.org/10.1016/j.esr.2018.09.003>.
  17. Jingxuan Feng, Lianyong Feng, Jianliang Wang, C. W. King, *Energy*, **144**, 232 (2018), ISSN 0360-5442, <https://doi.org/10.1016/j.energy.2017.11.061>.
  18. Y. Hu, Ch. A. S. Hall, J. Wang, L. Feng, A. Poisson, *Energy*, **54**, 352 (2013), ISSN 0360-5442, <https://doi.org/10.1016/j.energy.2013.01.067>.
  19. A. Steblyanskaya, W. Zhen, A. Denisov, M. Rybachuk, S. Razmanova, *Natural Gas Industry B*, **6** (6), 639 (2019), ISSN 2352-8540, <https://doi.org/10.1016/j.ngib.2019.10.002>.
  20. I. Capellán-Pérez, C. de Castro, L. J. M. González, *Energy Strategy Reviews*, **26**, 100399 (2019), ISSN 2211-467X, <https://doi.org/10.1016/j.esr.2019.100399>.
  21. M. Raugei, S. Sgouridis, D. Murphy, V. Fthenakis, R. Frischknecht, Ch. Breyer, U. Bardi, Ch. Barnhart, A. Buckley, M. Carbajales-Dale, D. Csala, M. de Wild-Scholten, G. Heath, A. Jæger-Waldau, Ch. Jones, A. Keller, E. Leccisi, P. Mancarella, N. Pearsall, A. Siegel, W. Sinke, Ph. Stolz, *Energy Policy*, **102**, 377 (2017), ISSN 0301-4215, <https://doi.org/10.1016/j.enpol.2016.12.042>.
  22. D. Müller, D. Chartouni, *Applied Energy*, **326**, 119958 (2022), ISSN 0306-2619, <https://doi.org/10.1016/j.apenergy.2022.119958>.
  23. M. Diesendorf, T. Wiedmann, *Ecological Economics*, **176**, 106726 (2020), ISSN 0921-8009, <https://doi.org/10.1016/j.ecolecon.2020.106726>.
  24. A. Fabre, *Ecological Economics*, **164**, 106351 (2019), ISSN 0921-8009, <https://doi.org/10.1016/j.ecolecon.2019.06.006>.
  25. Canada Energy Regulator: <https://www.cer-rec.gc.ca>
  26. U.S. Department of Energy: <https://www.energy.gov>
  27. UK Energy in brief 2022: <https://www.gov.uk>
  28. Metabolism of Cities, web: <https://metabolismofcities.org/>
  29. Ontario Tech University. Energy and material flows of megacities. URL: <https://ontariotechu.ca/>
  30. C. Kennedy S. Pincetl, P. Bunje, *Environmental Pollution*, **159**, 1965 (2011).
  31. T. Wei, J. Wu, S. Chen, *Frontiers in Sustainable Cities*, **3**, 696381 (2021), 10.3389/frsc.2021.696381.
  32. A. A. Genbach, D. Y. Bondartsev, I. K. Iliev, *J. Mach. Eng.*, **2**, 106 (2018).
  33. A. Genbach, K. Olzhabayeva, I. Iliev, *Thermal Science*, **20** (5), 1777 (2016).

## AUTHOR INDEX

- Abou-Zied O. K., See Al-Ruqeishi et al. .... 328
- Abzhalelov B. B., See Appazov et al. .... 9
- Acknowledgement to reviewers for Vol 55 (2023) .... 88
- Adilbayev N., See Bolegenova et al. .... 38
- Akyol E., Danisman M., Evaluating the efficacy of cherry stem extracts against calcium oxalate monohydrate crystallization in kidney stone treatment ..... 282
- Akyol E., See Mutlu et al. .... 342
- Alaman Ađar A., See Meral et al. .... 274
- Al-Ruqeishi Z. B., Abou-Zied O. K., The influence of gold nanorods' aspect ratio on the structure and spectroscopic properties of TiO<sub>2</sub> nanoparticles for solar cell utilization ..... 328
- Alshamhazi O. T. A., K¼¼k I., Doymaz I., Investigation of mass transfer in infrared drying of Ahlat pears: experimental and modeling approaches ..... 228
- Apostolov A., See Boyadjiev et al. .... 321
- Apostolov A., See Petrova et al. .... 333
- Apostolova D., See Chorbazhiyska et al. .... 395
- Appaz A. N., See Appazov et al. .... 9
- Appazov N. O., Syzdykbayev M. I., Appaz A. N., Nazarov E. A., Darmagambet K. Kh., Balykbayeva G. T., Abzhalelov B. B., Askarova G. Sh., Kim Yu. A., Microwave activation of isovaleric acid monoglyceride synthesis and its antimicrobial activity ..... 9
- Arda G., Karasakal A., Determination of trace and major elements in commercial propolis samples by ICP-OES after microwave digestion ..... 358
- Askarova A., See Bolegenova et al. .... 38
- Askarova G. Sh., See Appazov et al. .... 9
- Atanassova M., Todorova N., Goranova-Markova S., The history of the first germanium crystals along with a descendant of the novel "Bulgarians of old time" ..... 175
- Auce A., Jermuss A., Rucins A., Auce I., Horns I. A., Solar and heat pump hybrid heated greenhouse in Latvia: energy storage and CO<sub>2</sub> reduction ..... 32
- Auce I., See Auce et al. .... 32
- Author Index ..... 433
- Azoulay M., See Brusov et al. .... 27
- Bacheva K., See Veleva et al. .... 427
- Bajsert M., See Płowens et al. .... 44
- Balci S., See Uđur et al. .... 352
- Balykbayeva G. T., See Appazov et al. .... 9
- Banov K., See Stankov et al. .... 82
- Baraniak J., See Płowens et al. .... 44
- Baraniak M., See Płowens et al. .... 44
- Beker Ū., See Duranođlu et al. .... 203
- Beketayeva M., See Bolegenova et al. .... 38
- Beloev H. I., See Iliev et al. .... 433
- Benarafa L., See Rghioui et al. .... 407
- Beschkov V., See Stefanov et al. .... 379
- Blagoev B. S., See Rafailov et al. .... 401
- Boiadjieva E., Tafrova-Grigorova A., Digitalization in Bulgarian science education: a comparative analysis of the state of the art ..... 184
- Bolegenova S., Askarova A., Georgiev A., Beketayeva M., Bolegenova S., Maximov V., Adilbayev N., Selection of the optimal kinetic scheme for the formation of nitrogenous substances in the simulation of low-quality coal combustion ..... 38
- Bolegenova S., See Bolegenova et al. .... 38
- Boyadjiev B., Petrova T., Vladova R., Kirilova E., Apostolov A., Moravski A., Optimization and determination of the factors influencing the delamination in graphene/MoS<sub>2</sub>/PET nanocomposite under mechanical loading ..... 321
- Boyadjiev B., See Petrova et al. .... 333
- Boyadjiev S., See Rafailov et al. .... 401
- Brusov A., Azoulay M., Orr G., Golan G., Influence of a weak pulsed magnetic field on the recovery and recrystallization in aluminum ..... 27
- Chorbazhiyska E., Apostolova D., Dalgacheva V., Mitov M., Microbiologically influenced corrosion (MIC) - monitoring and prevention ..... 395
- Dakova I., See Veleva et al. .... 427
- Dalgacheva V., See Chorbazhiyska et al. .... 395
- Danisman M., See Akyol et al. .... 282
- Darakchiev R., See Semkov et al. .... 53
- Darakchiev S., See Semkov et al. .... 53
- Darmagambet K. Kh., See Appazov et al. .... 9
- Deniz S., See Yolađan et al. .... 314
- Dimitrov D. Z., See Rafailov et al. .... 401
- Dimitrov O. S., See Zaharieva et al. .... 164, 169
- Dimova S. S., See Zaharieva et al. .... 164
- Doymaz I., See Alshamhazi et al. .... 228
- Duranođlu D., K¼¼k I., Beker Ū., Continuous flow chromium (VI) adsorption onto peach stone- and acrylonitrile-divinylbenzene copolymer-based activated carbons ..... 203
- Duranođlu D., See Neziri et al. .... 208
- El Hajji A., See Rghioui et al. .... 407
- Eneva R. T., See Zaharieva et al. .... 164, 169
- Eren B., Yalcin Gurkan Y., Theoretical study of possible reaction pathways with the OH radical of the Apranax (AP) molecule with naproxen sodium (NS) as an active ingredient ..... 242
- Fedyukhin A. V., See Iliev et al. .... 433
- Fridmans R., See Kirilova et al. .... 265
- Gadekar S. S., See Sadaphal et al. .... 388
- Ganev E., Panyovska S., Stefanova K., Overview of approaches to obtaining energy from heat including ground-based installation ..... 101
- Gawai J. J., See Sadaphal et al. .... 388
- Georgiev A., See Bolegenova et al. .... 38
- G¼k B., Kıpđak E., The effect of chemical pretreatment on the drying behavior of blueberries ..... 233
- Golan G., See Brusov et al. .... 27
- Goranova-Markova S., See Atanassova et al. .... 175
- Guennoun L., See Rghioui et al. .... 407
- Gurkan B., See Guven et al. .... 255

Güven N., Gurkan B., Yalcin Gurkan Y., Removal of penicillin group antibiotics azlocillin, cloxacillin, methicillin from wastewater by DFT method .....	255	crystal media of -ONNO- type Schiff bases and metal complexes .....	274
Habib S., See Naseer et al. ....	125	Mitov M., See Chorbadzhiyska et al. ....	395
Hazar B., Şakar D., Kinetic investigation of methyl violet dye adsorption on agar-agar impregnated activated carbon .....	215	Mitova S. L., See Zaharieva et al. ....	169
Horns I. A., See Auce et al. ....	32	Moravski A., See Boyadjiev et al. ....	321
Hubenov V. N., See Zaharieva et al. ....	164	Moravski A., See Petrova et al. ....	333
Idakiev V. V., Mörl L., Inductively heated fluidized beds and their potential for energy savings and efficient process control .....	159	Mörl L., See Idakiev et al. ....	159
Ilaiyavel S., See Palani et al. ....	416	Mutlu H., Akyol E., Development of transdermal cellulose-based patches for Alzheimer's treatment and investigation of penetration behavior .....	342
Iliev I. K., Fedyukhin A. V., Yavorovsky Y. V., Beloev H. I., The application of an energy metric (EROI) for the analysis of a city energy profile .....	433	Naseer A., Naz Awan A., Iqbal J., Habib S., Javed A., Cobalt complexes of pyridine carboxaldehyde Schiff bases as cholinesterase inhibitors and anti-proliferative activity .....	125
Instructions to authors .....	89, 196, 362, 447	Naz Awan A., See Naseer et al. ....	125
Iqbal J., See Naseer et al. ....	125	Nazarov E. A., See Appazov et al. ....	9
Javed A., See Naseer et al. ....	125	Nedev N. D., See Nenova et al. ....	369
Jermuss A., See Auce et al. ....	32	Nenov T. G., See Nenova et al. ....	369
Kadioğlu Z., Şakar D., Methyl violet dye removal investigation on submicron particle size rubber powder obtained from scrap tyre functionalized with agar-agar .....	309	Nenova Z. P., Kozhukharov S. V., Nenov T. G., Nedev N. D., Thin film humidity sensing elements based on TiO <sub>2</sub> and graphene .....	369
Karadjov M., See Veleva et al. ....	427	Neziri E., Duranoğlu D., Modeling of continuous-flow phenol adsorption onto acrylonitrile-divinylbenzene copolymer .....	208
Karaivanova M. K., See Koleva et al. ....	76	Oreha J., See Kirilova et al. ....	265
Karasakal A., See Arda et al. ....	358	Orr G., See Brusov et al. ....	27
Karasakal A., See Tokatli Demirok et al. ....	260	Osipovs S., See Kirilova et al. ....	265
Khaoulaf R., See Rghioui et al. ....	407	Öztürk S., Küçük İ., The effect of pigment on the properties of black automotive enamel .....	348
Kim Yu. A., See Appazov et al. ....	9	Ozyalcin Z. O., Kipcak A. S., Drying kinetics, mathematical modeling and color analysis of <i>Solen marginatus</i> : A comparative study of oven, infrared, and microwave drying methods .....	221
Kipcak A. S., See Ozyalcin et al. ....	221	Özyörü Z. İ., See Uğur et al. ....	352
Kıpçak E., See Gök et al. ....	233	Palani R., Ilaiyavel S., Mathanbabua M., Mechanical properties, EDM process optimization, and wear performance of Al 7075-based NiCr-graphite reinforced metal matrix composites .....	416
Kirilova E., Fridmans R., Puckins A., Oreha J., Osipovs S., Photophysical study of benzanthrone 3-isothiocyanate as novel fluorescent label .....	265	Panchani D., Maurya S., Thaker T., Rathod V., Thakur Sh., Synthesis, biological evaluation, ADME studies and molecular docking with $\beta$ -tubulin of fused benzimidazole-pyridine derivatives .....	107
Kirilova E., See Boyadjiev et al. ....	321	Panyovska S., See Ganey et al. ....	101
Kirilova E., See Petrova et al. ....	333	Penchev H. P., See Zaharieva et al. ....	164, 169
Kirilova E., See Vladova et al. ....	147	Petrova T., Kirilova E., Vladova R., Apostolov A., Boyadjiev B., Moravski A., Multi-parameter optimization of layered hBN/PMMA nanocomposite under mechanical loading .....	333
Kolev D. N., Increasing the energy efficiency of combustion processes using contact economizer systems and finned tube heat exchanger .....	21	Petrova T., See Boyadjiev et al. ....	321
Koleva D. R., Karaivanova M. K., Modeling of rectification in a laboratory single-sieve tray column .....	76	Petrova T., See Semkov et al. ....	53
Kostadinova O., See Stankov et al. ....	82	Petrova T., See Vladova et al. ....	147
Kozhukharov S. V., See Nenova et al. ....	369	Płowens R., Baraniak M., Lota K., Baraniak J., Bajsert M., Lota G., Carbon materials used as additives to active mass of semi-traction lead-acid batteries .....	44
Küçük I., See Alshamhazi et al. ....	228	Pozan Soyly G. S., See Reis et al. ....	288
Küçük I., See Duranoğlu et al. ....	203	Puckins A., See Kirilova et al. ....	265
Küçük İ., See Öztürk et al. ....	348	Rafailov P. M., Mehandzhiev V. B., Sveshtarov P. K., Blagoev B. S., Sotirov S., Boyadjiev S., Tomov V., Yankova L., Spassov D., Dimitrov D. Z., Specific	
Kurteva V., In memoriam Prof. DSc Ivan Pojarlieff (Johnny) .....	99		
Ljutzkanov L., See Stefanov et al. ....	379		
Lota G., See Płowens et al. ....	44		
Lota K., See Płowens et al. ....	44		
Mathanbabua M., See Palani et al. ....	416		
Maurya S., See Panchani et al. ....	107		
Maximov V., See Bolegenova et al. ....	38		
Mehandzhiev V. B., See Rafailov et al. ....	401		
Meral S., Alaman Açar A., Synthesis, characterization and effects to cholesteric lyotropic liquid			

problems in the CVD growth of graphene and carbon nanotubes.....	401
Rathod V., See Panchani et al.....	107
Reis E. G., Pozan Soyulu G. S., Investigation of <i>in vitro</i> digestive process in optimization of ultrasound-assisted extraction with citric acid anhydride for antioxidant production from red beet, Swiss chard, and dragon fruit.....	288
Rghioui L., Benarafa L., Khaoulaf R., El Hajji A., Guennoun L., Serghini Idrissi M., Contribution to the structural study of $Rb_3Ln(PO_4)_2$ materials (Ln=La, Ce, Pr, Nd, Sm, Eu, Gd and Tb) by vibrational spectroscopy.....	407
Rucins A., See Auce et al. ....	32
Sadaphal S. A., Sapkal S. B., Gadekar S. S., Gawai J. J., Resin Tulsion-8052 MP – a novel and ecofriendly catalyst for Knoevenagel reaction in aqueous medium .....	388
Şakar D., See Hazar et al. ....	215
Şakar D., See Kadioğlu et al. ....	309
Sapkal S. B., See Sadaphal et al. ....	388
Semkov K., Darakchiev R., Petrova T., Darakchiev S., Horizontal expanded metal sheet packing (Holpack) for mass and heat transfer processes in column apparatuses – study of research, mathematical modeling and industrial application .....	53
Serdaroglu G., Carvacrol and 4-IP-2-MeO-1-MB derivatives: DFT computations and drug-likeness studies .....	247
Serghini Idrissi M., See Rghioui et al. ....	407
Slavova V., Application of mobile fluorescence spectroscopy as a method for the analysis of representatives of different varieties of carrots ( <i>Daucus carota</i> ) during storage under uncontrolled conditions.....	14
Slavova V., Application of mobile fluorescence spectroscopy as a method in the determination of varietal differences in black radish ( <i>Raphanus sativus</i> L. var. Niger) during storage under uncontrolled conditions.....	5
Sotirov S., See Rafailov et al. ....	401
Spasov D., See Rafailov et al. ....	401
Stambolova I. D., See Zaharieva et al.....	164
Stankov S., Banov K., Kostadinova O., Influence of the synthesis surfactants on the electrochemical and physicochemical properties of copper zinc tin sulfide .....	82
Stefanov S., Uzun D., Ljutzkanov L., Beschkov V., Sulfide driven fuel cell performance enhanced by integrated chemosorption and electricity generation.....	379
Stefanova K., See Ganev et al.....	101
Stoyanova D. D., See Zaharieva et al. ....	164
Subject Index.....	444
Sveshtarov P. K., See Rafailov et al. ....	401
Syzdykbayev M. I., See Appazov et al.....	9
Tafrova-Grigorova A., See Boiadjeva et al. ....	184
Thaker T., See Panchani et al. ....	107
Thakur Sh., See Panchani et al. ....	107
Todorova N., See Atanassova et al.....	175
Tokatli Demirok N., Karasakal A., Determination of macro- and microelement contents in thyme oil and rosemary oil by ICP-OES .....	260
Tomov V., See Rafailov et al. ....	401
Tuçcu F. T., Synthesis of substituted 4-methylphenyl-2-iminothiazolidinone compounds <i>via</i> one-pot method.....	270
Turhan K., Optimization of ozonation in the removal of Basic Blue 41 in aqueous solution.....	302
Ublekov F. S., See Zaharieva et al. ....	164
Uğur Nigiz F., Özyörü Z. İ., Balci S., Improved packaging performance of olive tree-based biochar-loaded poly(lactic acid) films .....	352
Unlu D., Dehydration of industrial isopropanol wastewater by pervaporation using carboxy methyl cellulose and graphene oxide hybrid membranes.....	296
Uzun D., See Stefanov et al.....	379
Veleva O., Bacheva K., Dakova I., Karadjov M., Silica gel chemically modified with ionic liquid – efficient sorbent for Au, Ir, Pd and Pt.....	427
Vladova R., Petrova T., Kirilova E., A multi-objective robust optimization to design a sustainable dairy supply chain under uncertain product demands, economic and social consideration. A real case study from Bulgaria.....	147
Vladova R., See Boyadjiev et al.....	321
Vladova R., See Petrova et al. ....	333
Yalcin Gurkan Y., See Eren et al. ....	242
Yalcin Gurkan Y., See Guven et al. ....	255
Yankova L., See Rafailov et al. ....	401
Yavorovsky Y. V., See Iliev et al.....	433
Yolaçan Ö., Deniz S., Effects of additives on mechanical and barrier properties of polyhydroxyalkanoate-derived bio-nanocomposite films by solution casting.....	314
Zaharieva K. L., Dimova S. S., Eneva R. T., Hubenov V. N., Stambolova I. D., Stoyanova D. D., Ublekov F. S., Dimitrov O. S., Penchev H. P., PLA/PVP/bio-synthesized hydrozincite nanocomposite films – photocatalytic and antibacterial activity .....	164
Zaharieva K. L., Eneva R. T., Mitova S. L., Dimitrov O. S., Penchev H. P., Preparation and antimicrobial activity of silver nanoparticles impregnated with halloysite clay.....	169

## SUBJECT INDEX

$\beta$ -Tubulin .....	107	continuous flow adsorption .....	203
3D computer modeling .....	38	continuous process .....	208
acrylonitrile divinyl benzene .....	203	crystallization .....	282
acrylonitrile-divinylbenzene copolymer .....	208	Cu <sub>2</sub> ZnSnS <sub>4</sub> .....	82
activated carbon .....	203	dairy supply chain .....	147
active methylene compounds .....	388	decolorization .....	302
adsorption .....	208	dehydration .....	296
adsorption isotherms .....	215, 309	delamination .....	321, 333
agar-agar .....	309	DFT .....	242, 247, 255
agar-agar impregnated activated carbon .....	215	DigComp .....	184
Ahlat pear .....	228	DigCompEdu .....	184
air-to-water heat pump .....	32	digestion .....	288
aldehydes .....	388	digital competence .....	184
aluminum .....	27	direct contact heat transfer .....	53
aluminum metal matrix .....	416	discovery of germanium .....	175
Alzheimer .....	342	distillation .....	76
amino acids .....	265	donepezil hydrochloride .....	342
antibacterial activity .....	9, 107, 164	drug delivery .....	342
antibiotics .....	255	drug likeness .....	247
antifungal activity .....	9	drying kinetics .....	221
antimicrobial activity .....	169	dye removal .....	215
antioxidant .....	288	dye-sensitized solar cells .....	328
Apranax .....	242	eco-friendly surfactants .....	82
ascorbic acid .....	82	economic sustainability improvement .....	147
Au nanorods .....	328	EDS .....	416
azlocillin .....	255	effective diffusivity .....	228
Bacillus subtilis .....	169	electrochemical impedance spectroscopy (EIS) .....	395
Basic blue 41 .....	302	emission wavelength .....	5, 14
Basic dyes .....	302	emissions .....	38
benzanthrone .....	265	enamel .....	348
benzimidazole .....	107	energy conservation .....	433
bioavailability .....	288	energy consumption .....	433
bioblend .....	314	energy efficiency .....	21
biochar .....	352	energy storage .....	32, 44
black radish accessions .....	5	environmental sustainability improvement .....	147
blueberry .....	233	EROI .....	433
calcium oxalate .....	282	Escherichia coli .....	169
carbon additives .....	44	essential oil .....	260
carbon nanotubes .....	401	exergy efficiency technologies .....	101
carrot accessions .....	14	extraction .....	288
carvacrol .....	247	extrusion .....	314
catalysis .....	379	fluidized bed .....	159
CFD .....	101	fluorescence .....	265
chemical pretreatment .....	233	fluorescence spectroscopy .....	5, 14
chemical vapor deposition .....	401	FMO & MEP .....	247
chemo-sorption .....	379	food supplement .....	358
cherry stem .....	282	gas diffusion electrode .....	379
cholesteric lyotropic liquid crystal .....	274	Gaussian 09 .....	242, 255
cholinesterase inhibition .....	125	geological samples .....	427
chromium .....	203	graphene .....	369, 401
clam .....	221	graphene/MoS <sub>2</sub> /PET nanocomposite .....	321
Clemens Winkler .....	175	greenhouse .....	32
cloxacillin .....	255	grooved razor shell .....	221
CO <sub>2</sub> reduction .....	21, 32	halloysite .....	169
cobalt complexes .....	125	hBN/Interface/PMMA nanocomposite .....	333
composite films .....	352	heat exchange .....	159
contact economizer .....	21	heat exchangers .....	21
contactless energy input .....	159	high-purity sepiolite .....	314

Holpack packing .....	53	packed columns .....	53
horizontal expanded metal sheet packing .....	53	paint glass-ceramics .....	348
host-guest interaction .....	274	peach stone .....	203
humidity sensing elements .....	369	penetration .....	342
ICP-OES .....	260, 358	percentage of liquid-phase resistance over total mass-transfer resistance .....	76
iminothiazolidinone .....	270	pervaporation .....	296
inductive heating .....	159	phase transition .....	407
infrared .....	407	phenol .....	208
infrared drying .....	228, 233	phenolic content .....	288
inhibition .....	282	photocatalyst .....	164
inorganic chemistry .....	175	pigment .....	348
interface shear stress .....	321, 333	PLA/PVP/Hydrozincite .....	164
internal friction .....	27	polarization resistance (PR) method .....	395
ionic liquids .....	427	polygonization .....	27
isopropanol .....	296	polyhydroxyalkanoate .....	314
isopropylidene protection .....	9	polylactic acid packaging .....	352
isothiocyanate .....	265	polyvinylpyrrolidone .....	82
isovaleric acid monoglyceride .....	9	precise temperature control .....	159
julolidene derivative Schiff base .....	274	pressure drop .....	53
K <sub>2</sub> CO <sub>3</sub> .....	233	process intensification .....	53
kidney stone .....	282	propolis .....	358
kinetic model .....	38	proteins .....	265
kinetic parameters .....	215	Raman .....	407
kinetic studies .....	309	Raman analysis .....	401
Knoevenagel reaction .....	388	recovery .....	27
laminated glass .....	348	recrystallization .....	27
Latvia .....	32	recyclable catalyst .....	388
Li-ion battery .....	82	Resin Tulsion-8052 MP catalyst .....	388
linear sweep voltammetry (LSV) .....	395	robust optimization .....	147
local efficiency .....	76	rosemary oil .....	260
low-grade coal .....	38	Schiff bases .....	125
luminescent label .....	265	science education .....	184
machining parameters .....	416	scrap tyre .....	309
Malachite Green .....	164	seafood .....	221
mass transfer .....	53	SEM .....	416
mathematical modeling .....	221	Semi-traction lead-acid battery .....	44
metal complex .....	274	sieve trays .....	76
metallurgy .....	175	silver nanoparticles .....	169
methicillin .....	255	social sustainability improvement .....	147
Methyl violet dye .....	215, 309	soils .....	427
microbiologically influenced corrosion (MIC) .....	395	solar energy .....	32
microwave digestion .....	358	sol-gel method .....	369
microwave-assisted synthesis .....	9	solution casting .....	314
modeling .....	208, 228	solution-processed materials .....	82
molecular docking .....	107	solvent free .....	270
monoclinic .....	407	sorption .....	427
MTT assay .....	125	spectroscopy .....	358, 407
multicomponent reaction .....	270	storage under uncontrolled conditions .....	5, 14
multi-parameter optimization .....	321, 333	Stoycho Karavelov .....	175
nanocomposite .....	164	sulfide fuel cell .....	379
naproxen sodium .....	242	supply chain .....	101
membrane .....	296	sustainable development .....	101
nitrogenous substances .....	38	thiourea .....	270
noble metals .....	427	thyme oil .....	260
number of mass-transfer units .....	76	TiO <sub>2</sub> nanoparticles .....	328
OH radical .....	242	titanium dioxide .....	369
one-pot reaction .....	270	transdermal patch .....	342
optimal design .....	147	trigonal .....	407
optimization .....	302, 416	ultrasonic probe .....	125
ozonation .....	302		

uncertain conditions.....	147	wastewater.....	296, 302
urban energy system .....	433	water.....	388
urban metabolism.....	433	weak pulsed magnetic field .....	27
urban planning .....	433	wear.....	416
vacuum oven drying .....	233	wet digestion .....	260
variety .....	5, 14		

### Instructions about Preparation of Manuscripts

**General remarks:** Manuscripts are submitted in English by e-mail. The text must be prepared in A4 format sheets using Times New Roman font size 11, normal character spacing. The manuscript should not exceed 15 pages (about 3500 words), including photographs, tables, drawings, formulae, etc. Authors are requested to use margins of 2 cm on all sides.

Manuscripts should be subdivided into labelled sections, e.g. INTRODUCTION, EXPERIMENTAL, RESULTS AND DISCUSSION, etc. **The title page** comprises headline, author(s)' names and affiliations, abstract and key words. Attention is drawn to the following:

a) **The title** of the manuscript should reflect concisely the purpose and findings of the work. Abbreviations, symbols, chemical formulae, references and footnotes should be avoided. If indispensable, abbreviations and formulae should be given in parentheses immediately after the respective full form.

b) **The author(s)**' first and middle name initials and family name in full should be given, followed by the address (or addresses) of the contributing laboratory (laboratories). **The affiliation** of the author(s) should be listed in detail (no abbreviations!). The author to whom correspondence and/or inquiries should be sent should be indicated by an asterisk (\*) with e-mail address.

**The abstract** should be self-explanatory and intelligible without any references to the text and containing up to 250 words. It should be followed by keywords (up to six).

**References** should be numbered sequentially in the order, in which they are cited in the text. The numbers in the text should be enclosed in brackets [2], [5, 6], [9–12], etc., set on the text line. References are to be listed in numerical order on a separate sheet. All references are to be given in Latin letters. The names of the authors are given without inversion. Titles of journals must be abbreviated according to Chemical Abstracts and given in italics, the volume is typed in bold, the initial page is given and the year in parentheses. Attention is drawn to the following conventions: a) The names of all authors of a certain publications should be given. The use of "et al." in the list of references is not acceptable; b) Only the initials of the first and middle names should be given. In the manuscripts, the reference to author(s) of cited works should be made without giving initials, e.g. "Bush and Smith [7] pioneered...". If the reference carries the names of three or more authors it should be quoted as "Bush et al. [7]", if Bush is the first author, or as "Bush and co-workers [7]", if Bush is the senior author.

**Footnotes** should be reduced to a minimum. Each footnote should be typed double-spaced at the bottom of the page, on which its subject is first mentioned. **Tables** are numbered with Arabic numerals on the left-hand top. Each table should be referred to in the text. Column headings should be as short as possible but they must define units unambiguously. The units are to be separated from the preceding symbols by a comma or brackets. Note: The following format should be used when figures, equations, etc. are referred to the text (followed by the respective numbers): Fig., Eqns., Table, Scheme.

**Schemes and figures.** Each manuscript should contain or be accompanied by the respective illustrative material, as well as by the respective figure captions in a separate file. As far as presentation of units is concerned, SI units are to be used. However, some non-SI units are also acceptable, such as °C, ml, l, etc. Avoid using more than 6 (12 for review articles) figures in the manuscript. Since most of the illustrative materials are to be presented as 8-cm wide pictures, attention should be paid that all axis titles, numerals, legend(s) and texts are legible.

**The authors are required to submit the text with a list of three individuals and their e-mail addresses that can be considered by the Editors as potential reviewers. Please note that the reviewers should be outside the authors' own institution or organization. The Editorial Board of the journal is not obliged to accept these proposals.**

The authors are asked to submit **the** final text (after the manuscript has been accepted for publication) in electronic form by e-mail. The main text, list of references, tables and figure captions should be saved in separate files (as \*.rtf or \*.doc) with clearly identifiable file names. It is essential that the name and version of the word-processing program and the format of the text files is clearly indicated. It is recommended that the pictures are presented in \*.tif, \*.jpg, \*.cdr or \*.bmp format. The equations are written using "Equation Editor" and chemical reaction schemes are written using ISIS Draw or ChemDraw programme.

## EXAMPLES FOR PRESENTATION OF REFERENCES

### REFERENCES

1. D. S. Newsome, Catal. Rev.–Sci. Eng., 21, 275 (1980).
2. C.-H. Lin, C.-Y. Hsu, J. Chem. Soc. Chem. Commun., 1479 (1992).
3. R. G. Parr, W. Yang, Density Functional Theory of Atoms and Molecules, Oxford Univ. Press, New York, 1989.
4. V. Ponec, G. C. Bond, Catalysis by Metals and Alloys (Stud. Surf. Sci. Catal., vol. 95), Elsevier, Amsterdam, 1995.
5. G. Kadinov, S. Todorova, A. Palazov, in: New Frontiers in Catalysis (Proc. 10th Int. Congr. Catal., Budapest (1992), L. Guzzi, F. Solymosi, P. Tetenyi (eds.), Akademiai Kiado, Budapest, 1993, Part C, p. 2817.
6. G. L. C. Maire, F. Garin, in: Catalysis. Science and Technology, J. R. Anderson, M. Boudart (eds.), vol. 6, Springer Verlag, Berlin, 1984, p. 161.
7. D. Pocknell, GB Patent 2 207 355 (1949).
8. G. Angelov, PhD Thesis, UCTM, Sofia, 2001, pp. 121-126.
9. JCPDS International Center for Diffraction Data, Powder Diffraction File, Swarthmore, PA, 1991.
10. CA 127, 184 762q (1998).
11. P. Hou, H. Wise, J. Catal., in press.
12. M. Sinev, private communication.
13. <http://www.chemweb.com/alchem/articles/1051611477211.html>.

***Texts with references which do not match these requirements will not be considered for publication!!!***

CONTENTS

Z. P. Nenova, S. V. Kozhukharov, T. G. Nenov, N. D. Nedev, Thin film humidity sensing elements based on TiO <sub>2</sub> and graphene.....	369
S. Stefanov, D. Uzun, L. Ljutzkanov, V. Beschkov, Sulfide driven fuel cell performance enhanced by integrated chemisorption and electricity generation.....	379
S. A. Sadaphal, S. B. Sapkal, S. S. Gadekar, J. J. Gawai, Resin Tulsion-8052 MP – a novel and ecofriendly catalyst for Knoevenagel reaction in aqueous medium.....	388
E. Chorbadzhiyska, D. Apostolova, V. Dalgacheva, M. Mitov, Microbiologically influenced corrosion (MIC) - monitoring and prevention.....	395
P. M. Rafailov, V. B. Mehandzhiev, P. K. Sveshtarov, B. S. Blagoev, S. Sotirov, S. Boyadjiev, V. Tomov, L. Yankova, D. Spassov, D. Z. Dimitrov, Specific problems in the CVD growth of graphene and carbon nanotubes.....	401
L. Rghioui, L. Benarafa, R. Khaoulaf, A. El Hajji, L. Guennoun, M. Serghini Idrissi, Contribution to the structural study of Rb <sub>3</sub> Ln(PO <sub>4</sub> ) <sub>2</sub> materials (Ln=La, Ce, Pr, Nd, Sm, Eu, Gd and Tb) by vibrational spectroscopy.....	407
R. Palani, S. Ilaiyavel, M. Mathanbabua, Mechanical properties, EDM process optimization, and wear performance of Al 7075-based NiCr-graphite reinforced metal matrix composites.....	416
O. Veleva, K. Bacheva, I. Dakova, M. Karadjov, Silica gel chemically modified with ionic liquid – efficient sorbent for Au, Ir, Pd and Pt.....	427
I.K. Iliev, A.V. Fedyukhin, Y.V. Yavorovsky, H.I. Beloev, The application of an energy metric (EROI) for the analysis of a city energy profile.....	433
Author Index.....	441
Subject Index.....	444
INSTRUCTIONS TO AUTHORS.....	447